POLITECNICO DI TORINO

Master of Science: ICT for Smart Societies

Master's Degree Thesis

BREADCRUMBS
Building up Robust and Efficient routing Algorithms for Drones by integrating Connectivity and Risk awareness in a Suburban air Mobility Bvlos Scenario

Supervisor:
Prof. Michela Meo

Co-Supervisors:
Dr. Greta Vallero

Candidate:
Federica Gavazzi

A.Y. 2024/2025

Abstract

In recent years, the use of drones, or Unmanned Aerial Vehicles (UAVs), has expanded across various industries, including agriculture, emergency response, and logistics. However, these operations are generally restricted to within Visual Line of Sight (VLoS), limiting their effectiveness.
VLoS refers to drone operations where the pilot can maintain an uninterrupted visual observation of the UAV without any visual aids, such as binoculars or cameras. This type of flight is currently the standard for drone operations in Italy, primarily due to safety and regulatory concerns, ensuring the pilot can immediately react to potential obstacles or hazards. Extended Visual Line of Sight (EVLoS) is also permitted under specific conditions, allowing for slightly longer operational ranges with additional safeguards, such as spotters.
Beyond Visual Line of Sight (BVLoS) operations instead open up new possibilities but also introduce complex challenges, particularly in ensuring constant and reliable communication. This thesis aims to develop a novel framework for efficient BVLoS flight planning.

This research focuses on a case study in a realistic suburban scenario, also considering a realistic distribution of GSM towers. In such suburban environments, the key challenges revolve around ensuring reliable communication in BVLoS scenarios, adopting the Rural Macrocell (RMA) channel model.

Key performance indicators (KPIs) such as communication latency, signal strength, and Quality of Service (QoS) are analyzed to ensure continuous and reliable connectivity. By leveraging existing ground cellular infrastructure, we aim to ensure that UAVs remain under constant control without the need for costly, dedicated networks.

One of the central challenges in suburban areas is the variability in communication coverage and quality, especially when using the Rural Macrocell (RMA) channel model. This thesis proposes solutions that propose a graph-based framework, integrating an ad-hoc channel model to provide optimal flight routes. Experimental results demonstrate how drones can navigate through suburban environments while maintaining robust connections with cellular networks, enabling effective communication without the need for new infrastructure.

These methods have the potential to be applied in various real-world BVLoS missions, from agricultural monitoring to infrastructure inspections, enhancing

both the performance and safety of UAV flights. The results of this work lay the groundwork for future advancements in BVLoS connectivity and their potential deployment in larger-scale applications.

Acknowledgements

I would like to express my sincere gratitude to Professor Michela Meo and Doctor Greta Vallero, who followed me step by step with patience and helpfulness, giving me the support that I needed to successfully complete my thesis work.

This work started as a research project born in collaboration with the University of Perugia, University of Firenze and Politecnico of Torino. As such, I would like to extend my thanks for all the support given to me by all the professors and doctors from Università degli Studi of Perugia and Università degli Studi of Firenze. A special thanks in particular to Professor Francesco Betti Sorbelli and Professor Maria Cristina Pinotti, that gave me all the support I needed to finish this work.

Additionally, I am thankful for the expertise and assistance provided by Professor Andrea Maria Lingua and Doctor Francesca Matrone, for giving me their insights and especially all the initial data I required.
A special mention goes to all my work colleagues for their understanding, support and also important tips during these months.

Thanks to my dear friends, Betta, Bri, Ele and Fu for listening and supporting me during my outbursts. Thanks also to Alessandro, Claudio and Federico for the laughter and funny moments shared over these years, but above all the mutual support in the (numerous) moments of discouragement during which I felt fully understood only by them.

A really huge thank you to all my family, my sister Francesca for always pushing me to give my best. To my parents, with their support and encouragement they have sustained me throughout my entire academic journey. To my grandparents, for those who are still here and for those who are not, I know that wherever I can count on their support. To my uncles Federico, MC, Lella and Giovanni as well as my cousins Marta and Greg, who always remembered to cheer me on. Special thanks to my uncle Federico who is the only one in the family able to sustain my engineering monologues to the end.

Last but certainly not least, a big thank you to Francesco, who has put up with me during my difficult times, for his boundless patience and understanding. This achievement was also possible thanks to all of them and I am very grateful for their presence in my life.

Contents

Acronyms

4G Fourth Generation Cellular Network

5G Fifth Generation Cellular Network

AAM Advanced Air Mobility

BVLoS Beyond Visual Line of Sight

BS Base Station

CAGR Compound Annual Growth Rate

DEM Digital Elevation Model

EASA European Aviation Safety Agency

ESA European Space Agency

EVLoS Extended Visual Line of Sight

GBS Ground Base Stations

GSM Global System for Mobile Communications

ITU International Telecommunication Union

JARUS Joint Authorities for Rule-making on Unmanned Systems

KPI Key Performance Indicator

LoS Line of Sight

LTE Long Term Evolution

MDP2 Maximum Dependability Path Problem

PC Power Consumption

PL Path Loss

QoS Quality of Service

RF Radio Frequency

RMA Rural Macro Cell

RX Receiver

SNR Signal-to-Noise ratio

STD Standard

TCAS Traffic Collision Avoidance System

TX Transceiver

UAM Urban Air Mobility

UAV Unmanned Aerial Vehicle

UMA Urban Macro Cell

VLoS Visual Line of Sight

Chapter 1

Introduction

Unmanned Aerial Vehicles (UAVs), commonly known as drones, have experienced significant growth in their application across various fields in recent years. According to Forbes [2] in 2016, the global drone market was projected to reach a value of $127 billion by 2025, driven primarily by their use in infrastructure, agriculture, and transport sectors. In agriculture alone, precision farming applications using drones have grown by over 80% between 2014 and 2020, reflecting their efficiency in monitoring crops and optimizing resource use. Furthermore, the report [3] highlighted that the construction industry could save up to $45 billion annually by adopting drone technology for site inspections and surveys. These results are graphically represented in Fig. 1.1. From goods delivery and infrastructure monitoring to search-and-rescue operations, drones offer unmatched flexibility and efficiency in many sectors.

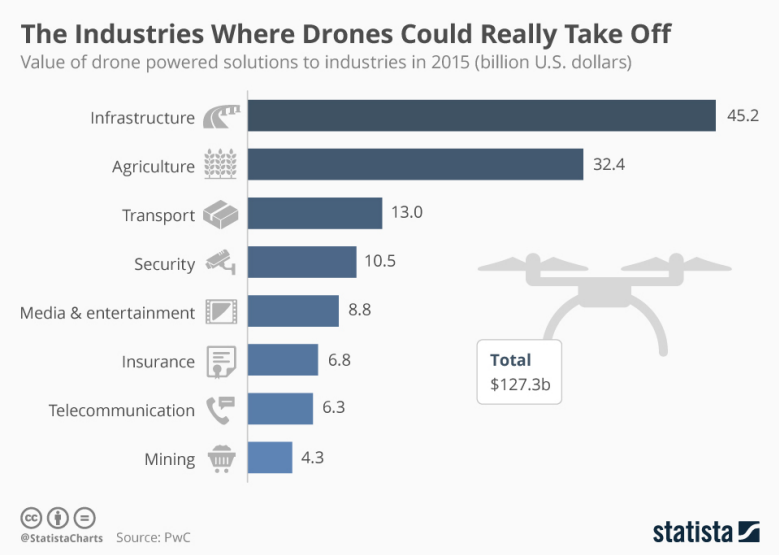

Figure 1.1: Commercial potential of drones in industrial sectors, data taken from [1]

According to more recent researches done by [4], the global commercial drone market size is estimated nowadays at approximately USD 60.37 billion and is projected to reach around USD 1,445.80 billion by 2034, growing at a Compound Annual Growth Rate (CAGR) of 37% during this period, as shows the graph in figure 1.2. The construction industry will be the sector that will benefit the most from drone technology, with potential annual savings of up to USD 45 billion through improved site inspections and surveys.
In the United States, the drone market is also expanding rapidly as stated in [4]. Sales of drones in the U.S. were estimated at USD 6.58 billion in 2024, with projections to reach USD 31.34 billion by 2034, indicating a CAGR of 16.9%.

Their increasing presence in urban and suburban environments has also transformed them into essential tools in advancing technological frontiers such as Urban Air Mobility (UAM) and Advanced Air Mobility (AAM). These paradigms aim to enhance transportation and logistics in areas underserved by traditional infrastructure, paving the way for more sustainable and efficient solutions.

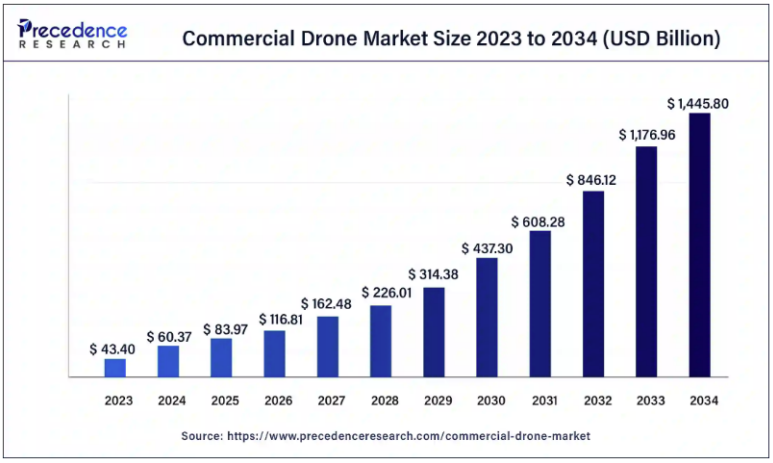

Figure 1.2: Commercial Drone market size from 2023, data taken from [4]

Despite their potential, UAVs face considerable operational limitations, particularly concerning their flight range and communication methodologies. Compared to traditional ground-based vehicles, drones have significantly smaller payload capacities and limited ranges, both of which are heavily influenced by battery life and payload weight. Current commercial drones typically have a maximum range between 15 to 50 kilometers, depending on the model and operational conditions, with flight times ranging from 20 to 50 minutes under ideal conditions, as investigated in [5] and [6]. Payload capacity is another limiting factor, with most commercial UAVs supporting loads of 1 to 5 kilograms, which decreases with extended range requirements or adverse weather conditions such as headwinds.
Environmental factors further exacerbate these constraints, as increased wind resistance can significantly affect energy consumption and reduce effective range,

as highlighted in [5]. These constraints require careful mission planning and the development of optimization strategies to ensure successful UAV operations within these technical limitations.

Currently, UAVs are primarily restricted to operations within the Visual Line of Sight (VLoS) of the pilot for many civilian uses, as stipulated by aviation regulations in many countries, including Italy. However, advancements in drone technology have introduced new operational paradigms, such as Extended Visual Line of Sight (EVLoS) and Beyond Visual Line of Sight (BVLoS). As shown in the diagram 1.3, VLoS operations rely on the pilot's direct visual contact only, suitable for activities like hobby flights, surveying construction sites, and real estate mapping. EVLoS, supported by a visual observer, expands the range to include more complex operations such as asset inspection and emergency response. BVLoS represents the most advanced mode, enabling many applications where the drone operates completely out of the pilot's sight, requiring at least a regulatory approval.

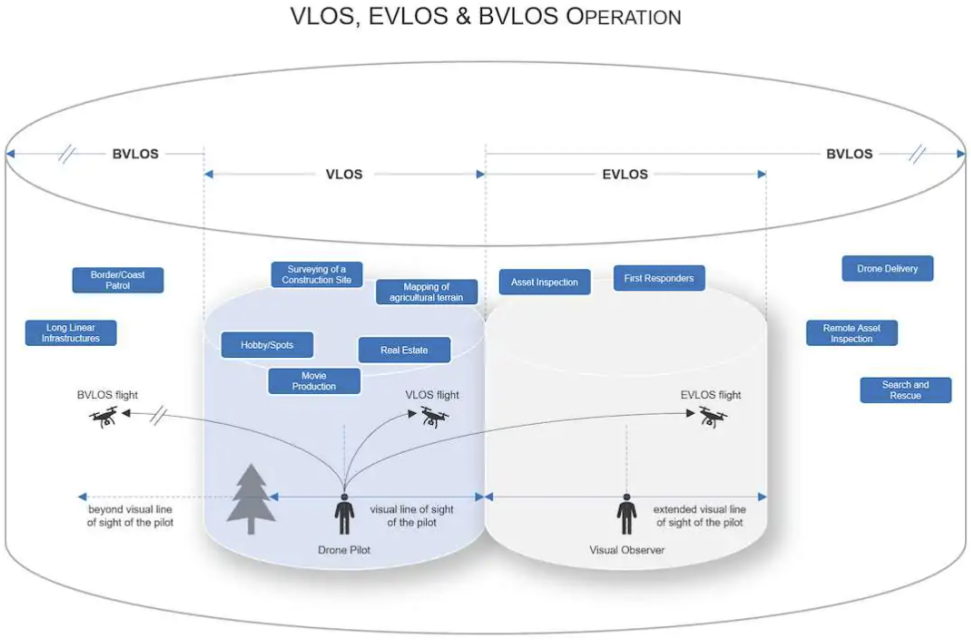

Figure 1.3: Differences between VLoS, EVLoS & BVLoS operations, reported in [12]

The European Aviation Safety Agency (EASA) classifies UAV operations into three categories, based on risk levels:

- **Open Category**: For low-risk operations, drones can be used without a permit if they are flown within the visual line of sight (VLoS), remain below 120 meters in altitude, and have a maximum flying weight of 25 kg. Depending on the weight of the drone, there are restrictions on how close to uninvolved persons it can be flown. The pilot must register with the aviation authority.

- **Specific Category**: or medium-risk operations, such as flights beyond the visual line of sight (BVLoS), a permit from the aviation authority is required. Theoretical and practical training is mandatory for drone pilots in this category, as well as the registration.

- **Certified Category**: For high-risk operations, including passenger transport, drones in this category have a size of at least 3 meters. The scope of the legal provisions hardly differs from manned aviation.

In the *open category*, as depicted in Fig. 1.4, drones can be used without a permit if they are flying in sight (clearly respecting the restrictions mentioned above). These limitations ensure safety by maintaining direct visual contact between the operator and the UAV but heavily constrain the scope of applications, especially for long-range or beyond-obstacle missions.
To unlock the full potential of UAVs, it is essential to enable Beyond Visual Line of Sight (BVLoS) operations. BVLoS flights allow UAVs to autonomously navigate and execute missions over extended distances without the need for constant visual oversight by a human operator. This capability expands the range of applications, the main ones are highlighted in [8] include:

- **Infrastructure Inspection**: BVLoS drones can inspect power lines, pipelines, and railways over long distances, enhancing efficiency and reducing the need for manual inspections.

- **Agricultural Monitoring**: Farmers can monitor large fields for crop health, irrigation issues, and pest infestations, enabling precise and timely interventions.

- **Environmental Monitoring**: BVLoS drones are used to monitor environmental changes, track wildlife, and conduct scientific research in remote areas, vital for conservation efforts and understanding ecological dynamics.

- **Disaster Response**: In emergencies, BVLoS drones can assess damage, locate survivors, and deliver supplies in areas inaccessible to ground teams.

Currently, these operations fall into the *specific category*, for which a permit from the aviation authority is required. As a drone pilot in this category, theoretical and practical training is mandatory.

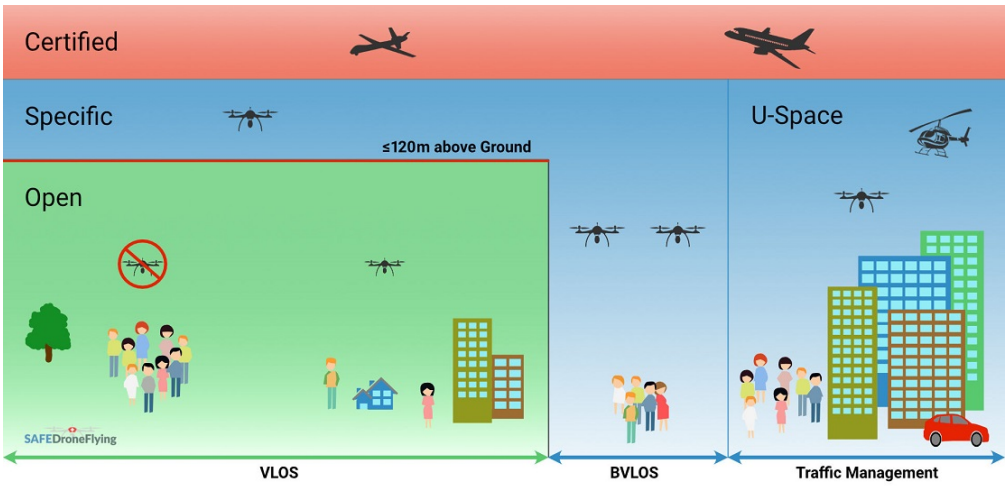

Figure 1.4: The airspace division for drones based on category, data taken from [9]

In the context of BVLoS, two critical challenges arise: ensuring safety and maintaining reliable communication. Safety concerns involve minimizing risks to both aerial and ground environments, including potential collisions or malfunctions, and mitigating threats to populated areas. Communication challenges focus on providing a robust, low-latency, and high-quality link between the UAV and the pilot or control station. In Italy and across Europe, where urban and suburban landscapes vary significantly, achieving reliable BVLoS operations requires addressing these dual challenges within the constraints of existing infrastructure.

A promising avenue to tackle these communication challenges lies in leveraging existing cellular networks, such as 4G and 5G, as primary or supplementary communication technologies for UAV operations. Cellular networks are already extensively deployed and provide wide-area coverage, high bandwidth, and low latency connections, making them a viable candidate for supporting BVLoS communication. Integrating UAVs with cellular networks could open up new possibilities for autonomous navigation, real-time monitoring, and adaptive mission planning, transforming industries such as delivery services, environmental monitoring, and emergency response.

However, utilizing cellular networks for UAV communications is not without its challenges. Ensuring adequate Quality of Service (QoS), addressing coverage gaps, and managing interference are vital to guaranteeing reliable and safe UAV operations, highlighted in [7]. In addition, Italian regulations currently impose strict limitations on BVLoS flights, making the widespread adoption of such technologies contingent on future policy changes and technological advancements.

1.0.1 Emerging Applications & Enabling Technologies for BVLoS Drones

The rapid development of drone technology has paved the way for a wide spectrum of applications that extend far beyond traditional military and recreational uses. The ability to operate drones Beyond Visual Line of Sight (BVLoS) has emerged as a critical enabler for unlocking the full potential of Unmanned Aerial Systems (UAS), driving significant advancements in various fields such as logistics, agriculture, infrastructure inspection, and emergency response.

Recent advancements in Internet of Things (IoT) architectures, miniaturization of onboard sensors, and communication technologies have revolutionized how data is collected, processed, and utilized in real-time. For instance, IoT-enabled BVLoS drones equipped with hyperspectral cameras, LiDAR, and Global Navigation Satellite Systems (GNSS) provide unparalleled capabilities for applications like precision agriculture, urban mapping, and disaster management. These drones can autonomously navigate complex environments, collect high-resolution environmental data, and perform tasks such as crop monitoring, damage assessment, or search-and-rescue missions in remote areas, as stated in [10].
Key enabling technologies such as sensor integration, data fusion, and AI-based algorithms have been instrumental in advancing BVLoS drone capabilities. Sensor fusion techniques, for example, combine data from multiple sources, including infrared cameras and LiDAR, to enhance navigation and obstacle detection even in adverse conditions.

From a regulatory perspective, EASA initiatives, such as the Joint Authorities for Rule-making on Unmanned Systems (JARUS), aim to establish a unified framework for the safe and reliable operation of drones. These regulations emphasize compliance with safety, privacy, communications, and environmental standards, which are essential for the integration of BVLoS drones into everyday business processes. Compliance with such frameworks is particularly critical for applications in urban areas, where the stakes for safety and privacy are higher, but also in rural areas, where communication is the main risk factor. This is mostly due to limited cellular coverage and the lack of essential ground-based communication infrastructure. Sparse or unreliable LTE and 5G networks can result in signal loss, hindering the ability to maintain control and transmit data effectively. Additionally, environmental factors such as dense forests, mountainous terrain, or large water bodies further disrupt communication signals, increasing operational risks.
The diverse use cases of BVLoS drones highlight their transformative potential:

- **Logistics and Delivery**: UAVs can streamline last-mile delivery by reaching remote areas and reducing congestion in urban settings. They offer solutions for transporting critical medical supplies to inaccessible locations or performing simultaneous multi-location deliveries.
- **Agriculture**: BVLoS drones facilitate precision farming in big fields, enabling tasks like crop monitoring, disease detection, and resource optimization,

ultimately increasing productivity and sustainability.

- **Emergency Response and Surveillance**: in disaster scenarios, advanced sensor-equipped drones provide critical situational awareness, expedite victim localization, and improve the effectiveness of rescue operations. Similarly, their use in public surveillance ensures better safety and risk mitigation during critical incidents.

While these applications demonstrate immense potential, they also present challenges, particularly in terms of performance, which includes ensuring reliable communication, maintaining operational stability over long distances, and achieving accurate navigation in complex environments. Performance issues can arise due to factors such as signal latency, position inaccuracies, or limited battery life, which can constrain the range and duration of BVLoS flights.
Balancing these conflicting requirements is crucial for scaling BVLoS operations to widespread adoption. For example, robust communication frameworks that leverage 4G/5G networks must guarantee low latency and high bandwidth, enabling drones to perform computationally intensive tasks like real-time video analysis or route optimization [11].

1.0.2 Thesis Objective & Structure of the document

This thesis builds on the concepts of the study described in the work [13]. It comes from advances in UAV technology and the increasing demand for their application Beyond Visual Line of Sight (BVLoS). The objective is to deepen the understanding of potential telecommunication risks during flight, focusing on path optimization to minimize the likelihood of issues during BVLoS operations, especially in suburban and urban areas where connectivity may present challenges. The Fig. 1.5 presents a simple schema of a possible scenario during a BVLoS flight, where the pilot/user is present only at the take-off. The thesis's goal is to find the best possible routes a drone can take during its flights, maintaining the best possible communication conditions even in rural areas, exploiting the GSM network. This work contributes to addressing these challenges by proposing a graph-based framework that encapsulates critical operational parameters, including connectivity quality and environmental constraints.
The methodology is based on the concept of a layered graph structure [13], which integrates diverse data inputs such as no-fly zones, population density, cellular infrastructure, and obstacle mapping. This allows to generate safe and dependable routes, leveraging existing cellular networks for seamless communication. Through rigorous experimental evaluations using real-world datasets, the framework demonstrates the possibility and feasibility of achieving BVLoS operations without necessitating new infrastructure investments.

Figure 1.5: Possible BVLoS scenario, involving an operator with limited visibility, image taken from[13].

In order to obtain the desired result, a simulator is exploited to create, analyze, and perform some computations on the layered-graph. The main structure of this document is briefly described as follows:

- Chapter 1: Introduction and presentation of the thesis objective.
- Chapter 2: Review of the state-of-the-art, and a comprehensive examination of the potential challenges resulting in a real-case scenario.
- Chapter 3: Presentation of the thesis work, specifically the preliminary phases involving the graph generation.
- Chapter 4: Illustrates the main methodology and the description of the scenarios.
- Chapter 5: The results are commented and conclusions drawn, highlighting possible future improvements.

Chapter 2

State-of-the-Art

In this chapter, we discuss the main technologies and paradigms presented in the literature. More specifically, we review the following aspects:

- Communication challenges in UAV Networks, discussing limitations for aerial users.
- Explanation of the channel model used to compute the signal path loss in the specific scenario.
- The usage of a graph-based solution to work in a 3D space, to generate the drone's path moving along 3 coordinates.

2.1 Communication Challenges in UAV Networks

Operating Unmanned Aerial Vehicles (UAVs) either being in Line of Sight or Beyond Visual Line of Sight (BVLoS) introduces significant communication challenges that must be addressed to ensure safe and efficient operations.
As highlighted in [14], UAVs traditionally rely on radio frequency bands such as 2.4 GHz and 5.8 GHz for pilot-to-drone communications. While effective for Visual Line of Sight (VLoS) operations, these bands face significant limitations in (BVLoS) scenarios, including restricted range and susceptibility to interference.

To overcome these challenges, leveraging existing cellular networks has emerged as a promising alternative. Cellular infrastructure, particularly 4G LTE and 5G, offers extensive coverage, higher bandwidth, and lower latency compared to traditional RF communication methods. The integration of UAVs with these networks not only expands their operational range but also enables advanced functionalities such as real-time video streaming, adaptive mission planning, and reliable command-and-control links. UAVs have been tested as aerial base stations to offload traffic during network congestion, enhancing overall capacity and coverage [16], [17]. For instance, in [15], UAVs demonstrated the ability to supplement terrestrial networks by providing reliable communication links during emergencies or in remote areas. This dual capability, both as users and enhancers of the cellular infrastructure,

underscores their potential in modern communication ecosystems. The ability of UAVs to act as communication relays between disconnected areas or as a means to extend network coverage in rural and remote regions highlights their unique advantages.

The reliance on cellular networks such as 4G and 5G for BVLoS operations is particularly promising. Cellular networks offer wide-area coverage, low latency, and high bandwidth, making them suitable for UAV applications where traditional communication methods fall short. However, challenges such as seamless handover during UAV mobility, interference management, and maintaining quality of service (QoS) persist, as highlighted in [17], as well as security issues and privacy loss, as stated in [18]. In this case study, we are considering real antennas distributed throughout the territory, assessing their specifications and the different technologies supported, evaluating how handovers may affect the paths and the goodness of the results in the final sections.

Energy consumption remains a critical challenge for UAVs, as also stated in [20], where the optimization of flight trajectories and communication protocols significantly improves operational efficiency. These considerations are vital for ensuring the feasibility of UAV-based applications in scenarios where continuous connectivity is paramount. In this work are considered the power and energy specifics of a commercial drone capable of performing BVLoS flights, but the main goal is to always guarantee a certain level of QoS in the communication, therefore the results will show how this priority will impact the UAV performances (section 4 & 5).

A possible solution to the energy consumption problems proposed in [19] involves establishing ad hoc UAV-specific networks by deploying drone hubs or warehouses close to demand points. These facilities serve as distribution centers for UAVs, enabling them to recharge, reload payloads, or exchange data. This approach has been explored extensively in logistics and disaster recovery, particularly for applications like medical supply delivery in remote areas. For example, the use of drone hubs allows UAVs to operate over shorter distances between the depot and the delivery point, reducing energy consumption and extending mission feasibility.

While this strategy mitigates the limitations of UAV energy capacity and enhances operational efficiency, it requires the creation of dedicated infrastructure. This includes identifying optimal hub locations, allocating UAV fleets, and maintaining facilities, which can be costly and logistically complex. Additionally, deploying ad-hoc networks may not always be feasible in dense urban areas or in regions with limited resources.
Given the challenges associated with deploying dedicated UAV networks, this work focuses on leveraging the existing cellular infrastructure. Transitioning from conventional pilot-drone communication to cellular networks introduces several advantages. First, it reduces the dependency on direct visual contact or radio links, thereby enabling more autonomous and scalable operations. Second, as mentioned before, leveraging existing cellular infrastructure eliminates the need for extensive

new investments, making it a cost-effective solution for expanding UAV capabilities [17].

2.2 Channel model in RMA environment

The primary focus of this section is to address the complexities associated with maintaining high-quality communication links between Ground Base Stations (GBSs) and drones during BVLoS operations. These challenges are particularly worsened in rural and suburban areas, categorized as Rural Macrocell (RMA) environments, where the signal quality is often poor due to sparse population and irregular distribution of cellular infrastructure. On the other hand, Urban Macrocell (UMA) environments provide a contrasting scenario, where signal quality is better due to dense infrastructure, although with increased risks of signal obstruction from tall buildings and urban clutter.

In RMA environments, maintaining reliable communication links is hindered by large inter-site distances and weaker signal reception. Rural Macrocell (RMA) environments are typically characterized by a low density of base stations, leading to gaps in coverage and weaker signal reception. The antenna lobes in such areas are designed to focus radiation on specific populated zones, often leaving sparsely populated regions with suboptimal coverage. This design choice introduces significant variability in communication reliability for UAVs operating in BVLoS mode.
Rural Macro environments exhibit specific propagation characteristics, including increased line-of-sight (LoS) probability over long distances and heightened influence of free-space path loss due to the reduced presence of scatterers. Studies such as [21] emphasize that the propagation models for RMA environments often adopt a dual-slope path loss model, where the breakpoint distance d_BP determines the transition between near-field and far-field propagation conditions. The LoS path loss model in RMA scenarios used in [21] is expressed in formula 2.1:

$$\mathrm{PL}_{\mathrm{LoS}} = 20\log_{10}(d) + 20\log_{10}(f_c) - 27.55, \quad \text{for } d \leq d_{\mathrm{BP}}, \tag{2.1}$$

where d is the distance between the transmitter and receiver in meters, f_c is the carrier frequency in GHz, and d_{BP} represents the breakpoint distance, determined by the heights of the transmitter and receiver.
For Non-Line of Sight (NLoS) conditions, additional losses due to diffraction and reflection dominate, requiring the inclusion of shadow fading parameters, as also highlighted in [22].

$$\mathrm{PL}_{\mathrm{NLoS}} = \mathrm{PL}_{\mathrm{LoS}} + \Delta_{\mathrm{NLoS}}, \tag{2.2}$$

where Δ_{NLoS} accounts for additional losses due to obstructions.
According to [23], RMA deployments typically involve macro base stations (with heights around 35 meters or above) covering large inter-site distances (1732 to 5000 meters).
Studies such as [24] further refine this model by including a correction factor (CF)

to account for environmental variations specific to RMA conditions. For instance:

$$\mathrm{PL}_{\mathrm{RMA}} = \mathrm{PL3}GPP + \mathrm{CF}_{\mathrm{RMA}}(d_{\mathrm{2D}}), \tag{2.3}$$

where d_2D represents the horizontal distance, and the CF varies across two segments with a breakpoint at 4 km:

$$\mathrm{CF}_{\mathrm{RMA}}(d_{\mathrm{2D}}) = \begin{cases} 2.8359 \log_{10}\left(\frac{1000}{d_{\mathrm{2D}}}\right) + 13.2785, & 1 \leq d_{\mathrm{2D}} \leq 4 \text{ km}, \\ 3.9745 \log_{10}\left(\frac{1000}{d_{\mathrm{2D}}}\right) + 13.9739, & 4 < d_{\mathrm{2D}} \leq 10 \text{ km}. \end{cases}$$

Conversely, UMA environments, characterized by dense infrastructure and higher population density, ensure better signal coverage but introduce challenges such as multipath propagation and increased interference, as figure 2.1 shows. In such scenarios, the LoS path loss model is again represented by [21]:

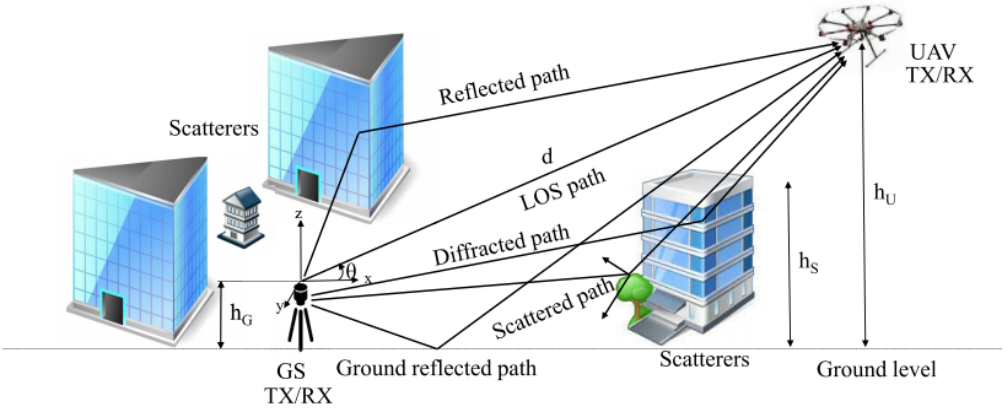

Figure 2.1: UMA air-to-ground propagation scenario, image taken from[22].

$$\mathrm{PL}_{\mathrm{LoS}} = 28 + 22 \log_{10}(d) + 20 \log_{10}(f_c), \tag{2.4}$$

while the NLoS path loss incorporates additional reflection and diffraction losses:

$$\mathrm{PL}_{\mathrm{NLoS}} = \max(\mathrm{PL}_{\mathrm{LoS}}, 13.54 + 39.08 \log_{10}(d) + 20 \log_{10}(f_c) - 0.6(h_{\mathrm{UT}} - 1.5)), \tag{2.5}$$

where h_{UT} is the height of the user terminal.
These models underscore the need to account for environmental and operational variables specific to each scenario. These variables are closely tied to the communication technologies employed—whether 4G LTE or 5G NR. Since this project is based on a real-case scenario, the technologies considered align with the infrastructure available in the test area, which includes 4G and 5G deployments.

In addition to evaluating signal quality, calculating the effective range of coverage of base stations in a suburban environment becomes critical. The channel model plays a pivotal role in obtaining accurate coverage estimates. In RMA environments, the coverage range of a tower is largely determined by the path loss model and the effective Signal-to-Noise Ratio (SNR) at the receiver. To compute the coverage range, it is essential to evaluate the effective SNR. In practical scenarios, the effective SNR depends on parameters such as the transmitter's output power (P_tx), the antenna gains at both ends (G_tx and G_rx), path loss (PL), and the noise floor at the receiver (N). In [25], where a coverage planning method performed in Nepal (rural and suburban areas) is evaluated, the relationship between the SNR and the powers is described as follows:

$$\mathrm{SNR_{eff}} = \mathrm{P}_{rx} + \mathrm{N}, \tag{2.6}$$

where the received power P_Rx is given by:

$$\mathrm{P_{rx}} = \mathrm{P}_{tx} + \mathrm{G_{tx}} + \mathrm{G_{rx}} - \mathrm{PL}), \tag{2.7}$$

The path loss (PL) is calculated using propagation models tailored to the deployment area. For RMA environments, the ITU-R and 3GPP TR 38.901 standards recommend models that include additional terms to account for environmental factors like building density and terrain height variations. In [25], the maximum path loss is calculated based on service throughput defined by the cell edge user. The same work also outlines a more complex coverage computation model, integrating link budget analyses. The link budget approach, which incorporates the *Cost231-Hata* model to estimate coverages, provides a practical method to assess base station placement and frequency allocation. This last model is beyond the scope of this paper as it takes into account factors present in urban realities and attenuation factors due to indoor tests.
In this work, the effective SNR for evaluating the coverage range and signal quality is computed using principles derived from the Shannon-Hartley theorem. This theorem provides a fundamental relationship between channel capacity, bandwidth, and SNR, enabling the calculation of SNR thresholds required to achieve a certain quality of communication. The approach is tailored to each type of antenna according to the guidelines outlined in the 3GPP TR 38.901 specification [23].
The Shannon-Hartley theorem states that the maximum achievable data rate (C) for a communication channel is given by:

$$C = B \log_2(1 + \mathrm{SNR}), \tag{2.8}$$

where:

- C: Channel capacity in bits per second (bps),
- B: Bandwidth of the channel in Hz,
- SNR: Signal-to-Noise Ratio (linear scale).

For this work, the objective is to identify the SNR threshold ($\mathrm{SNR_{th}}$) required to

maintain moderate communication quality, defined as achieving a specific channel capacity (C_{mod}) suitable for UAV operations. The evaluation of the effective SNR will be addressed again later in Section 4.

These models highlight the critical need for scenario-specific adjustments in channel modeling. This work integrates advanced propagation models for RMA scenarios from the 3GPP TR 38.901 framework [23]. This comprehensive model accounts for carrier frequency, antenna heights, and environment-specific factors such as building density and heights that will be further analyzed in Section 4. Furthermore, by optimizing flight paths and leveraging cellular infrastructure, the proposed framework aims to mitigate coverage gaps and enhance communication reliability in diverse operating conditions.

2.3 Graph-based layered solution

In the previous sections, an overview of the main challenges in a suburban environment for BVLoS flights was provided, particularly focusing on maintaining a reliable quality of service (QoS) in the communication channel. Beyond addressing these issues, it is equally crucial to define the foundational framework that enables efficient navigation and route planning for UAVs in 3D space.

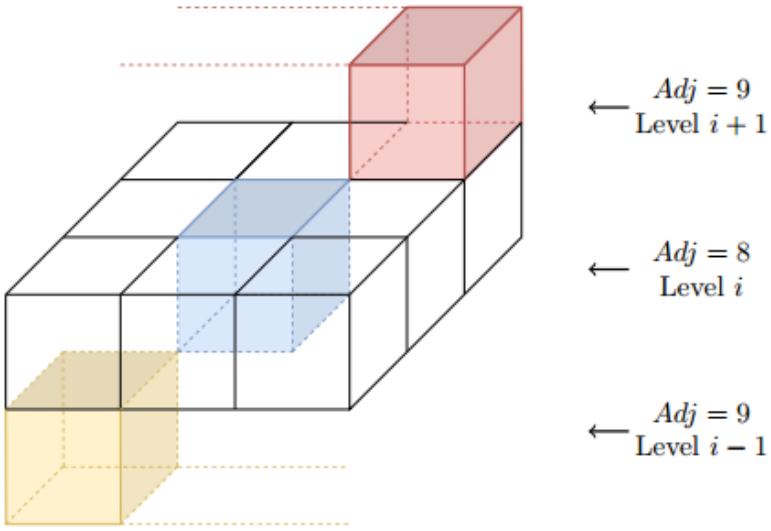

Figure 2.2: Example of adjacent cells in a discretized space, image taken from [13].

This work employs a multi-layered graph model, inspired by the approach initially presented in the paper [26]. The graph-based layered structure serves as the skeleton for mapping and organizing the 3D space into manageable and navigable segments,

where drones can travel safely and effectively. The space itself is then discretized into cells of fixed dimensions with a parallelepiped shape, as shown in figure 3.1. This model integrates spatial, environmental, and operational data, creating a flexible and scalable framework for BVLoS operations.

2.3.1 Multi-Layered Graph Representation

The multi-layered graph maps the 3D operational space by discretizing it into horizontal layers, each representing a specific altitude range. These layers are designed in [26] to capture different operational parameters and environmental constraints at different altitudes relevant to UAV navigation:

- **Obstacle Layer:** Represents physical obstacles such as buildings, trees, and other no-fly zones. This layer ensures collision-free paths by incorporating environmental data into the graph.
- **Wireless Infrastructure Layer:** Models the quality of communication with ground base stations, integrating parameters such as signal strength, path loss, and effective SNR.
- **Risk Map Layer:** Accounts for risks associated with UAV operations, such as population density and sensitive areas. This layer, while critical in urban scenarios, is excluded in this study due to the lower risk levels in rural and suburban environments.

Each layer is populated with nodes representing the centroids of 3D geo-referenced cells and edges connecting these nodes to indicate possible movement paths. The edges are weighted according to key operational parameters in order to solve the *Maximum Dependability Path Problem* (MDP2), as explained in more detail in [13]. These includes:

- **Connectivity Quality:** Derived from the channel model and effective SNR evaluations at the given altitude and position.
- **Risk Assessment:** Incorporating factors such as population density and potential obstacles, as detailed in [13].
- **Energy Efficiency:** Calculating the energy consumption to cross the edge, which varies with altitude and distance.

The integration of these weights allows for the development of cost-efficient and risk-averse routes while maintaining strong communication links throughout the UAV's flight. Each cell is evaluated for the attributes mentioned above (connectivity, risk, and energy cost) which are then used to populate the nodes and edges of the graph. The resulting structure provides a comprehensive 3D map of the operational space, enabling the UAV to navigate autonomously through the defined corridors.

This layered structure introduces several advantages:

- **Scalability:** The multi-layered representation simplifies the division of the 3D space, making it easier to integrate additional data, such as new environmental constraints or updated communication parameters.
- **Dynamic Adaptation:** By dynamically adjusting edge weights based on real-time data, the graph allows for responsive route planning, accommodating changes in connectivity, weather conditions, or obstacles.
- **Risk Mitigation:** The risk-aware routing capability reduces the likelihood of UAV failures or accidents by prioritizing safer paths with lower risk indices.

A related approach, investigated in [27], explores a two-layer path planning model for cooperative Ground Vehicle (GV) and UAV systems. In this model, a GV acts as a mobile depot, facilitating UAV operations by transporting the drone between discrete target areas and providing recharging or battery replacement.
While this approach enhances UAV endurance and operational efficiency, it introduces significant constraints, such as requiring an additional vehicle and optimizing the cooperative paths of both the UAV and GV simultaneously. This dependency limits its applicability in scenarios where deploying an auxiliary ground vehicle is infeasible or inefficient.

Similarly, [28] presents a comprehensive survey of UAV path planning techniques in 3D environments, emphasizing factors such as collision avoidance, energy efficiency, and cost optimization. These studies highlight the importance of finding optimal paths to minimize energy consumption and operational costs. However, they primarily focus on navigation and obstacle avoidance without addressing the optimization of communication quality.

In contrast, the current work integrates communication parameters directly into the graph framework, optimizing both the path planning and the quality of the communication channel. This ensures that UAVs maintain robust links with ground base stations throughout their routes, a feature not explored in the studies cited above.

By discretizing the 3D space and generating navigable corridors, this work establishes a comprehensive map for UAV operations. This graph-based representation provides a scalable and adaptive solution for BVLoS operations, ensuring that the UAV can navigate safely and maintain optimal communication with ground infrastructure.
This research primarily focuses on the Obstacle and Wireless Infrastructure layers of the graph. The Obstacle layer defines collision-free paths, as further detailed in Section 3, while the Wireless Infrastructure layer ensures optimal communication, as described in Section 4. The Risk Map layer is excluded, as the rural and suburban nature of the selected environment inherently mitigates the risks associated with human impact.

Chapter 3

Preliminary Steps

The case study presented in this work focuses on the suburban city of Mappano, located in the metropolitan area of Turin, Italy. This area is chosen for its diverse topographical features and multiple BSs, which align with the objectives of this research. In order to make the simulation as loyal as possible to real world cases, the test area encompasses a total of 247 ground base stations (GBSs) operated by various telecommunications providers, including WindTre, Vodafone, TIM, Iliad, and Zefiro. They are distributed over 8 different positions on the map, as shows the in figure 3.1. This configuration is maintained over all the scenarios.
Additionally, the distribution of antenna heights for both 4G and 5G base stations is illustrated in Figure 3.2. This analysis provides insight into the vertical positioning of antennas, which plays a crucial role in determining coverage, signal propagation, and the effectiveness of UAV communication in BVLoS operations. In the figure, the left histogram represents the height distribution of 4G antennas, while the right histogram corresponds to 5G antennas. The x-axis in both plots denotes the antenna height in meters, while the y-axis represents the count of base stations at each height level. The blue bars illustrate the frequency of 4G base station heights, whereas the red bars represent the distribution of 5G base station heights. The distribution highlights that 4G base stations are more prevalent and exhibit a wider range of heights compared to 5G base stations, which are fewer and appear to be installed at lower altitudes on average.
This difference in height distribution impacts signal propagation characteristics, as higher base stations tend to have wider coverage but may experience increased path loss. In contrast, lower 5G antennas might be optimized for urban environments with smaller cell sizes and higher frequencies, requiring a denser deployment for effective coverage.

These base stations support a wide range of technologies, including 4G and 5G, across multiple frequency bands (700 MHz, 800 MHz, 1800 MHz, 2100 MHz, and 2600 MHz). The data for these base stations, such as their locations, supported technologies, and operational parameters, are retrieved from *LTE Italy* [30] website.

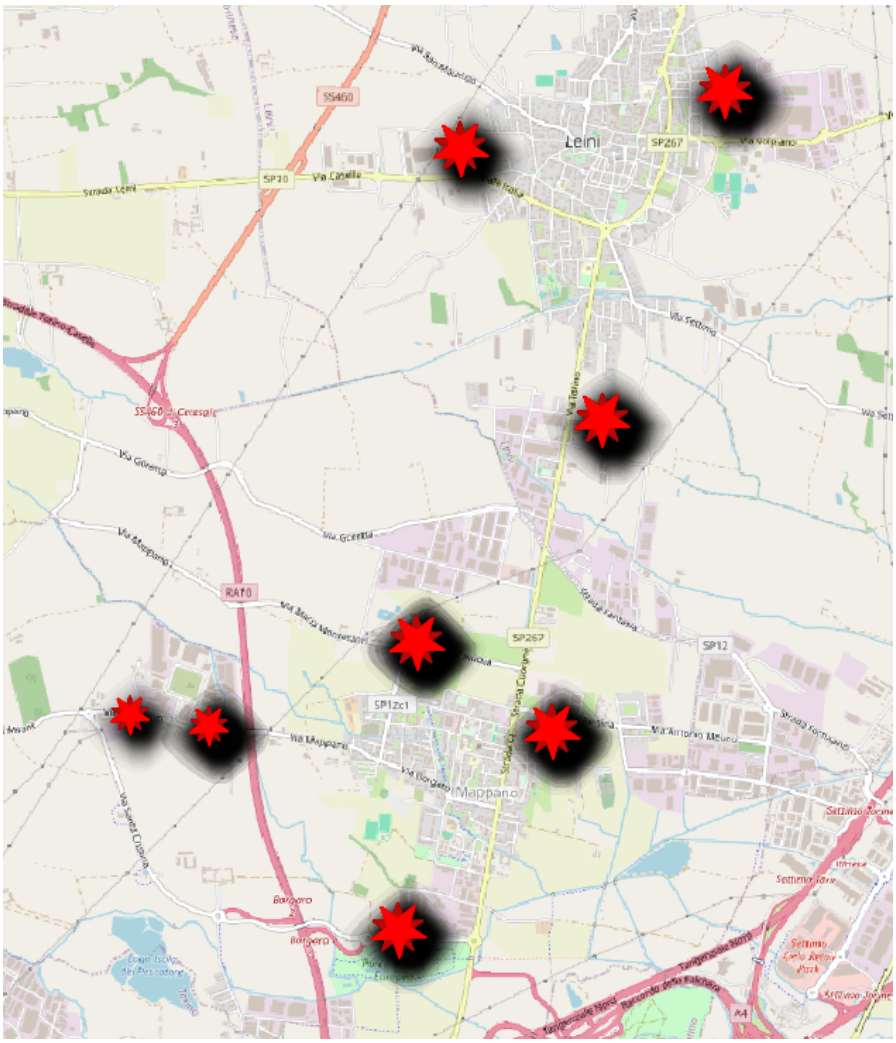

Figure 3.1: Base station position on the map.

LTE Italy Network aims to provide information about mobile network coverage in Italy, specifically focusing on 4G LTE, being a crowdsourced database of network coverage information. A sample of the data includes the following parameters:

- **ID:** Unique identifier for the base station.
- **Supported Technologies:** E.g., 5G, 4G.
- **ARFCN:** Absolute Radio Frequency Channel Number.
- **Geographical Coordinates:** Latitude and longitude of the base station.
- **Cell Name:** Identifier for the cell tower (e.g., "B1 S1 DSS Mappano Via Cà Nuova").
- **Layer and Height:** Corresponding operational layer (Italy telephone operator) and the height of the base station antenna.

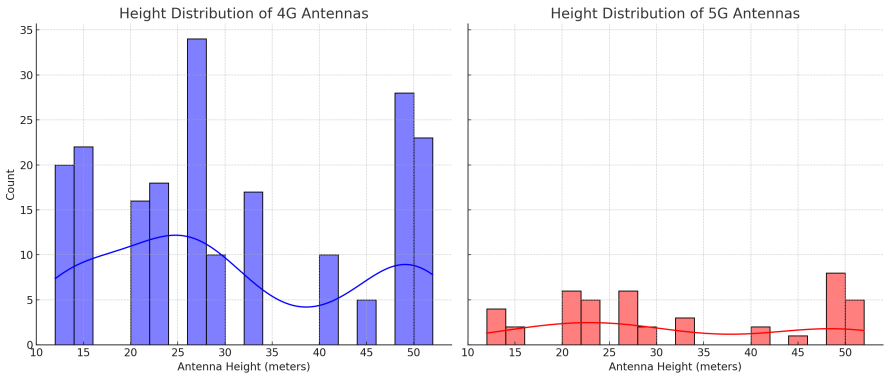

Figure 3.2: BSs heights distribution

These realistic parameters serve as the foundation for modeling the wireless communication layer and are integral to the simulations conducted in this study.

Further in this chapter, every aspect of the preliminary analysis will be taken into account and described, starting from the description of the initial input files and following up with the generation of the main data input for the simulator.

3.0.1 Digital Elevation Model (DEM)

A key component of this research involves the utilization of a **Digital Elevation Model** (DEM) to characterize the test area. The DEM provides detailed altitude information for each geographical point in the area, enabling the identification of potential obstacles for UAV operations.
The initial DEM dataset is provided by the Department of Civil Engineering (DISAT) at Politecnico di Torino. However, since certain base stations are located outside the bounds of this dataset, it is supplemented with regional DEM data obtained from the Geoportal of Piemonte Region, taken from the source [31].

For consistency, the altitude data within the DEM are adjusted to set the minimum altitude found in the dataset as the reference ground level (0 meters). This adjustment simplifies the processing and ensures uniformity across the simulations. For the default configuration, the minimum altitude is set to 220.18 m above mean sea level. For smaller test areas, such as those used in specific simulations, the minimum altitude is recalculated, with the value set to 223.3 m.
It is important to note that areas below the defined ground level, such as rivers or lakes, are also considered at 0 meters, as UAVs are not expected to operate from these regions.

The DEM plays a pivotal role in generating the foundational elements of the simulator: the **3D matrix** and the **basic graph**. By discretizing the geographical area into grid cells, the DEM provides altitude data at each cell, indicating the presence or absence of obstacles. This approach ensures that the 3D representation of the test area accurately reflects the real-world topography and is optimized for

UAV navigation and communication.
The methodology for processing the DEM is as follows:

1. **Discretization:** The DEM is divided into a grid, with each cell representing a 10m x 10m area horizontally and 30m vertically in the default scenario.
2. **Obstacle Identification:** Cells with altitudes below the defined DEM level are marked as containing obstacles.
3. **Integration:** The DEM data are integrated with shapefiles, which define the boundaries of the test area, ensuring that only relevant regions are considered.

This processed DEM serves as the foundation for creating both the 3D matrix, which stores obstacle information, and the basic graph, which defines initial node connectivity. These elements are further detailed in the following sections.

3.1 Generation of the 3D Matrix

The 3D matrix serves as a fundamental component of the simulator, representing the discretized 3D space of the test area and capturing critical information regarding obstacles. Its primary purpose is to facilitate UAV navigation and communication analysis by providing a structured and realistic representation of the environment. The structure and generation of the 3D matrix are inspired by the methodologies outlined in [13], ensuring that the model adheres to recognized standards for simulating UAV communication environments.

3.1.1 Structure and Purpose of the 3D Matrix

The 3D matrix discretizes the test area into small cubic cells, each representing a $10\,\mathrm{m} \times 10\,\mathrm{m} \times 30\,\mathrm{m}$ space in the default configuration. Every cell contains information about its geographical location, altitude, and whether it contains an obstacle or not. This structure enables a layered representation of the environment, with each layer corresponding to a specific altitude. By dividing the area into manageable units, the matrix provides a scalable and efficient way to model the 3D operational space for UAVs.

The 3D matrix is used for the following purposes:

- Identifying obstacle-free cells that are safe for UAV navigation.
- Providing altitude-specific information to facilitate the generation of the basic graph.
- Serving as a reference for determining communication parameters such as line-of-sight (LoS) and signal quality between UAVs and ground base stations.
- Serving as a simpler structure than the graph itself to perform obstacle-detecting computations.

3.1.2 Creation of the 3D Matrix

The generation of the 3D matrix begins with the processed Digital Elevation Model (DEM) and shape files described in the previous section. A Python script together with QGIS tools are used to automate this process. The steps for generating the matrix are as follows:

1. **Grid Initialization:** The geographical area is divided into a 3D grid of cells, having each cell assigned a unique identifier based on its coordinates.
2. **Altitude Assignment:** For each cell, the DEM is queried to determine the presence of possible obstacles. This altitude is compared with the altitude level indicated by the DEM at that specific geographical location.
3. **Obstacle Marking:** Cells with altitudes below the level specified by the DEM are marked as containing obstacles. In contrast, cells at or above the DEM level are marked as obstacle-free.
4. **Boundary Validation:** The shape files are used to exclude cells outside the defined test area, ensuring that only relevant regions are included in the matrix.

The resulting matrix is a three-dimensional array where each element corresponds to a cell. For the default configuration, there are 3 z-layers of discretization, while for the smaller but more discretized scenario, we can find 9 altitude layers. The value of each element indicates whether the cell contains an obstacle (`1`) or is obstacle-free (`0`), schematically represented in figure 3.3.

Figure 3.3: 3D Matrix representation.

The 3D matrix forms the foundation for creating the basic graph, which represents the connectivity between cells in the 3D space. It is also used to evaluate line-of-sight conditions and calculate communication parameters, as described in [13]. By providing a detailed representation of the environment, the matrix ensures that the simulator accurately models real-world conditions and supports robust UAV operations.

3.2 Creation of the Graph

Following the generation of the 3D matrix, the next steps involve the construction of the basic graph, which serves as the skeletal structure of the simulator. This graph is derived directly from the 3D matrix and provides an initial representation of the test area's connectivity. Each node in the graph corresponds to a cell in the 3D matrix, and edges represent potential paths between adjacent cells. In figures 3.4 and 3.5, the blue points indicate the obstacle-free nodes, the red ones those containing possible obstacles, while, where allowed, the orange lines represent the edges among cells.

3.2.1 Purpose and Role of the Basic Graph

The basic graph is a foundational component of this work, representing the initial 3D connectivity of the test area based on the previously generated 3D matrix. Each node in the graph corresponds to a cell in the 3D matrix, and edges denote possible paths the UAV can traverse. The graph structure is crucial for simulating UAV navigation, ensuring the drone can safely take off, avoid obstacles, and land in the designated area.
The default graph initially includes three altitude layers, as shown the figure 3.4, and only a subset of edges with no weights; these are added in subsequent steps as part of the simulator's refinement process.

The basic graph is used to:

- Model the 3D connectivity of the test area, enabling UAVs to navigate through obstacle-free corridors (the orange lines in figures 3.4 and 3.5).
- Serve as the input for adding weights based on communication quality and shortest distance parameters, that will be seen in later chapters.
- Provide an efficient representation of the test area for pathfinding and optimization algorithms.

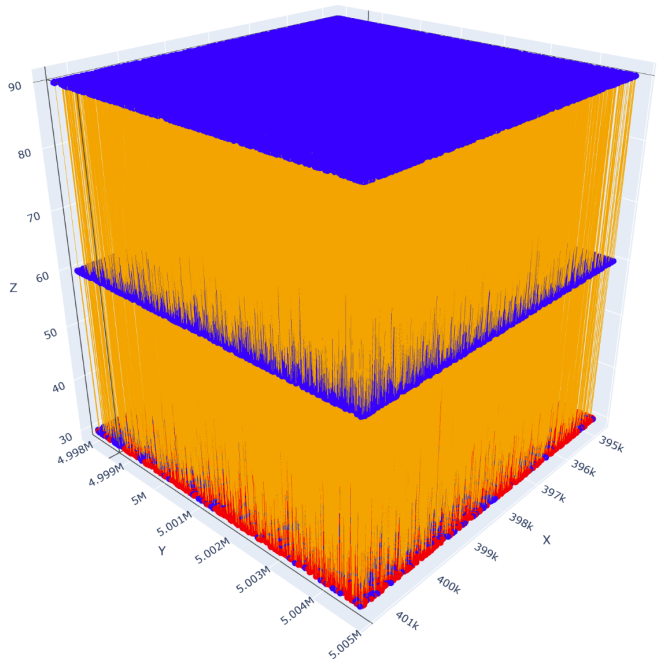

Figure 3.4: 3 layered graph - Default configuration on total area

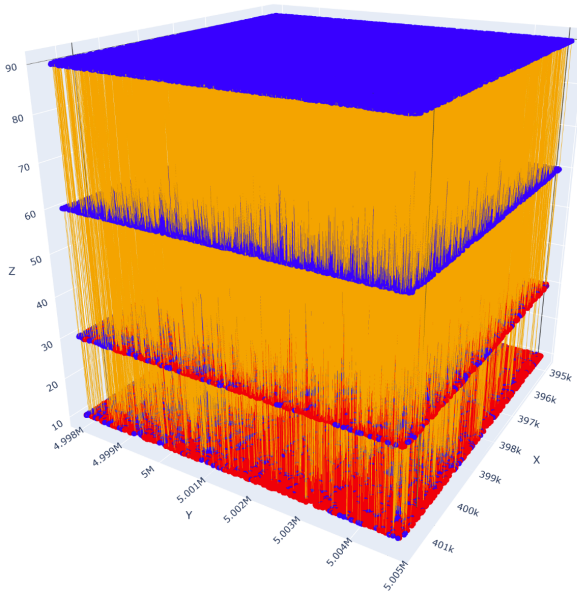

(a) 4 layered graph - total area

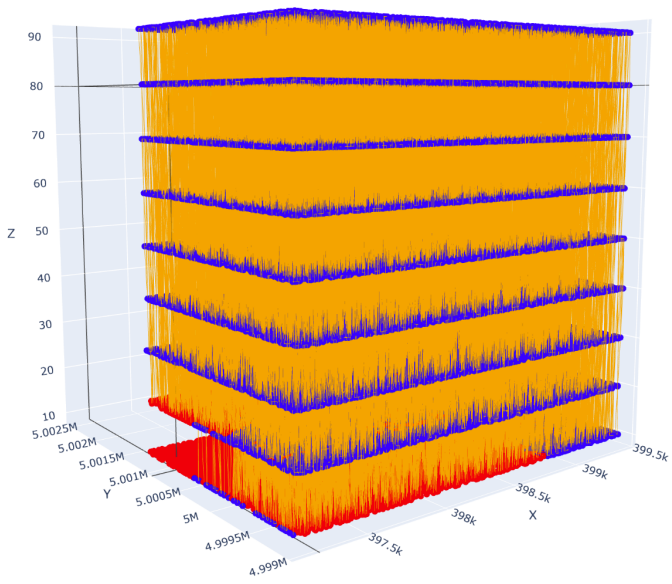

(b) 9 layered graph - smaller urban area

Figure 3.5: 3D layered Graphs

3.2.2 Graph Construction Process

A Python script automates the creation of the graph by processing the 3D matrix. The main steps are depicted in the flow chart 3.6 and explained in detail as follows:

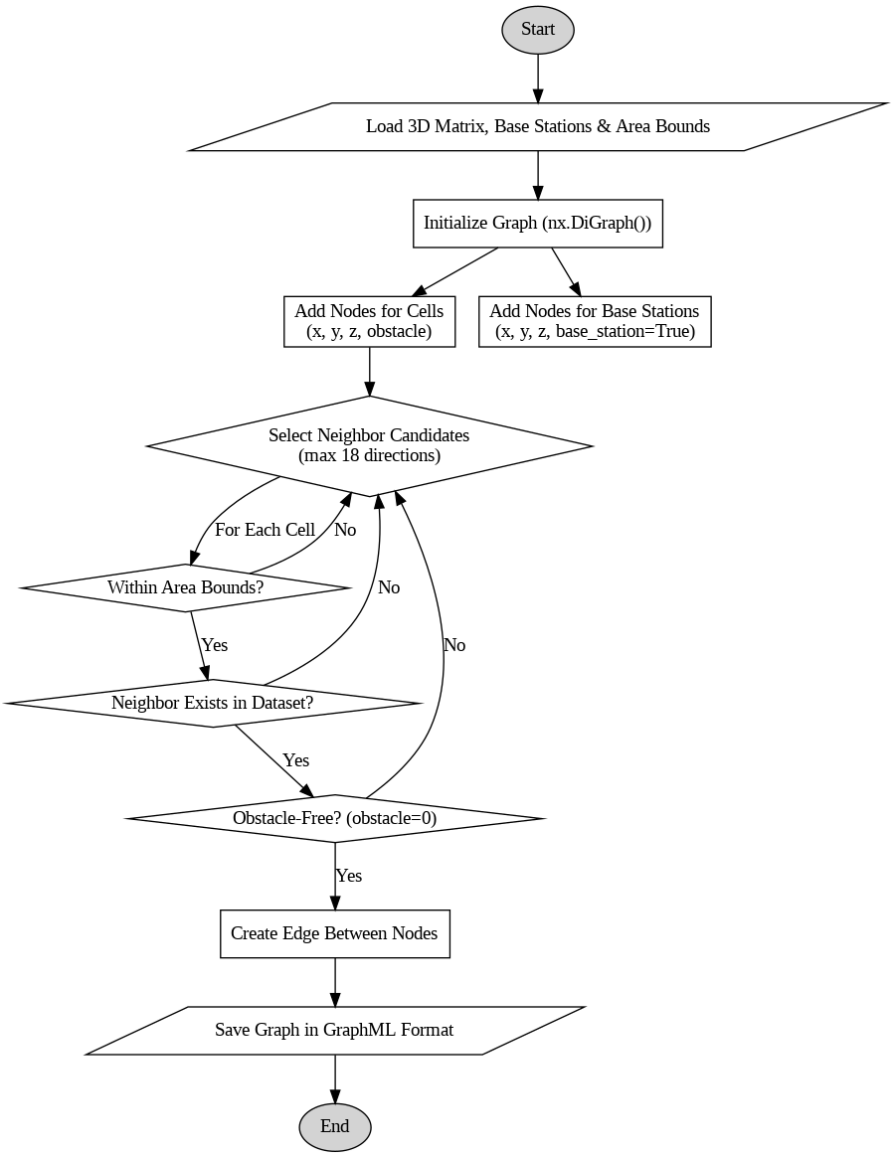

Figure 3.6: Flowchart main graph creation steps

1. **Node Initialization:** Each cell in the 3D matrix is mapped to a unique node in the graph. The node's attributes in the preliminary step include only its coordinates (x, y, z) and obstacle status (0 for obstacle-free, 1 for obstacle).

2. **Edge Generation:** Edges are created between adjacent nodes that respect specific criteria. Adjacency is determined in six directions: up, down, left, right, forward, and backward, corresponding to the cell's neighbors in the 3D matrix.

3. **Boundary Handling:** Cells at the edges of the test area are connected only to neighbors within the matrix bounds, ensuring the graph does not reference non-existent nodes.

4. **Obstacle Exclusion:** Nodes marked as obstacles in the 3D matrix are excluded from edge creation except in certain circumstances seen in the next chapter, ensuring that UAVs avoid these regions during navigation.

The resulting graph $G = (V, E)$ is represented as a set of nodes and edges, where:

- **Nodes (V):** As mentioned before, each cell in the 3D matrix is mapped to a unique node, identified by its coordinates (x, y, z). The nodes inherit the attributes of the corresponding matrix cells. Each node can have up to 18 neighbors, 6 that share a face (face-adjacent), and 12 neighbors that share only a side (edge-adjacent).

  The decision to allow connectivity up to 18 neighbors ensures flexibility in UAV navigation, particularly in 3D spaces where avoiding obstacles may require considering multiple movement directions.

- **Edges (E):** Edges represent the connectivity between neighboring nodes and are mono directional, capturing the direction of potential UAV movement by following the criterias specified below.

Edges are created based on the attributes of the source and target nodes, following specific criteria designed to reflect realistic UAV behavior:

- **Obstacle-free cells (`obstacle` $= 0$):**
  - If the neighbor is also obstacle-free (`obstacle` $= 0$) and covered by at least a BS (`no_cover` $= 0$), a normal edge is created with a positive weight.
  - If the neighbor is obstacle-free but uncovered (`no_cover` $= 1$), an edge is created, but its weight is set to infinite, reflecting limited communication reliability.
  - If the neighbor contains an obstacle (`obstacle` $= 1$), no edge is created, as UAVs are designed to avoid entering cells with obstacles, unless this node is the destination point. In this case is supposed to have the support of a user/pilot.
- **Cells with obstacles (`obstacle` $= 1$):**
  - Outgoing edges are allowed only to obstacle-free neighbors:
    - If the neighbor is obstacle-free and covered (`no_cover` $= 0$), a normal edge is created. This might be the case of a starting cell with an obstacle towards the destination.
    - If the neighbor is obstacle-free but uncovered (`no_cover` $= 1$), an edge is created with infinite weight.
  - No incoming edges are allowed to nodes with obstacles, as UAVs cannot safely land or navigate into such cells.

This set of criteria ensures that UAVs prioritize paths through safe, obstacle-free

areas while accounting for communication constraints. The exclusion of incoming edges into obstacle-containing cells reflects the UAV's operational constraints, where obstacles may impede both navigation and safe landing.

Mathematically, the graph $G = (V, E)$ is defined as:

$$V = \{v_i \mid i \in \text{cells in the 3D matrix}\}, \tag{3.1}$$

where v_i represents a node corresponding to a cell, and:

$$E = \{(v_i, v_j) \mid v_i, v_j \in V, \text{ and } v_i \text{ and } v_j \text{ are adjacent and obstacle-free}\}. \tag{3.2}$$

By leveraging the 3D matrix and DEM data, the basic graph ensures an accurate and realistic representation of the test area's spatial and connectivity characteristics, forming the backbone of the simulation framework.

3.2.3 Different Graph Configurations and Scenarios

Three different graph configurations are generated to analyze UAV path planning under varying discretization levels and operational constraints. Each graph includes the municipal administrative boundaries of Mappano along with portions of adjacent municipalities, except for the smallest graph, which focuses on the most densely populated area.

The first and most detailed graph represents the entire test area with **three altitude layers** set at 30, 60, and 90 meters above the ground. The fixed cell size is $10 \times 10 \times 30$ meters, ensuring fine-grained discretization of the airspace. The total area covered by this graph is 45.88 km^2, with:

- **Number of nodes:** 1,374,707
- **Number of edges:** 16,667,454

The second graph extends the default configuration by introducing a new altitude layer at 10 meters, resulting in **four layers**: 10, 30, 60, and 90 meters. This configuration allows for an additional level of analysis at near-ground UAV operations. The cell size at the lowest layer is $10 \times 10 \times 10$, while the higher layers retain $10 \times 10 \times 30$. The total area remains 45.88 km^2, with:

- **Number of nodes:** 1,832,936
- **Number of edges:** 18,521,802

The third and smallest graph covers a highly urbanized subregion of 4.86 km^2, offering the highest resolution. It features **nine altitude layers** distributed every 10 meters, from 10 to 90 meters. Each cell has a fixed size of $10 \times 10 \times 10$, enabling a highly granular representation of the 3D airspace. This setup allows for a more detailed analysis of UAV path selection in urban settings, where more height options exist for navigation. The graph properties are:

- **Number of nodes:** 440,588
- **Number of edges:** 6,603,629

In table 3.1 provides a numerical summary of the three graph configurations:

Graph	Area (km^2)	Altitude Layers	Cell Size (m)	Nodes	Edges
Default Graph	45.88	3 (30, 60, 90)	$10 \times 10 \times 30$	1,374,707	16,667,454
Four-Layer Graph	45.88	4 (10, 30, 60, 90)	Mixed ($10 \times 10 \times 10$ at lowest)	1,832,936	18,521,802
Smallest Graph	4.86	9 (10-90)	$10 \times 10 \times 10$	440,588	6,603,629

Table 3.1: Summary of the generated graph configurations.

These three configurations allow for extensive testing of UAV navigation under different levels of discretization and airspace constraints, ensuring robust validation of the proposed methodology.

The graphs serve as the foundation for further refinements, such as adding edge weights based on communication quality, risk assessment, and other factors. By modeling the connectivity of the test area, it provides a scalable framework for UAV navigation and supports the simulator's goal of ensuring safe and efficient BVLoS operations.

Chapter 4

Methodology

As already mentioned in section 1 and 3, in order to guarantee a certain level of QoS for the communication between UAV-BS during the flight, it is necessary to define the most realistic channel model for RMA scenarios.
The methodology adopted in this work is structured around a two-step approach aimed at modeling and analyzing UAV communication in a BVLoS scenario. This process is built upon the pre-processed data derived from the DEM, shape files defining the study area, and the basic graph representation of the 3D environment.

An ad-hoc simulator is developed as the principal tool from here onward, entirely programmed in Python. This choice is motivated by Python's flexibility as an object-oriented language and its extensive ecosystem of libraries, including *networkx* for graph-based modeling, *rtree* for efficient spatial indexing, and other scientific computing libraries that facilitate geospatial and signal processing operations. The modular nature of Python allows for streamlined implementation, testing, and optimization of the proposed methodology.

The core objective of the methodology is to assign meaningful attributes to the nodes and edges of the graph-based representation of the 3D space. This is achieved through an incremental approach, where each step progressively refines the level of information embedded within the graph. The first phase focuses on determining the coverage area of each BS by computing the expected path loss for each cell within its range. This involves evaluating the propagation characteristics of the signal in relation to environmental factors, including terrain elevation and obstacles derived from the DEM.
Once the coverage map has been established, the second phase enhances the graph structure by defining the connectivity between nodes and assigning weights to the edges. These weights represent the feasibility and cost of transitioning from one node to another, incorporating key parameters such as signal quality, potential obstructions, and flight constraints. The ultimate goal is to produce a structured representation of the UAV flight space that enables optimal path selection while ensuring reliable communication links.

As already mentioned in the previous chapters, to ensure the simulation remains

as faithful as possible to real-world conditions, the actual distribution and technical specifications of BSs are incorporated. Additionally, obstacle distribution is accurately mapped using real-world DEM data and shape files, allowing for precise modeling of environmental constraints affecting UAV flight paths and signal propagation. A simple graph presented in figure 4.1 summarizes all the needed input data, as well as the final output obtained once all the computations are done.

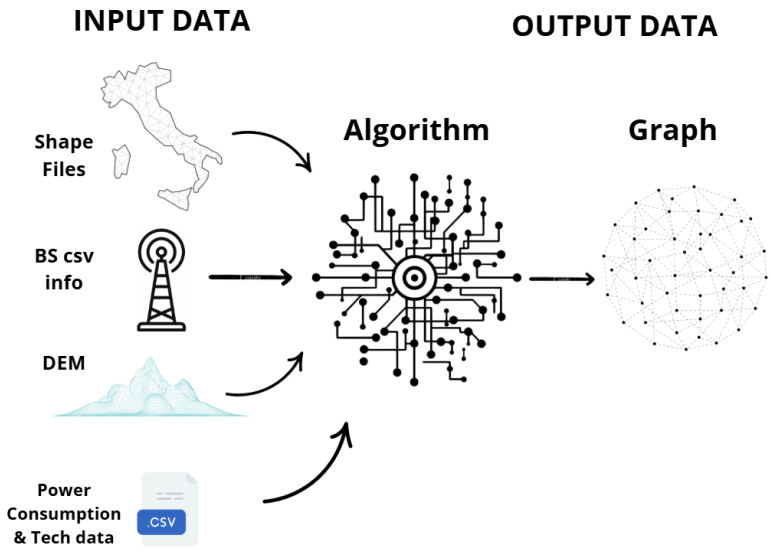

Figure 4.1: Graph to summarize Input and Output data of the algorithm

This chapter provides an in-depth explanation of the two main phases of the methodology, highlighting the considerations made during the implementation and the key challenges addressed to accurately model real-world UAV operations. The subsequent sections will detail the processes involved in computing the coverage range, assigning path loss values, and defining edge weights to create a dynamic and realistic network representation.

4.1 General Algorithm description

In this section, we describe the overall algorithm used in our study. The algorithm consists of multiple phases, each performing a specific task related to network modeling and path optimization. The first phase focuses on calculating the channel model for the cells in the graph.

The first step of the algorithm involves computing the coverage radius of all BSs present in the area (see step 2 figure 4.2. Then, it iteratively selects all cells n where the ‘obstacle‘ field is set to 0 (see step 3 in 4.2), indicating that they are free of obstacles and can be traversed.
It should be specified that for *cell* n is intended the physical portion of volume in space that occupies a dimension of 10x10x30 in the standard case, and 10x10x10 in the more discrete case.

For each selected cell n, the algorithm evaluates whether it falls within the coverage radius of any BS (see steps 4 and 6 in 4.2). Additionally, a flag "*no_ cover*" is set to indicate whether *cell n* is covered by at least one BS (see step 5 in 4.2). If after the computation the cell is not in the range of any antenna, this flag will be set to 1 and the final weigth will be computed accordingly as explained later.

The process follows these steps:

- Select a cell n with 'obstacle = 0'.
- Check whether at least one BS covers cell n. If no BS covers the cell and the 'no_cover' flag remains set to 1, the cell is marked as uncovered, and the next cell is processed.
- If cell n is covered by a BS, determine whether the BS is in LoS or NLoS conditions (see step 7 in 4.2).
- Compute the Path Loss (PL) using the appropriate formula.
- If the computed PL exceeds the maximum acceptable PL, the algorithm moves to the next BS in the list. Otherwise, the 'no_cover' flag is set to 0, and the computed PL is appended to a list associated with the BS (see steps 8 and 9 in 4.2).
- If additional BSs remain to be checked (step 11 in 4.2), repeat the process from step 4 in figure 4.2. Otherwise, sort the PL values in ascending order (step 10 in 4.2).

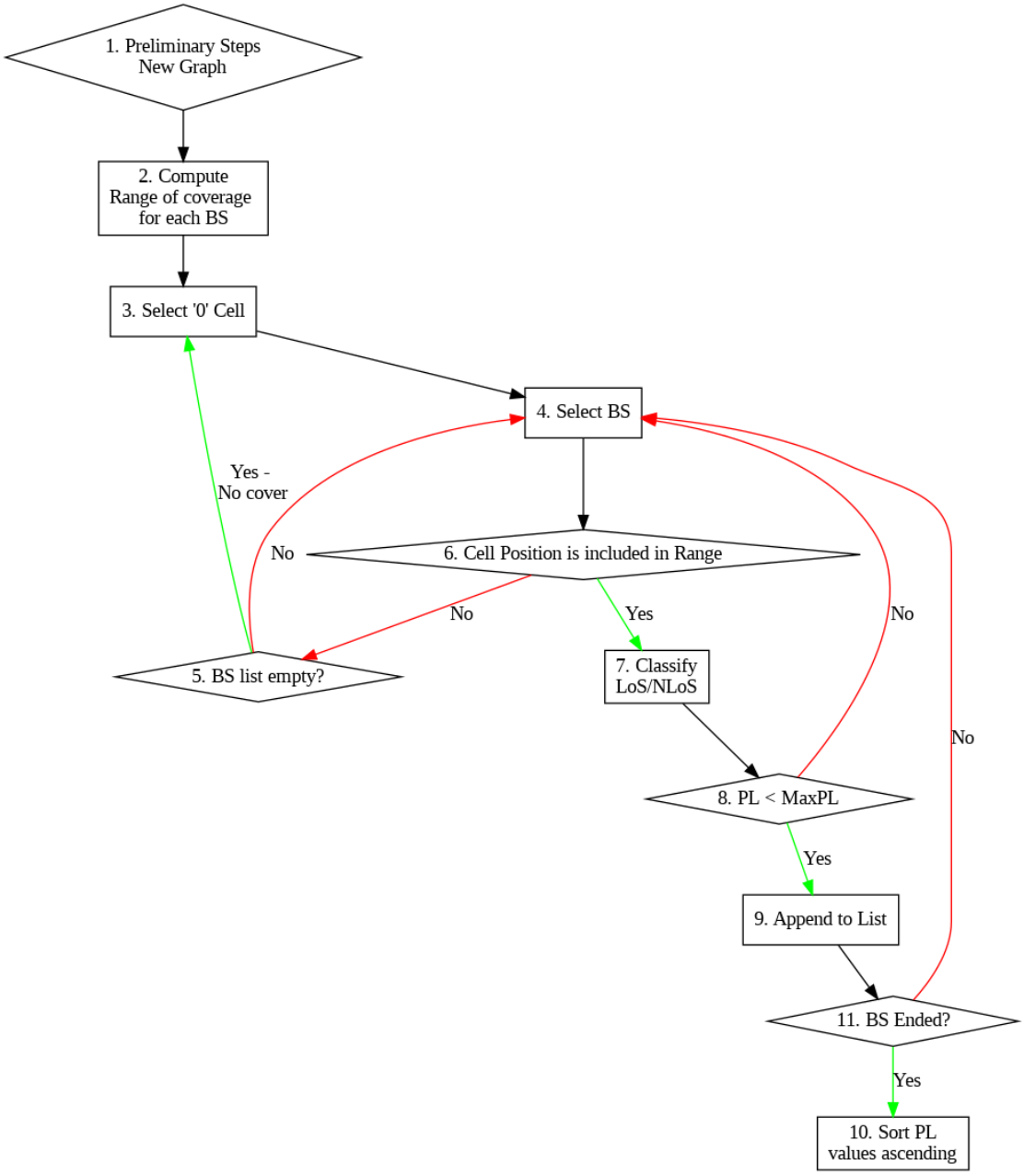

Figure 4.2: Flowchart of Phase 1: Channel Model Computation.

The flowchart illustrating this process is shown in Figure 4.2.

In the second phase, weights are assigned to the graph edges based on the computed PL values. The algorithm selects all obstacle-free nodes (see step 2 in 4.3) and evaluates only edges connecting neighboring cells that also satisfy this condition (see steps 3 and 4 in 4.3). In this case, the nodes represent the centroid of each geographical cell, which means that the algorithm will select, as before, all those cells that have as property the '*obstacle=0*'
The steps include:

- Selecting the neighboring cells, having as constraint the maximum of 18

possible adjacent cells (step 6 in 4.3). This means that at best the 18 edges may exit from *cell n*.

- Extracting the smallest PL value from the sorted list of the neighboring cell n' (see step 5 in 4.3).
- If the BS of n' matches the BS of n (step 7 in 4.3), (meaning they correspond to the same tower) compute the weight (see step 12 in 4.3) using the ratio:

$$\text{ratio} = \frac{PL(n)}{PL(n')} \tag{4.1}$$

  followed by scaling and normalization processes, explained in the next section (step 13 in 4.3).
- If the BS of n' is different and 'no_cover = 0', an inter-cell handover is triggered, and a penalty is applied to the weight computation (see steps 9 and 10 in 4.3). This quantity will be explained later in 4.19.
- If flag 'no_cover = 1', the transition weight to that cell is set to inf, as it is an uncovered cell (see step 11 in 4.3).

A flowchart illustrating this phase is provided in Figure 4.3.

The next sections will further analyze each step that the algorithm does, paying particular attention to the ad hoc channel model used and the corresponding equations.

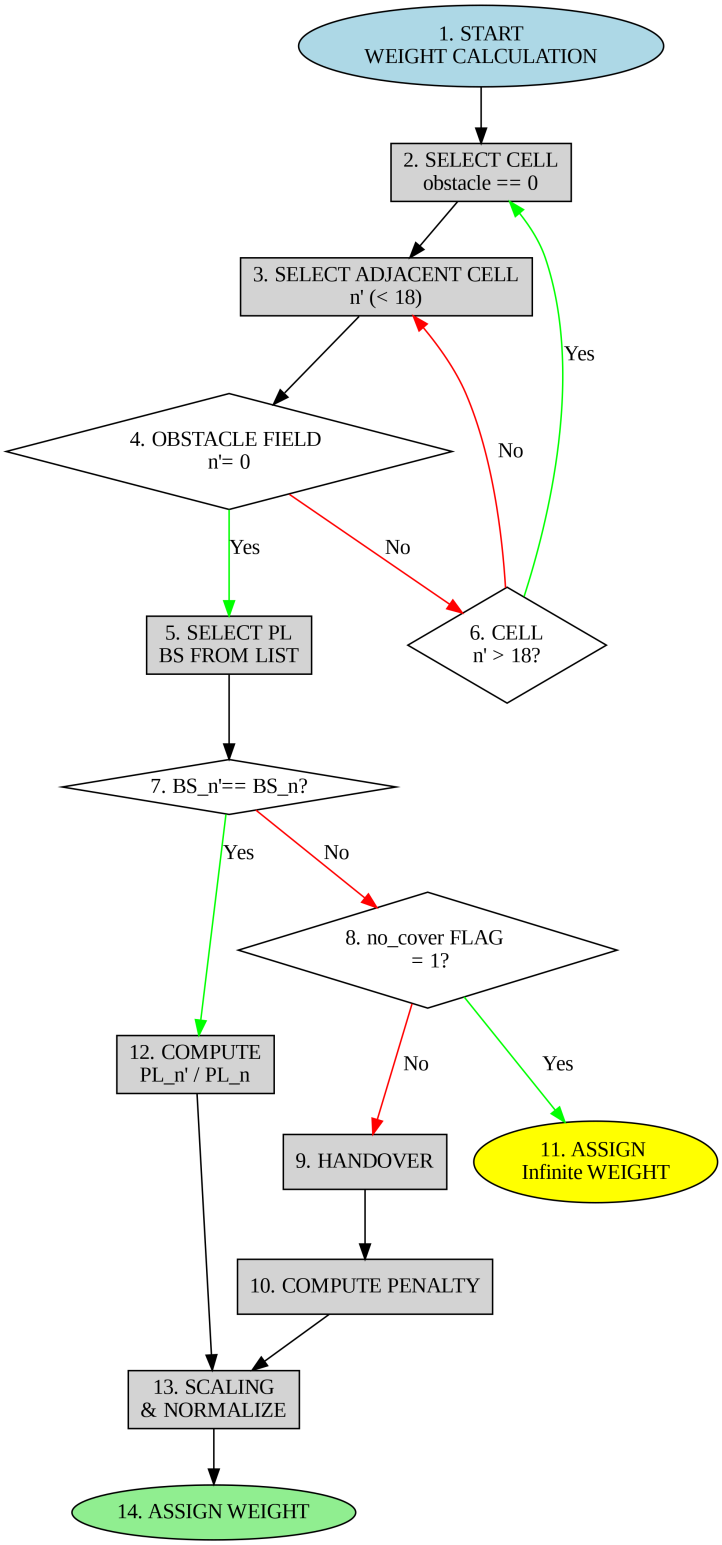

Figure 4.3: Flowchart of Phase 2: Edge property definition and weights assignment.

4.2 Phase 1: Network Coverage and Path Loss Calculation

The first part of the simulator is dedicated to assessing the network coverage over the study area and determining the path loss experienced by UAVs at different positions within the graph. This step is crucial in ensuring that the drone can maintain reliable communication links with BSs throughout its flight. The overall process consists of three main components: preprocessing input data, computing the range of coverage for each BS, and calculating the path loss under LoS and NLoS conditions.
The approach ensures that, for each cell, it will be possible to retrieve the necessary information to evaluate and find the most efficient connection between the UAV with the ground network, minimizing disruptions caused by terrain obstructions and varying signal conditions.

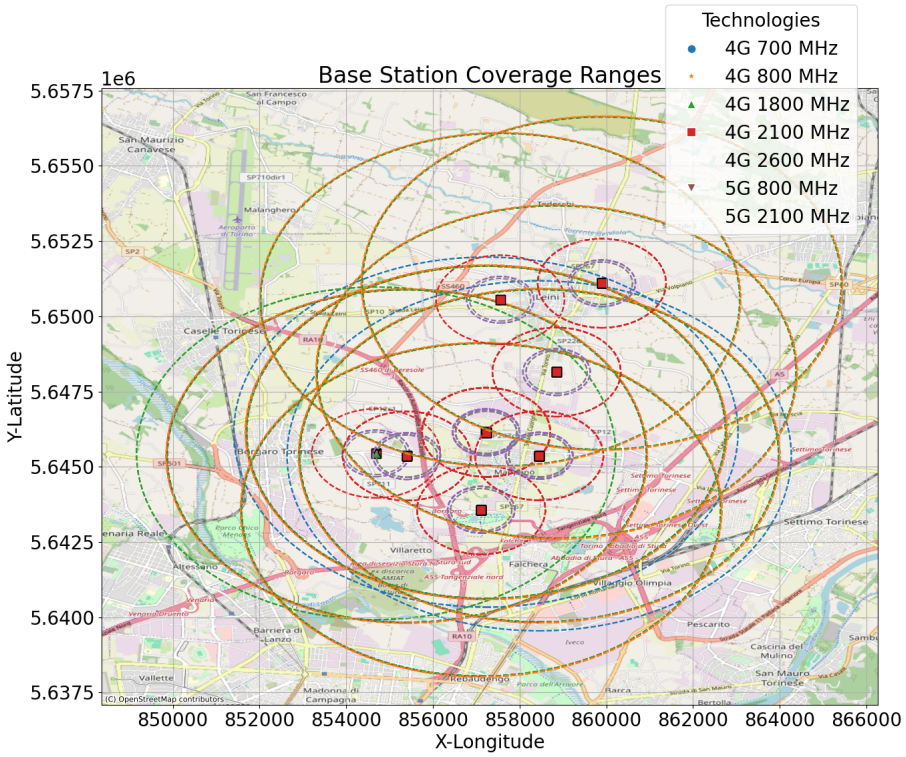

Figure 4.4: Estimated Range of coverages for each BS

4.2.1 Data Preprocessing and Input Handling

The algorithm begins with data preprocessing, ensuring that all necessary input files, including the Power consumption and supported technologies specifications, shapefiles, and base station information, are correctly loaded.

The UAV environment is built using real-world base station locations and topographical data extracted previously from the DEMs. The Radio Access Network (RAN) is composed of several BSs, each one individually characterized by its supported technology, either multi-frequency Long Term Evolution (LTE) or New Radio 5G.

Thanks to the data obtained from the [30] website and the work in [29], the algorithm can rely on various key technological parameters and characteristics of power consumption for each BS.

These input attributes include:

- **Geographic Coordinates:** Latitude and longitude defining its precise position.
- **Height and Antenna Specifications:** Actual BS height and supported technology bands (4G/5G).
- **Transmit Power:** Defines the signal strength for communication coverage.
- **Operational Layer:** Information on frequency bands and Absolute Radio Frequency Channel Numbers (ARFCNs).
- **Mobile Operator:** The specific cellular operator that installed his dedicated antenna. These are the main italian operators: Vodafone, Tim, Wind-Tre, Illiad and the newest Zefiro.

The simulator reads from configuration files that define the supported wireless communication technologies in the area. These files include parameters that dictate the performance and behavior of different cellular technologies, particularly 4G and 5G, across various frequency bands.

Below is presented the list of the main key parameters:

- **Bitrate:** The possible transmission rates (Mbps) available for that technology.
- **Input Power (dBm):** The value of the maximum input power of the antenna.
- **Frequency:** The specific frequency of the antenna, that can be for 4G technologies among 700, 800, 1800, 2100 or 2600 MHz, while for 5G technologies can assume one value among those available between 800, 2100 MHz.
- **Receiver SNR (dB):** Signal-to-noise ratio (SNR) values required to sustain different bitrates of the receiver.
- **SNR Threshold:** The minimum SNR required to maintain a stable connection, used to evaluate the range of coverage. A detailed explanation of this parameter choice will be done in the next subsection.

- **Bandwidth (MHz):** The allocated spectrum for that frequency.
- **Antenna Gain (dBi)**: The gain of the BS antenna.
- **Path Loss Margins**: Includes the *fade margin*, *interference margin*, and *shadow margin*, which account for real-world signal degradation and obstruction.
- **Maximum Input Power (dBm):** Defines the highest transmission power for that technology.
- **Doppler Margin**: Accounts for signal distortions due to UAV mobility.
- **Noise Figure**: Represents the noise introduced by the receiver hardware, affecting signal clarity.

In addition to technological parameters, the simulator also incorporates energy consumption models, which are defined in specific files. These models describe the power requirements for each type of base station and technology.

The power consumption model includes the following parameters:

- $N_{\mathbf{ant}}$: Number of antennas used in transmission.
- $P_{\mathbf{tx}}$: Power effectively transmitted by the base station.
- $P_{\mathbf{amp}}$: Power consumed by the amplifier to boost the signal strength, defined as:
$$P_{\text{amp}} = \frac{P_{\text{tx}}}{\eta} \tag{4.2}$$
where η is the efficiency factor.
- $P_{\mathbf{trans}}$: Power transferred for signal transmission.
- $P_{\mathbf{dsp}}$: Power dissipation in digital signal processing.
- $P_{\mathbf{rect}}$: Power used by the rectifier circuit to stabilize energy supply.
- $P_{\mathbf{cool}}$: Cooling system power requirements, particularly relevant for high-frequency 5G transmitters.
- $P_{\mathbf{bh}}$: Power used for backhaul connectivity to link the base station to the core network.
- $P_{\mathbf{mwl}}$: Power used by the microwave link for base station communication.
- η: Efficiency factor of the amplifier, indicating how much of the input power is converted into usable transmission power.
- *Sectors*: Number of independent antenna sectors supported by the base station.

These parameters allow the algorithm to compute realistic energy requirements for different base station configurations, impacting coverage calculations.
They are utilized in different computational models depending on whether the base station operates on a 4G or 5G network.

The simulator computes the total power consumption using different formulas:

- For **5G base stations**, power consumption is computed as:

$$P_{\text{total}} = N_{\text{ant}} \times (P_{\text{trans}} + P_{\text{dsp}} + P_{\text{amp}}) + P_{\text{rect}} + P_{\text{cool}} + P_{\text{bh}} \tag{4.3}$$

- For **4G base stations**, power consumption is computed as:

$$P_{\text{total}} = P_{\text{const}} + P_{\text{load}} \tag{4.4}$$

where

$$P_{\text{const}} = Sectors \times P_{\text{rect}} + P_{\text{mwl}} + P_{\text{cool}} + P_{\text{bh}} \tag{4.5}$$

and

$$P_{\text{load}} = Sectors \times (Tx \times (P_{\text{amp}} + P_{\text{trans}}) + P_{\text{dsp}})\,. \tag{4.6}$$

Concerning instead the UAV flight area, it is divided into a **3D grid**, where each cell represents a spatial point and contains metadata about potential obstacles, elevation, and later also with communication coverage. Spatial indexing techniques, such as R-trees, are applied to efficiently retrieve nearby BSs for each UAV position. The integration of geospatial analysis tools allows for enhanced optimization of communication paths, ensuring a good adaptability during UAV missions.

4.2.2 Base Station Coverage Computation

The coverage range of each base station is a fundamental aspect of this simulation. The computation is based on the **maximum allowable path loss** that still ensures an acceptable Signal-to-Noise Ratio (SNR). The maximum coverage distance is determined iteratively, increasing the distance from the base station until the path loss exceeds the defined limit, as shown in the flow chart 4.5.
Theoretical SNR thresholds can be derived from the Shannon-Hartley theorem, which defines the maximum channel capacity C (in bits per second) as:

$$C = B \log_2(1 + \text{SNR}) \tag{4.7}$$

where:

- C is the channel capacity,
- B is the channel bandwidth,
- SNR is the Signal-to-Noise Ratio.

.

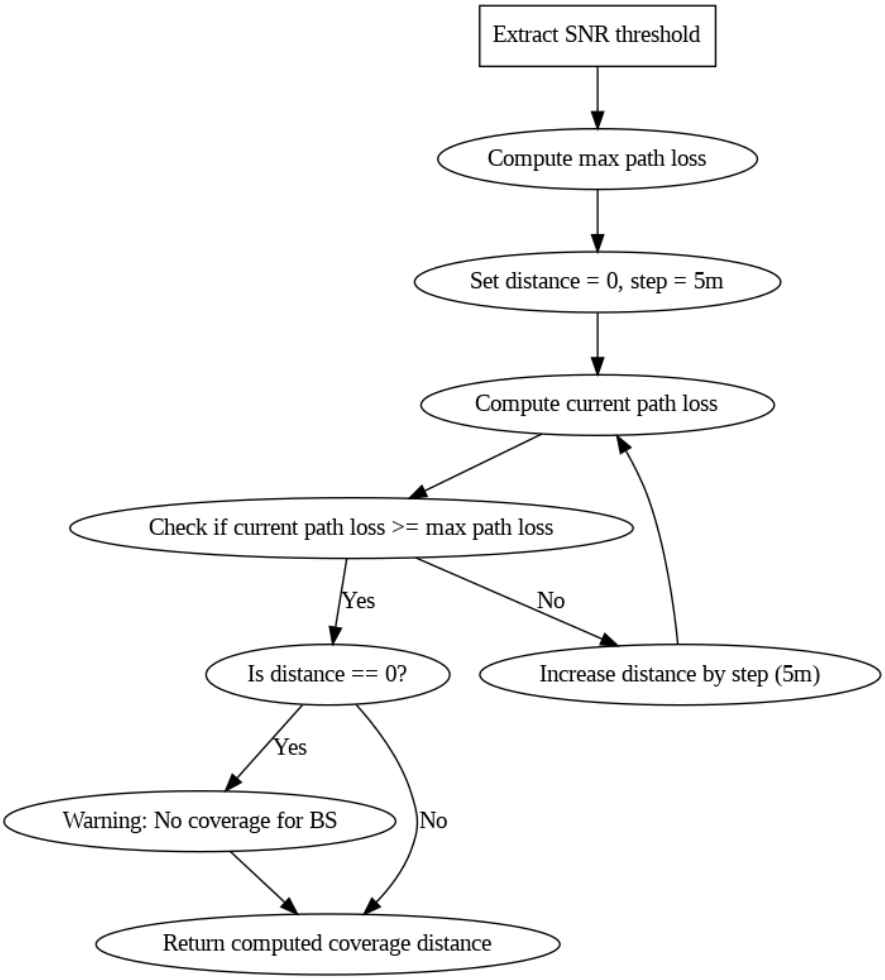

Figure 4.5: Flowchart describing the steps for Range of Coverage computation

From this equation, the minimum SNR required to sustain a given data rate can be derived as:

$$\text{SNR} = 2^{\frac{C}{B}} - 1. \tag{4.8}$$

However, the values obtained from this formula only represent theoretical limits under ideal conditions with no interference, no multipath fading, and perfect receiver sensitivity. In practical BVLoS scenarios, additional factors such as shadow fading, interference margins, and environmental conditions impact real-world communication quality, but we leave these aspects for future works.
To ensure a stable and reliable connection, the SNR thresholds used in this work are selected based on a balance between theoretical limits and real-world conditions, as derived from existing literature on network performance in RMA environments [32], [34] and [33]. Instead of setting SNR thresholds at their minimum viable levels, a more conservative approach is adopted to maintain a stable link, even in suboptimal conditions.

An ad hoc function to evaluate the range will iteratively increases the distance from the BS while computing the path loss, stopping once the maximum set SNR threshold is reached. The overall estimated range of coverage for each tower considered in the test area can be seen in figure 4.4. It should be specified that the calculated value does not guarantee the minimum beyond which there is no longer any coverage, but rather the coverage radius within which the signal quality is still considered to be at an 'acceptable' level (see table 4.6).

SINR

SINR	Signal strength	Description
>= 20 dB	Excellent	Strong signal with maximum data speeds
13 dB to 20 dB	Good	Strong signal with good data speeds
0 dB to 13 dB	Fair to poor	Reliable data speeds may be attained, but marginal data with drop-outs is possible. When this value gets close to 0, performance will drop drastically
<= 0 dB	Poor	Marginal data with drop-outs is possible, performance will drop drastically

Figure 4.6: General LTE SNR level bands, taken from [36]

Mathematically, the maximum path loss PL_{max} is derived as:

$$\mathrm{PL}_{\mathrm{max}} = P_{\mathrm{tx}} + G_{\mathrm{BS}} + G_{\mathrm{UAV}} - \mathrm{Losses} - \mathrm{SNR}_{\mathrm{min}} \tag{4.9}$$

where:

- P_{tx} is the transmit power of the BS,
- G_{BS} and G_{UAV} are the antenna gains of the BS and UAV, respectively,
- Losses accounts for penetration loss, Doppler margin, and other system-dependent attenuation factors,
- $\mathrm{SNR}_{\mathrm{min}}$ is the minimum required SNR for reliable communication, which is not the global minimum nor the theoretical one.

The choice of $\mathrm{SNR}_{\mathrm{min}}$ is based on empirical data from scientific literature rather than purely theoretical calculations. While the Shannon-Hartley theorem provides a theoretical lower bound for SNR, real-world conditions such as interference, multipath fading, and environmental attenuation necessitate a more conservative threshold.

The selected values are as follows:

- 4G at 2600 MHz: $\mathrm{SNR}_{\mathrm{min}} = 5$ dB,
- 4G at 2100 MHz: $\mathrm{SNR}_{\mathrm{min}} = 3$ dB,
- 4G at 1800 MHz: $\mathrm{SNR}_{\mathrm{min}} = 2$ dB,
- 4G at 800 MHz: $\mathrm{SNR}_{\mathrm{min}} = 0$ dB,

- 5G at 800 MHz: $\text{SNR}_{\text{min}} = 0$ dB.
- 5G at 2100 MHz: $\text{SNR}_{\text{min}} = 4$ dB.

These values reflect practical considerations, ensuring a balance between maintaining coverage and achieving an acceptable signal quality. BSs with different frequencies will have varying coverage ranges due to the inverse relationship between frequency and propagation distance, as shown in table 4.1. Lower frequencies, such as 700 MHz, will cover larger areas, whereas higher frequencies, such as 2600 MHz, will be more localized. This also imply that the SNR_{min} for lower frequencies can be set at lower values, viceversa for higher frequencies.

Technologies	Acceptable Ranges (m)
5G 2100 MHz	705
4G 2100 MHz	1480
4G 2600 MHz	770
5G 800 MHz	5540
4G 700 MHz	5815
4G 1800 MHz	5525
4G 800 MHz	5550

Table 4.1: Supported Technologies VS Range of Coverage

The importance of fine-tuning SNR thresholds is particularly evident in RMA environments, where coverage gaps are common, and small adjustments can significantly impact communication reliability. By adopting a moderate SNR threshold, this work aims to optimize coverage without excessively sacrificing quality, ensuring that UAV communication remains stable even in suboptimal scenarios.

4.2.3 Path Loss Computation: RMA Model and LoS/NLoS Conditions

After determining the BS coverage, the algorithm proceeds to compute the path loss at each UAV-accessible cell. The computation is based on the RMA model, an adaptation of the UMA model proposed in [29]. Reliable communication for UAVs operating in BVLoS scenarios depends critically on accurate channel modeling and path loss estimation. The RMA model is more suitable for suburban and rural areas due to the lower building density and larger inter-site distances.
In addition, in RMA environments, as mentioned previously, the BS density is typically lower and the propagation conditions are dominated by free-space losses with fewer scattering objects compared to urban settings.

Consequently, the path loss in RMA is primarily determined by:

- **Free-space propagation:** At moderate distances, the line-of-sight (LoS) component dominates, and the path loss can be almost approximated by a free-space model.

- **Dual-slope behavior:** A breakpoint distance (d_{BP}) is introduced to differentiate near-field and far-field propagation. The breakpoint is a function of the BS and UAV antenna heights.
- **Additional attenuation in NLoS conditions:** When obstacles (e.g., low-rise buildings, vegetation) obstruct the direct path, possible diffraction, scattering, and shadowing contribute to an additional loss.

The PL is expressed in decibels (dB) and is computed differently depending on whether the communication link is in **Line of Sight or Non-Line of Sight**. The RMA propagation model is employed to calculate path loss, considering whether the UAV has a clear LoS to the BS or encounters obstacles resulting in NLoS conditions.

For a given 2D distance d_{2D} between a base station and a receiver (e.g., drone), the LoS path loss that was adopted is given by:

$$\begin{aligned} PL_{\text{LoS}}(d_{3D}) = & 20\log_{10}\left(\frac{40\pi f_c}{3}\right) + \\ & \min\left(0.03h^{1.72}, 10\right)\log_{10}(d_{3D}) - \\ & \min\left(0.044h^{1.72}, 14.77\right) + 0.002\log_{10}(h)d_{3D}. \end{aligned} \tag{4.10}$$

where:

- d_{3D} is the 3D distance between the transmitter and receiver in meters, computed as:

$$d_{3D} = \sqrt{d_{2D}^2 + (h_{BS} - h_{UAV})^2} \tag{4.11}$$

Since we are working with distances of the order of kilometers, for those beyond the breakpoint distance ($d_{3D} > d_{BP}$), an additional loss term is introduced:

$$PL_{\text{LoS,far}}(d_{3D}) = PL_{\text{LoS}}(d_{3D}) + 40\log_{10}(d_{3D}/d_{BP}) \tag{4.12}$$

where:

- A breakpoint distance d_{BP} is introduced, computed as:

$$d_{BP} = \frac{4(h_{UAV} + 1)h_{BS}f_c}{c} \tag{4.13}$$

- $c = 3 \times 10^8$ m/s is the speed of light.

For NLoS conditions, if the UAV is obstructed by terrain, buildings, or foliage, additional **diffraction and scattering losses** are introduced:

$$\begin{aligned} PL_{\text{NLoS}}(d_{3D}) = & 161.04 - 7.1\log_{10}(W) + 7.5\log_{10}(h) + \\ & -(24.37 - 3.7(h/h_{BS})^2)\log_{10}(h_{BS}) + \\ & +(43.42 - 3.1\log_{10}(h_{BS}))(\log_{10}(d_{3D}) - 3) + \\ & +20\log_{10}(f_c) - (3.2(\log_{10}(11.75h_{UAV}))^2 - 4.97) \end{aligned} \tag{4.14}$$

where:

- The term $PL_{\text{LoS}}(d_{3D})$ is compared to $PL_{\text{NLoS}}(d_{3D})$, and the larger value is taken as the final path loss.

If the computed NLoS path loss exceeds the LoS path loss, the LoS model is applied as a conservative estimate.

$$PL'_{\text{NLoS}} = \max(PL_{\text{LoS}}, PL_{\text{NLoS}}) \tag{4.15}$$

From the extracted information, the following variables and parameters are considered:

- **Carrier Frequency (f_c)**: The frequency of the transmitted signal in GHz, influencing propagation characteristics.
- **2D Distance (d_{2D})**: The horizontal distance between the transmitter and receiver in meters.
- **3D Distance (d_{3D})**: The actual Euclidean distance considering height differences, computed as $\sqrt{d_{2D}^2 + (h_{BS} - h_{UAV})^2}$.
- **Base Station Height (h_{BS})**: The height of the base station antenna, which affects signal propagation and diffraction.
- **UAV Height (h_{UAV})**: The height of the UAV in meters.
- **Breakpoint Distance (d_{BP})**: The distance beyond which additional losses occur, computed based on frequency and heights.
- **Street Width (W)**: A factor influencing NLoS path loss in urban and suburban environments.
- **Building Height (h)**: Used in computing diffraction and scattering effects in NLoS conditions.

Additional terms are present in the LoS and NLoS equations have been derived from the literature [23], and ensure accurate modeling of path loss in both LoS and NLoS conditions:

- $20\log_{10}(40\pi(f/3\times10^8))$: Free-space path loss component.
- $\min(0.03h^{1.72}, 10)\log_{10}(d_3)$: Accounts for attenuation due to building height.
- $\min(0.044h^{1.72}, 14.77)$: Additional attenuation factor related to building height, capped at 14.77.
- $0.02\log_{10}(h)\cdot d_3$: Small correction factor for building height.
- $40\log_{10}(d_3/d_{BP})$: Models increased path loss beyond the breakpoint distance.
- $-7.1\log_{10}(W)$: Effect of street width on signal attenuation.

- $7.5 \log_{10}(h)$: Accounts for the average building height's effect on signal attenuation.
- $(43.42 - 3.1 \log_{10}(h_{BS}))(\log_{10}(d_3) - 3)$: Models impact of distance and base station height.
- $20 \log_{10}(f)$: Incorporates effect of carrier frequency.
- $-(3.2(\log_{10}(11.75h_u))^2 - 4.97)$: Models effect of mobile station antenna height.
- $(24.37 - 3.7(h_{average}/h_{BS})^2) \log_{10}(h_{BS})$ (for NLoS only): Captures BS height impact, important for NLoS scenarios.

This refined model ensures an accurate computation of the quality of communication for different environments, considering the presence or absence of obstacles between the base station and the receiver.

4.2.4 Iterative Path Loss Assignment and Sorting

In summary, to evaluate the connectivity of UAV-accessible cells in the environment, the algorithm iteratively computes the path loss from nearby base stations for each cell. The stored PL values for each cell are no more than 30, meaning that not for each BS present in the area the result is stored. This decision was taken both for computational and time-saving reasons, but also because the results were getting worse, and consequently they would not have been taken into account in the selection for the shortest path afterwards.

This procedure is essential to determine the best possible coverage for each cell and forms the foundation for subsequent weights assignment to each graph's edge.

The process is described in the following:

1. Select a cell n with obstacle field = 0.
2. For each BS, check if n falls within its coverage range.
3. If covered, determine if the BS is in LoS or NLoS relative to n.
4. Compute the corresponding path loss using the RMA model.
5. If the computed path loss is below the acceptable maximum, store it and set the *no_ cover* flag to 0.
6. If multiple BSs cover n, store path loss values in a sorted list (ascending order).
7. If no BS covers n, leave *no_ cover* set to 1.

The outcome of this phase is a comprehensive mapping of UAV-accessible cells to their respective BSs, ordered by signal quality. This information will be crucial for the second phase, where edge weights between nodes are determined based on signal strength, handover events, and network stability.

4.3 Graph Weight Assignment

This section details the methodology employed for assigning weights to the omni-directional edges in the newly constructed graph, as depicted in the flowchart in Figure 4.3. The resulting graph, enriched with appropriate weight assignments, serves as the foundation for computing the shortest path in the simulator, whose details will be further elaborated in the following sections.

The algorithm commences by iterating over all cells in the discretized environment and selecting only those for which the obstacle attribute is set to zero. This ensures that weight computations are performed exclusively on traversable regions, effectively filtering out obstacles from the connectivity analysis.
Once a cell, denoted as n, has been selected, its adjacent nodes are identified. Given the imposed constraint that limits the maximum number of adjacent cells to $n' \leq 18$, the algorithm examines only these neighboring nodes. The selection criterion for adjacency is based on direct spatial connectivity within the 3D grid structure, as mentioned in chapter 3.

For each selected cell n, the algorithm determines whether it shares a base station with its adjacent nodes. This step is essential, as connectivity properties depend on the communication infrastructure available to each cell.

The evaluation follows these steps:

1. Retrieve the set of base stations covering cell n as well as its adjacent node n'.

2. Extract the PL values corresponding to the communication link between n and each of its associated base stations.

3. Compare the base stations assigned to n and n' to determine if they share the same primary (best) base station.

Once the path loss values are extracted, the relative loss between nodes is assessed using the ratio:

$$\frac{PL_{n'}}{PL_n} \tag{4.16}$$

where PL_n and $PL_{n'}$ represent the path loss values for the current and adjacent cell, respectively.

At this stage, two possible cases emerge:

- **Cases 1:** The best base station for cell n, i.e., the one providing the lowest path loss, is also the best base station for its adjacent node n'.

- **Cases 2:** The best base station for cell n is either absent in the base station list of n' or is present but does not provide the best possible coverage for that position.

4.3.1 Assignment of Edge weight - Case 1

In the case where both the current node N and its neighboring node N' are primarily covered by the same base station, the algorithm proceeds by computing the ratio of their respective path loss values, as done in equation 4.16.
This ratio quantifies the relative degradation of the signal between the two nodes. Since path loss inherently measures the attenuation experienced by the transmitted signal, higher ratios indicate a more significant loss when transitioning from n to n'.

To ensure consistency across different edge weights and maintain comparability in the shortest-path computation, the computed ratio undergoes a scaling and normalization process. The algorithm first applies a logarithmic transformation:

$$W_{\log} = \log(W_{n,n'}) + 5 \tag{4.17}$$

where the base offset of 5 ensures that all weights remain positive, avoiding negative values that could distort the weight distribution and can later cause possible errors in the NetworkX algorithm.

Next, the transformed weight is rescaled to fit within a predefined range:

$$W'_{n,n'} = W_{\min} + \frac{(W_{\log} - 1)}{10 - 1} \times (W_{\max} - W_{\min}) \tag{4.18}$$

where $W_{\min}$ and $W_{\max}$ represent the minimum and maximum observed weight values across the entire graph. The rescaled values are mapped onto the interval $[1, 10]$ to ensure consistent weight interpretation.

4.3.2 Assignment of Edge Weights - Handover Case

If the adjacent node n' is covered by a different base station than n, an additional penalty is introduced to account for the handover cost. This reflects the preference for maintaining connectivity with a single base station throughout the UAV's flight, as frequent handovers may introduce latency, increased energy consumption, and more importantly potential communication disruptions.

The penalty is computed as a function of the relative path loss values of the two nodes:

$$P_{\text{handover}} = 2 \times \left| 1 - \frac{PL_{n'}}{PL_n} \right| \tag{4.19}$$

This formulation ensures that the penalty increases as the path loss discrepancy

between n and n' grows. Larger penalties discourage frequent handovers by increasing the associated transition cost.

The introduction of a handover penalty serves two key purposes:

- **Minimizing unnecessary transitions**: By increasing the weight of edges that involve handovers, the algorithm will favor paths that maintain connectivity with a single base station for as long as possible.
- **Reflecting real-world constraints**: In practical UAV communications, excessive handovers may result in increased packet loss, delays, and energy consumption, making it desirable to limit such occurrences.

4.3.3 Assignment of weights to special cases

An additional case arises when a selected cell n has no obstacles ($obstacle = 0$) but is entirely outside the coverage range of any base station, indicated by the flag $no\_cover = 1$. In this scenario, the cell represents a geographical location where no wireless connectivity is available.

Consequently, while an entry edge can still exist, its weight is set to infinity:

$$W_{n,n'} = \infty \tag{4.20}$$

This effectively discourages the selection of paths traversing such cells, as the UAV would experience a complete loss of connectivity.

Before finalizing the graph and storing it in GraphML format, a final consistency check is performed to ensure that at least one upward-directed edge exists from ground-level cells ($z = 0$).
This is important as it guarantees that the UAV, regardless of its initial position on the ground, has a valid path to ascend into the air. It is assumed that takeoff in obstacle-fill areas can be aided by a pilot, making an initial transition from the ground to a higher altitude always feasible. This occurrence is only valid if z is equal to 0, i.e. the drone takes off from the ground.

The logic for assigning these edges is as follows:

- If an edge from node B to node A exists, where $z_A = 0$, then an edge in the opposite direction from A to B is created, inheriting the same weight.
- If no such reverse edge exists, a default weight of infinity is assigned, following the same policy done in equation 4.20.

With this final processing step, the graph is now fully prepared, incorporating all necessary weight adjustments, penalties, and connectivity constraints.

4.3.4 Interpretation of Edge Weights

The final weight assigned to the edge connecting n and n' is a measure of the expected difficulty in establishing a reliable communication link between the two cells. Lower values indicate better connectivity, whereas higher values reflect a higher likelihood of signal degradation. That is why, to adapt them to the NetworkX edge weight rules, the reciprocal is computed with the exception of the special cases where W_{final} is already set to the worst possible value, equal to ∞.

Thus the final weight assigned to the edge connecting n and n' is computed as:

$$W_{\text{final}} = \frac{1}{\max(W'_{n,n'}, 1)} \tag{4.21}$$

Whereas the rescaled weight, incorporating the handover penalty, is computed as:

$$W'_{\text{handover}} = W'_{n,n'} - P_{\text{handover}} \tag{4.22}$$

The modified graph, now enriched with weight penalties, is subsequently stored in GraphML format, preserving all relevant node and edge attributes for subsequent shortest-path computations.

4.4 Shortest Path Computation and Scenario Testing

After constructing the weighted graph representations of the environment, the next step involves computing the shortest path for a UAV trajectory using the *NetworkX* library [44]. This section outlines the methodology adopted for path computation, detailing the algorithms, tools, and testing scenarios employed to evaluate UAV navigation through the generated graphs.

The primary objective of this phase is to determine the most efficient UAV trajectory while maintaining a stable communication link with the available BSs. The computed paths take into account the weighted graph structures described in the previous sections, where edge weights encapsulate the expected difficulty in maintaining reliable connectivity due to PL and potential handovers.
To achieve this, the *Dijkstra's algorithm* is leveraged from the *NetworkX* library [46], ensuring the computation of the minimum-cost path from a given start node to a target destination. As defined by [45] source:

> *Dijkstra's algorithm is an algorithm for finding the shortest paths between nodes in a weighted graph, which may represent, for example, a road network.*

Dijkstra's algorithm operates with a time complexity of $O(|E|+|V|\log|V|)$, where $|V|$ is the number of nodes and $|E|$ is the number of edges in the graph (source [45]). This complexity arises from the use of a priority queue (commonly implemented as a binary heap), allowing efficient retrieval of the next node with the smallest

accumulated cost. Given that UAV trajectory planning involves a limited number of waypoints and the network of base stations is not overly dense, this computational complexity remains manageable.
The cost function is dictated in this work by the assigned edge weights, which, as described earlier, reflect communication quality rather than simple Euclidean distances.

This algorithm finds the shortest path from a source node to a destination node in a weighted graph by iteratively expanding the least-cost path until reaching the target. At each step, the algorithm selects the node with the lowest cumulative weight, updates its neighboring nodes' tentative distances, and continues until the optimal path is found.

The step-by-step operation of Dijkstra's algorithm is illustrated in Figure 4.7.

4.4.1 Graph Variants and Test Scenarios

Different scenarios and tests are performed to compare the performance and results obtained under different circumstances.
To analyze different UAV mobility conditions and communication constraints, three distinct graph structures are considered:

- **Graph with 3 altitude layers**: This graph represents a moderately discretized environment where UAV movement is restricted to three different altitude levels (30 m, 60 m, and 90 m). It serves as the baseline scenario, offering a balance between computational efficiency and flexibility in trajectory planning.
- **Graph with 4 altitude layers**: An extension of the previous graph, incorporating an additional altitude layer at 10m, allowing an evaluation of UAV behavior at lower altitudes, particularly in urban-like areas where obstacles may influence the choice of the optimal path, and Non-Line of Sight situations may arise more frequently.
- **Graph with 9 altitude layers**: This is the most discretized representation, allowing UAVs to navigate at fine-grained altitude variations (10m intervals up to 90m). It is particularly useful for testing UAV decision-making in densely populated areas, where multiple flight levels provide different trade-offs in connectivity and obstacle avoidance.

For each of these graph structures, multiple test scenarios are implemented by varying:

- The initial and target positions of the UAV.
- The UAV model used, with distinct technical features.

- The impact of base station distribution and coverage variations.
- The influence of handover penalties on the computed paths.

Different Edge Weights

Besides exclusively using the *Path Loss weights*, two additional types of weights are computed and employed to determine alternative shortest paths:

- **Physical Distance Weights:** Each edge weight is assigned based on the Euclidean distance between two connected nodes, representing a purely geometric shortest path. Given two nodes u and v in the graph, the distance weight is simply computed as:

$$d_{uv} = \sqrt{(x_u - x_v)^2 + (y_u - y_v)^2 + (z_u - z_v)^2} \tag{4.23}$$

  where (x_u, y_u, z_u) and (x_v, y_v, z_v) are the coordinates of nodes u and v, respectively.

- **Combined Weights:** A weighted combination of the physical distance and path loss values, balancing both spatial efficiency and communication reliability. The combined weight is computed as:

$$w_{uv}^{\text{combined}} = W_{PD} \cdot d_{uv} + W_{PL} \cdot w_{uv}^{\text{PL}} \tag{4.24}$$

  where d_{uv} is the physical distance weight, and w_{uv}^{PL} represents the path loss weight assigned to the edge (u, v). The values W_{PL} and W_{PD} are the factors given to each kind of 'weight' in order to give more importance to one or the other. The tests are done by varying these factors in order to find the best balance between the physical shortest path but without reducing the quality of communication. Among the results, the combination used are listed in table 4.2.

Path Distance (PD)	Path Loss (PL)
50	50
80	20
20	80

Table 4.2: Combined weights proportions

All three weight configurations are applied across the three graph variants in order to evaluate how different cost functions influence UAV trajectory selection.

Base Station Reduction Analysis

In addition to the scenarios illustrated in Figure 4.8, additional tests are conducted by reducing the number of available base stations in the network. Specifically, the

base stations supporting the technologies *4G 700 MHz, 4G 800 MHz*, and, in the case of the 4-layer graph, also *5G 800 MHz* are removed.
This reduction aims to evaluate the impact of decreased connectivity on UAV navigation and path selection.
Unlike the main tests, which involved multiple UAV models, these reduced-base-station scenarios are tested exclusively using the *DJI Inspire 3*, since changing the drone will impact only the power consumption and battery level performance in this case.

Scenarios Summary

The following sections will present a detailed analysis of the shortest paths computed under the conditions described above, comparing UAV trajectories, communication performance, and overall network robustness across different scenarios.
The relationships among these test scenarios are summarized in Figure 4.8.

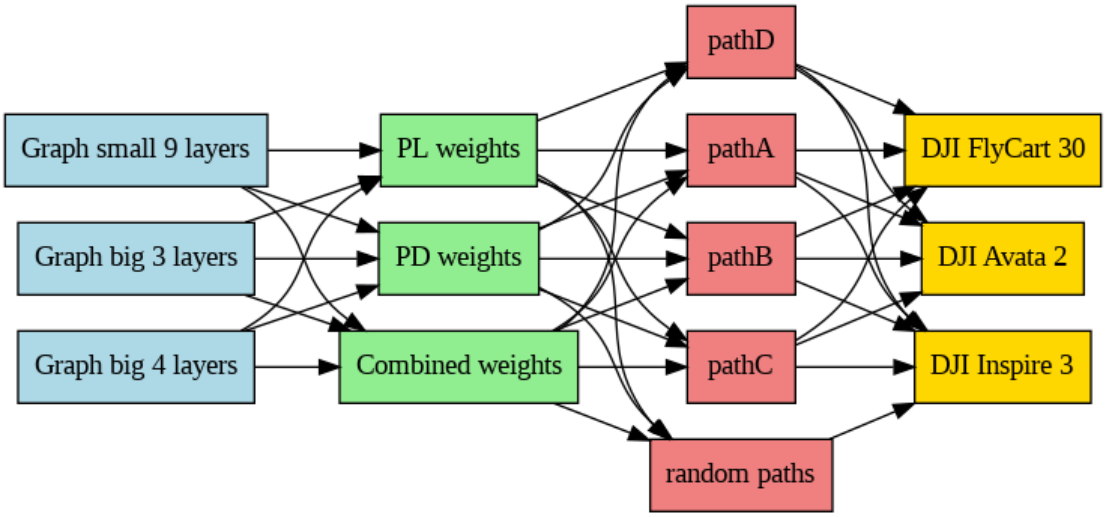

Figure 4.8: Overview of the main scenarios tested in shortest path computations

Each simulation considers multiple weight configurations (path loss, distance, and their combination), various UAV models, and different start-end path pairs across the three graph variants. The results highlight the trade-offs between minimizing path loss and optimizing trajectory efficiency.

4.4.2 Key Performance Indicators (KPIs)

A crucial step in every simulation-based study is the definition of Key Performance Indicators (KPIs). In this analysis, the selected KPIs follow widely accepted criteria ensuring specificity, measurability, and relevance to the study objectives.
For this study, three primary KPIs are chosen to evaluate UAV path computa-

tion strategies, focusing on network connectivity, flight efficiency, and signal quality.

The defined Key Performance Indicators are as follows:

1. **Communication Performance**
    - Evaluates the UAV's connectivity with the ground network by analyzing parameters such as:
        - Mean and variance of the path loss encountered during the trajectory.
        - The percentage of LoS and NLoS connections along the path.
        - Number of handovers suffered along the path.
2. **Travel Distance and Flight Characteristics**
    - Measures the total distance traveled by the UAV along the computed shortest path.
    - Includes sub-metrics such as the number of altitude changes (ups and downs) and time elapsed from take-off and landing.
    - Battery level and power consumptions of the drone with or without payload.
3. **Network Technology Utilization**
    - Assesses which communication technologies are predominantly used throughout the UAV's flight.
    - Computes the percentage of connectivity with different technologies.
    - Provides insights into how the UAV interacts with different network infrastructures and helps in optimizing coverage strategies.

Among these, the main ones include total path length, average path loss, the cumulative vertical displacement (z-axis shifts) and the total number of handovers suffered during flight, the results of which will be shown in the next chapter.

The main focus, as mentioned in the first chapters, will be on Communication Performances. These should be evaluated by balancing the average PL with the total number of handovers H_n and the percentage of LoS (or NLoS) sustained along the path. For instance, good communication performance would be reached by minimizing the H_n, the average PL as well as the percentage of NLoS.
In the following chapter, the outputs and results obtained for each scenario and combination of weights/graphs/UAV type, starting from the baseline, will be presented.

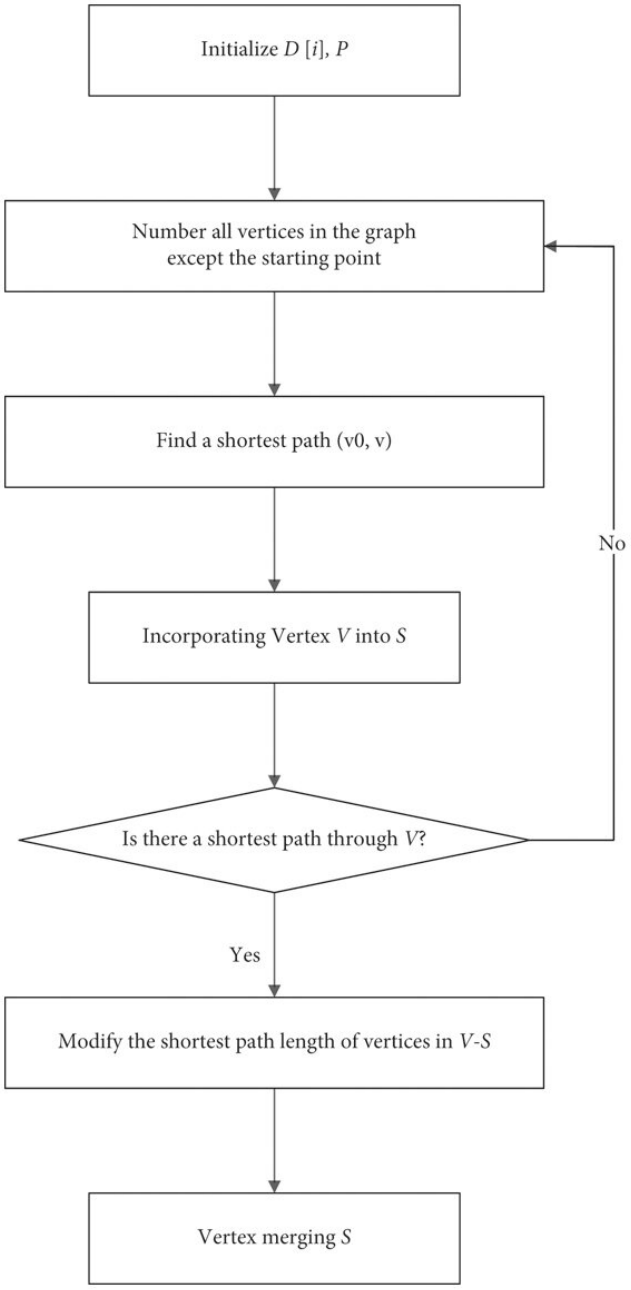

Figure 4.7: Dijkstra algorithm flow chart, taken from [35]

Chapter 5

Final Results

This chapter presents the results obtained from the UAV shortest path simulations, analyzing different network and mobility conditions across multiple scenarios. The final goal is to evaluate the impact of various weighting strategies (path loss, physical distance, and combined weights) on UAV trajectory optimization while considering key performance metrics such as connectivity, handover frequency, and power consumption.

The results are structured according to the three different graph configurations (3 layers, 4 layers, and 9 layers), considering the path evaluated with the PL weights (the standard weight scenario). For each graph, simulations are conducted using different UAV models and weight-assignment strategies, providing insight into how different constraints affect flight efficiency and network stability.
Additionally, a sensitivity analysis is performed to assess the impact of reducing the number of available base stations, specifically by removing support for lower-frequency bands such as 4G 700 MHz and 4G 800 MHz.
These tests will be presented in the final sections of this chapter.

5.1 Drone Specifications

Maintaining good and stable drone-to-tower communications is indeed the focus of this work, but in order to have a realistic assessment of the final outcomes, other performance metrics such as power consumption, time elapsed, and battery level are also considered.

Three different drones with very different technical features, as reported in the table 3.1, are used to monitor and compare these metrics.
The computations are based on aerodynamic models, energy efficiency principles, and real drone specifications taken from the official *DJI website* [38], leveraging methodologies from the works in [39] and [40].

It should be specified that both horizontal and vertical speeds are considered at their maximum values in *Normal* flight mode. Since operating at these speeds results in

higher energy consumption compared to typical flight velocities, this choice was made to evaluate a worst-case scenario. Additionally, as no weather conditions are factored into the analysis, this assumption helps balance the simplification introduced by neglecting external environmental factors.
Regarding the UAV's empty weight, it already includes the battery but does not account for any additional payload. The payload weight is set to the maximum capacity that each drone is capable of carrying. Consequently, the results obtained for the *DJI Avata* remain unchanged between the payload and no-payload scenarios, as this drone is not designed to carry additional weight beyond its built-in battery and camera equipment.

Specification	**FlyCart 30**	**Avata 2**	**Inspire 3**
Empty Weight (kg)	52.5	0.377	3.995
Max Payload (kg)	30.0	0.0	0.4
Battery Capacity (mAh)	38000	2150	4280
Battery Voltage (V)	52.2	14.76	23.1
Horizontal Speed (m/s)	20.0	8.0	26.0
Vertical Speed (m/s)	3.0	6.0	8.0
Air Density (kg/m^3)	1.204	1.204	1.204
Drag Coefficient	0.3	0.3	0.3
Frontal Area (m^2)	0.5	0.013	0.124
Width (m)	3.08	0.212	0.7098
Length (m)	2.8	0.185	0.500
Height (m)	0.947	0.064	0.176
Rotors (num)	8	4	4
Rotors diameter (m)	1.375	0.0756	0.406

Table 5.1: Drone Specifications Used in Simulations

The power consumption of the drone is computed by distinguishing horizontal and vertical energy expenditures. Horizontal power consumption accounts for aerodynamic drag, while vertical power is dictated by the energy required to counteract gravity. The aerodynamic drag force is computed as:

$$F_{drag} = \frac{1}{2}\rho V_{air}^2 C_d A, \tag{5.1}$$

where C_d is the drag coefficient, A is the drone's frontal area, and V_{air} is the relative airspeed, which includes wind effects.
Since air density affects aerodynamic performance, it is modeled using the International Standard Atmosphere (ISA) approximation:

$$\rho(h) = \rho_0 \left(1 - \frac{Lh}{T_0}\right)^{\frac{g}{RL}-1}, \tag{5.2}$$

where ρ_0 is the sea-level air density (1.204 kg/m^3), L is the temperature lapse rate (0.0065 K/m), T_0 is the reference temperature at sea level (293.15 K), g is gravitational acceleration (9.81 m/s^2), and R is the specific gas constant for air

(287.05 J/(kg·K)). This formula accounts for the decrease in air density as altitude increases, influencing energy requirements.
Wind speed is also considered, as it influences the drone's effective airspeed and subsequently impacts energy consumption. It is estimated using a power-law model:

$$W(h) = W_0 \left(\frac{h}{h_0} \right)^{\alpha}, \tag{5.3}$$

where W_0 is the reference wind speed at $h_0 = 10$ m (set to 1 m/s), and $\alpha = 0.1$ for low turbulence conditions. While the influence of wind is considered to be relatively small in these experiments, its impact on power consumption is still integrated into the computations.

The thrust required to keep the drone airborne is determined following the model used in [39]:

$$T = (m_{drone} + m_{payload})g + F_{drag}, \tag{5.4}$$

where m_{drone} and $m_{payload}$ are the mass of the drone and its carried payload, respectively. The hovering power required to maintain altitude is then computed as:

$$P_{hover} = \frac{T^{3/2}}{\sqrt{0.5\pi n d^2 \rho}}, \tag{5.5}$$

where n is the number of rotors and d is the rotor diameter. The power needed for forward motion is given by:

$$P_{forward} = TV_{air}. \tag{5.6}$$

The total power consumption at any point in the flight is then computed as:

$$P_{total} = P_{hover} + P_{forward}. \tag{5.7}$$

The total energy consumption, in kWh, is obtained instead by integrating power over time:

$$E = \frac{P_{total} \cdot t}{3600}, \tag{5.8}$$

where t is flight time in seconds, converted to hours for watt-hour calculations. Takeoff and landing introduce additional power requirements, modeled as:

$$P_{takeoff} = \frac{(m_{drone}g)^{3/2}}{\sqrt{2\rho A}}. \tag{5.9}$$

A duration of 5 seconds is assumed for takeoff and landing, adding extra energy consumption.
Finally, the battery level at each step is computed as:

$$B_{remaining} = 100 - \frac{E_{total}}{C_b V_b} \times 100, \tag{5.10}$$

where C_b is battery capacity in mAh and V_b is battery voltage in volts, converted from mWh to Wh. These calculations allowed for precise tracking of energy consumption and remaining flight time, incorporating altitude, wind effects, and

payload variations.

The different capabilities of these UAVs lead to variations in optimal path selection, as flight speed, weight, and aerodynamics affect energy consumption and maneuverability.

5.2 Performance Analysis of default scenario - 3-layered graph

In the context of the default case, the 3-layer graph is used to model the environment. Figure 5.1 illustrates the four shortest paths calculated by the NetworkX algorithm for the given start and end points. The selected paths displayed on the right are based on path loss weights, which evaluate the impact of signal attenuation along the trajectory. On the left are instead presented the same paths, with the only difference of using the physical distances as the edges weights.

The following elements are highlighted in figures 5.1, 5.2, 5.3 and 5.4, and will be valid for this and subsequent 2D plots:

- The **red line** represents the chosen shortest path as determined by the algorithm. Note that while the path appears as a 2D projection, it includes transitions between different elevation levels (z-layers), which are not directly visible in these plots.
- The **green dot** indicates the starting point of the trajectory, while the **blue dot** represents the endpoint.
- The **orange dots** correspond to the geographical locations of the base stations (BSs), which are distributed across the environment.

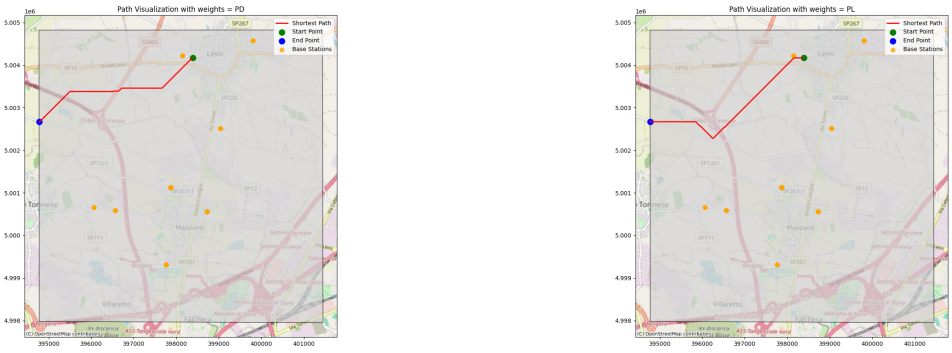

(a) Path A with PD weights selection (b) Path A with PL weights selection

Figure 5.1: Path A for the 3-layered graph - PD & PL weights comparison.

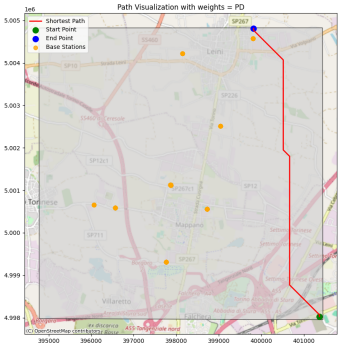

(a) Path B with PD weights selection

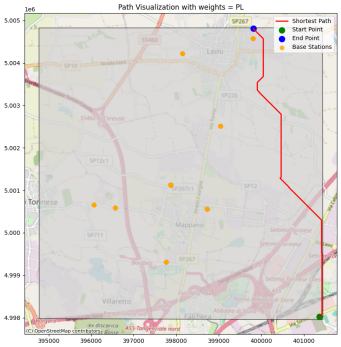

(b) Path B with PL weights selection

Figure 5.2: Path B for the 3-layered graph - PD & PL weights comparison.

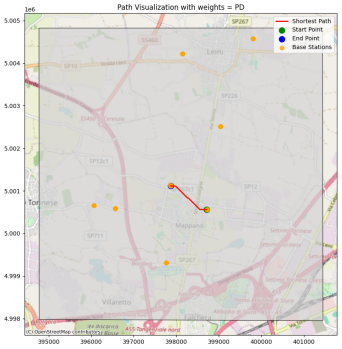

(a) Path C with PD weights selection

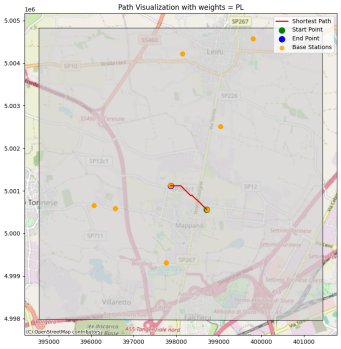

(b) Path C with PL weights selection

Figure 5.3: Path C for the 3-layered graph - PD & PL weights comparison.

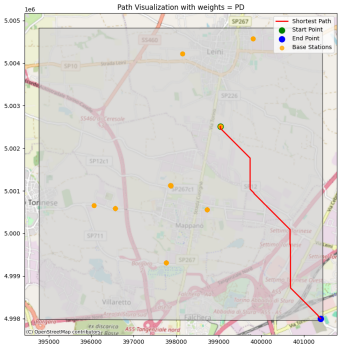

(a) Path D with PD weights selection

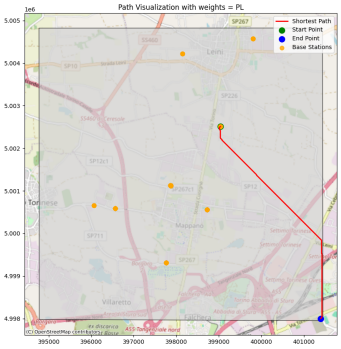

(b) Path D with PL weights selection

Figure 5.4: Path D for the 3-layered graph - PD & PL weights comparison.

The results reveal varying path lengths and characteristics depending on the proximity of the UAV to base stations and urban centers, as well as the relative elevations at the starting and ending points. In particular:

- In Figures 5.1a 5.1b, the paths start from a relatively remote area, far from any BSs, approaching an urban area once at destination, with moderate proximity to base stations.
- In Figures 5.2a and 5.2b, the trajectories cover longer distances, being further away from the base stations in the first half of the trajectory, emphasizing the impact of higher path loss weights.
- In Figures 5.3a and 5.3b, the selected paths starts and ends near base stations, traversing areas with relatively high urban density.
- In Figures 5.4a and 5.4b, the selected paths endpoints are rather far away from any urban center, starting also far away from any BSs but arriving exactly adjacent to one.

Even without a 3D visualization, it is clear how, especially for longer distances, the PL weight-based paths are not optimize to find the shortest path, sometimes seemingly preferring deviations from the physical shortest one. In any case, even if not very noticeable, these small deviations tend to force the path to the nearest BS location in the territory.

To illustrate the differences between the two path selection strategies, Figure 5.5 presents a comparison between the distances traveled when optimizing for PL versus PD. The plot visualizes the relationship between the two approaches for different paths, highlighting the percentage increase in total distance when prioritizing communication performance over travel efficiency. Points above the diagonal line indicate cases where the PL-based approach resulted in longer trajectories compared to the PD-based method. The percentage labels quantify this increase, showing the extent to which the PL distance exceeds the PD distance. On average, for middle-range distances between 3 and 5 km, the increase is approximately 4.8%. For shorter distances between 500 m and 3 km, the average increase rises to 7.6%. Finally, for longer distances exceeding 5 km, the increase averages around 3.25%.

To better understand this statement, in figures 5.6 and 5.7 are represented the 3D plots of the trajectories for the first 2 paths A and B. On the left side of figures 5.6 and 5.7 (a and c) the 3D path representations compare the differences with respect to the two paths computed using PD over PL. Clearly, the fact that by only focusing on optimizing the path losses over the physical distances may force the drone to do many shifts, especially along z.

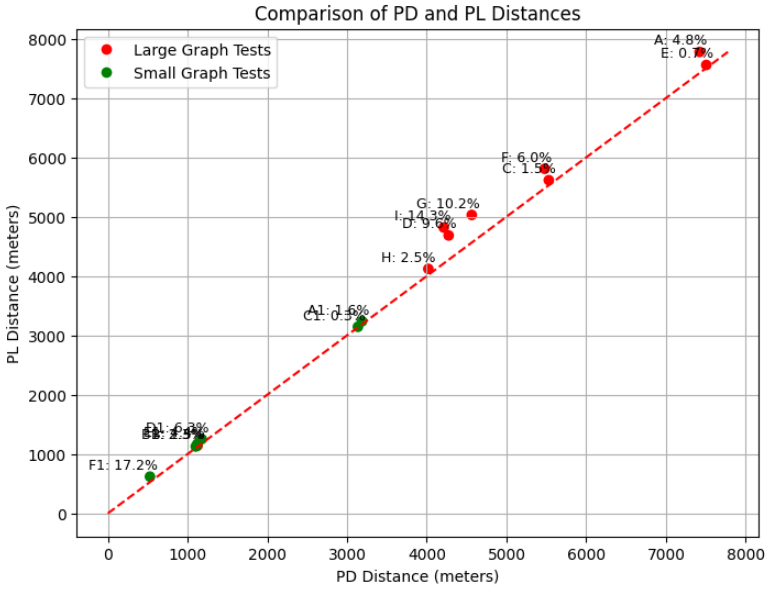

Figure 5.5: Extra Distance comparison between PD and PL cases

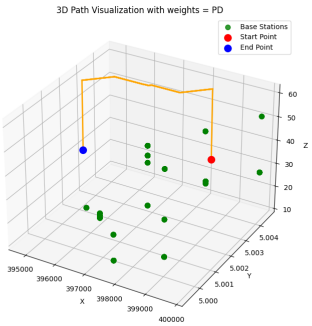

(a) Path A - 3D plot using PD

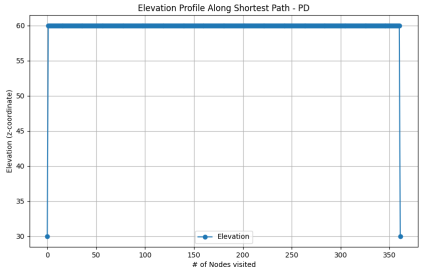

(b) Path A - elevation profile using PD

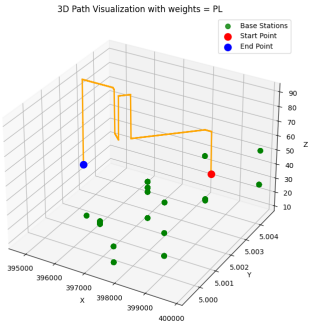

(c) Path A - 3D plot using PL

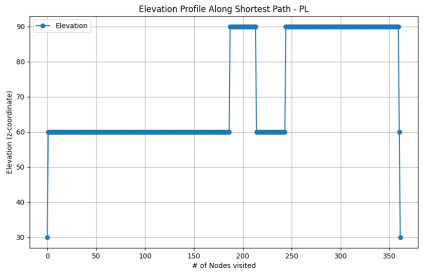

(d) Path A - elevation profile using PL

Figure 5.6: Path A - focus on displacements along the z-axis

However, to better quantify the differences between the two path selection strategies,

the PL weight-based results are indeed optimized for communication performances, as shown in tables 5.2 and 5.3. The table structure presents in the first column the metrics, in the second column the results obtained using the path loss ratios as weights, and finally in the third column the standard (abbreviated STD) path, minimizing distance.
These tables summarize key metrics for each computed trajectory. The total path length gives insight into how much extra distance is traveled when optimizing for PL instead of PD. The cumulative vertical displacement highlights how much the drone is forced to change altitude when selecting the path with the lowest signal attenuation.

The data reveals that paths optimized for PL tend to exhibit significantly higher cumulative vertical displacement compared to those optimized for PD. This suggests that minimizing signal attenuation forces the UAV to navigate through different altitude layers more frequently, likely in an effort to maintain a favorable line of sight with base stations. While this may enhance communication reliability, it could also lead to increased energy consumption due to frequent altitude adjustments. This is especially highlighted by the "Final Battery Level" metric reported in tables 5.2 and 5.3.

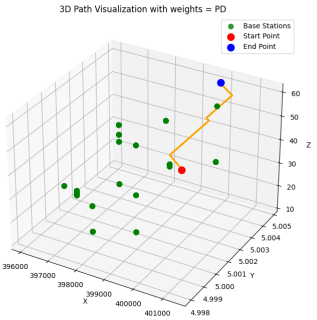

(a) Path B - 3D plot using PD

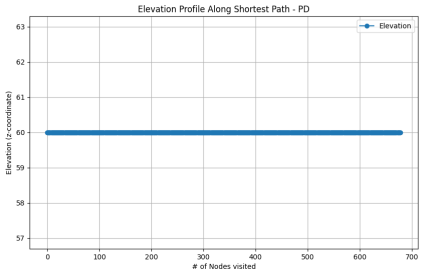

(b) Path B - elevation profile using PD

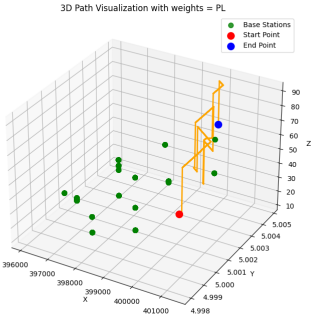

(c) Path B - 3D plot using PL

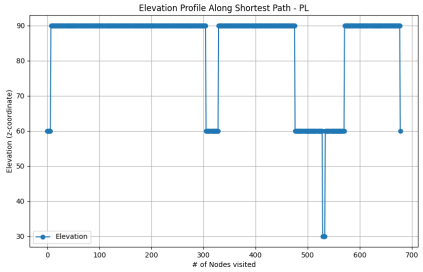

(d) Path B - elevation profile using PL

Figure 5.7: Path B - focus on displacements along the z-axis

Table 5.2: Comparison of Path Loss Optimized vs. PD path using DJI FlyCart 30 for Path A

Metric	**PL Optimized**	**STD Shortest Path**
Travelled Distance (m)	4684.14	4274.57
Number of Ups	3	1
Number of Downs	3	1
Handover Count	3	2
Total Time (No Payload) (s)	609.30	548.92
Total PC (No Payload) (%)	13.89	12.57
Final Battery Level (No Payload) (%)	86.11	87.43
Total Time (Max Payload) (s)	609.30	548.92
Total PC (Max Payload) (%)	13.89	12.57
Final Battery Level (Max Payload) (%)	86.11	87.43
Mean Path Loss (dB)	96.17	96.61
Maximum PL (dB)	99.09	99.50
Minimum PL (dB)	91.01	92.21
95th Percentile PL (dB)	98.84	99.36
99th Percentile PL (dB)	99.04	99.47
Variance of Path Loss	4.74	4.93
LoS Percentage (%)	99.72	99.70
NLoS Percentage (%)	0.28	0.30

Table 5.3: Comparison of Path Loss Optimized vs. PD path using DJI FLyCart 30 for Path B

Metric	**PL Optimized**	**Std Shortest Path**
Travelled Distance (m)	7777.2672	7422.0310
Number of Ups	4	0
Number of Downs	4	0
Handover Count	3	4
Total Time (No Payload) (s)	470.21	381.10
Total PC (No Payload) (%)	58.77	54.91
Final Battery Level (No Payload) (%)	41.23	45.09
Total Time (Max Payload) (s)	470.21	381.10
Total PC (Max Payload) (%)	92.06	85.10
Final Battery Level (Max Payload) (%)	7.95	14.90
Mean Path Loss (dB)	96.80	96.51
Maximum PL (dB)	99.97	99.97
Minimum PL (dB)	92.06	91.89
95th Percentile PL (dB)	99.54	98.97
99th Percentile PL (dB)	99.95	99.83
Variance of Path Loss	4.65	2.53
LoS Percentage (%)	100.00	100.00
NLoS Percentage (%)	0.00	0.00

The results highlight the advantages of optimizing paths based on PL over selecting the standard shortest path. Specifically, in both Path A and Path B, the PL-optimized paths demonstrate key benefits for communication reliability:

- For Path A, the results indicate that the PL-optimized path introduces a **higher number of handovers** (three versus two) compared to the shortest path. Frequent handovers are typically undesirable in UAV communications, as they can introduce latency and potential link failures. However, this drawback is compensated by an **improved average path loss** and **a lower percentage of time spent in Non-Line-of-Sight (NLoS) conditions**.
- For Path B, while the **mean path loss** is slightly higher than in the shortest path, it achieves **fewer handovers** (three versus four), which is beneficial in reducing communication disruptions. Concerning instead the percentage of flight done in NLoS they are both at 0 since (as also shown in the elevation profile) both the start and end points are at a high altitude, being 60 meters from ground.

Another important aspect that should be consider is, obviously, the selection of start and end points. Keeping as test set *path A* and *path B*, these two examples are selected to analyze the general behavior of the algorithm using PL-based weights in worst case scenarios. In particular we can see:

- *Path A*: the start point is in a urbanized area, adjacent to a BS. The path gradually shifts towards a remote and less covered area.
- *Path B*: viceversa, in this path the starting point is in the lower extreme of the map, far from the base stations, while the destination point a few kilometers further north ends up in a built-up area.

With this in mind, the results of the various path losses measured along the route are consistent with the statements made before, as also shown in figures 5.8 and 5.9. The results suggest that the path losses suffered along the route are actually greater in areas further away from the BSs (and consequently from population centers). The path loss trend for route A is, in fact, increasing, and vice versa for route B.
These results confirm that the PL-optimized approach strategically adapts the UAV's trajectory to improve connectivity. By reducing handovers/average PL whenever possible and ensuring a more uniform signal strength. This is clearly strictly dependent on the geographical location the drone is to take-off or land. Although total travel distance and battery consumption are slightly higher, the trade-off results in enhanced connectivity, which is critical for BVLoS drone operations.

5.2.1 Performance Analysis of different drones - default scenario

In this subsection, we analyze the performance of different drones along predefined paths, considering their technical constraints and endurance capabilities, previously

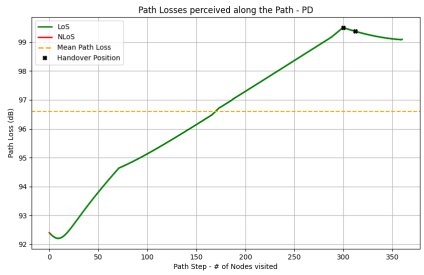

(a) Path A - Path Loss suffered for PD-based weights

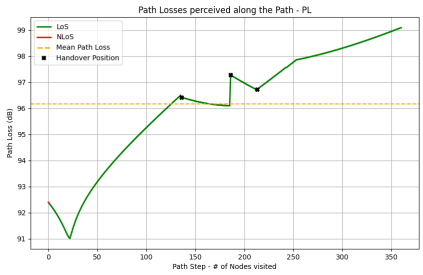

(b) Path A - Path Loss suffered for PL-based weights

Figure 5.8: Representation of path Losses suffered along paths A

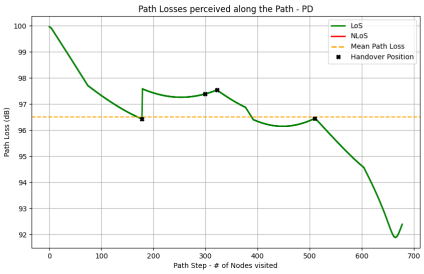

(a) Path B - Path Loss suffered for PD-based weights

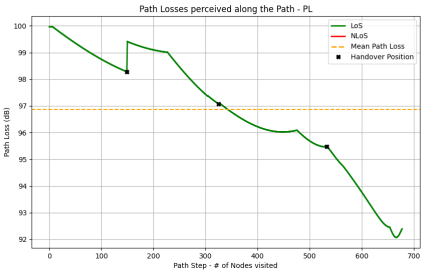

(b) Path B - Path Loss suffered for PL-based weights

Figure 5.9: Representation of path Losses suffered along paths B

described in table 5.1. As already mentioned, there are no plans for the Avata drone to carry payloads of any kind, as its small size and capacity make it more suitable for precision manoeuvres rather than for transporting objects. However, even with its small size, it is able to cover longer distances, even surpassing the Inspire 3 in terms of total travel distance. This is because the Avata 2 was specifically designed to operate in BVLoS scenarios where possible, optimizing its battery consumption for extended missions.
On the other hand, while the Inspire 3 excels in terms of speed and maximum altitude, its power consumption is higher, leading to a shorter operational time before battery depletion.

Since Paths C and D have not been previously analyzed, they are now selected for performance evaluation. The following figures 5.10, 5.11 and 5.12 present detailed results, including energy consumption and battery depletion trends, to assess the feasibility and efficiency of each drone along its designated path.
The first plot in these figures displays the energy consumption (in watt-hours, Wh) along the path. The x-axis represents the *path step*, while the y-axis represents the energy consumption per step. Notably, the y-axis is logarithmic, to better visualize the result. The second graph in each case displays the battery level (as a percentage of total capacity) along the path. The x-axis represents again the *path*

step, while the y-axis represents the battery level in percentage (%).

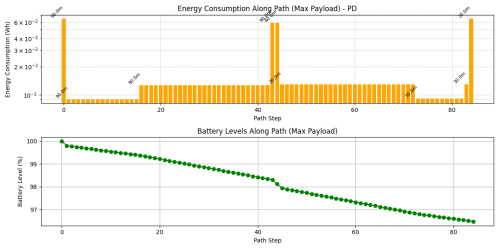

(a) Path C - Power Consumption for PD-based weight graph

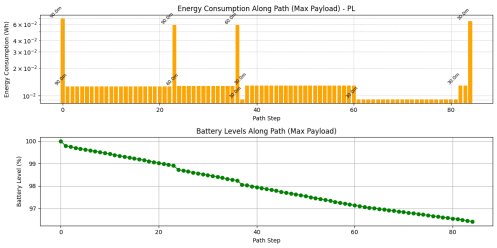

(b) Path C - Power Consumption for PL-based weight graph

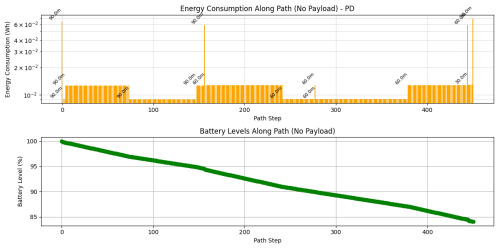

(c) Path D - Power Consumption for PD-based weight graph

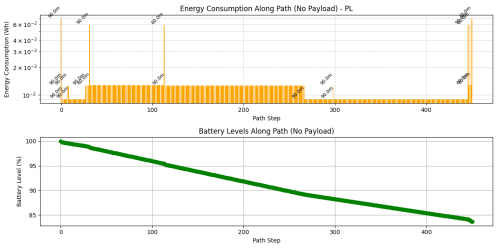

(d) Path D - Power Consumption for PL-based weight graph

Figure 5.10: Power consumption of the Avata drone along path C & D

Figure 5.10 analyzes the energy consumption and battery levels of the *DJI Avata* drone using PD weight-based and PL weight-based respectively. The drone's technical specifications include a total battery capacity of:

$$\text{Battery Energy Capacity} = \frac{2150\,\text{mAh} \times 14.76\,\text{V}}{1000} = 3173.4\,\text{Wh}.$$

Energy consumption values range approximately between 10^{-2} Wh (0.01 Wh) during steady-state flight and peak at around 6×10^{-2} Wh (0.06 Wh) during moments of increased energy demand.
The energy consumption shows a consistent trend across both scenarios:

- **Takeoff and Landing:** The initial spike in energy consumption corresponds to the drone's takeoff phase. Similarly, a final spike represents the landing phase. These activities require additional power to overcome gravitational forces.
- **Steady-State Flight:** During horizontal flight, the energy consumption stabilizes at lower values, reflecting the reduced power demand compared to vertical maneuvers.
- **Additional Peaks:** Whenever "downward movements" happen (two in these cases) along the z-axis, it may cause additional peaks in energy consumption. These maneuvers likely correspond to controlled descents, requiring higher power to maintain stability.

In both scenarios, the battery level exhibits a gradual decline over time, consistent with the energy consumption trends. In the first case (PD), where the total distance is shorter (1125.21 m), the battery depletion is minor with respect to the second case (PL), where the total distance is greater (1141.77 m). In this last case the battery depletion is slightly higher, reflecting the higher energy demands of a longer flight.

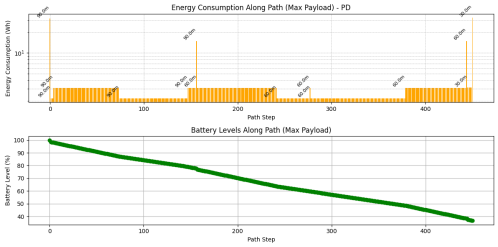

(a) Path D - Power consumption using max payload (PD)

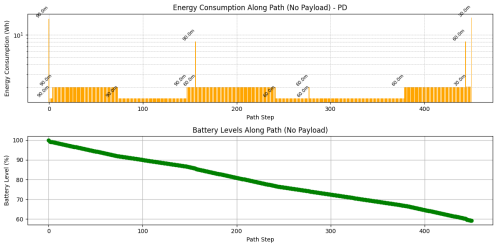

(b) Path D - Power consumption using no payload (PD)

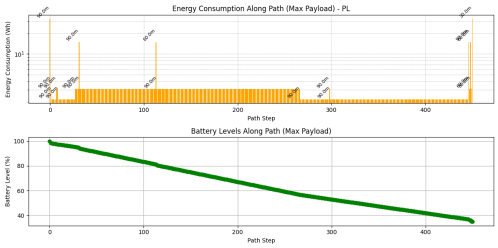

(c) Path D - Power consumption using max payload (PL)

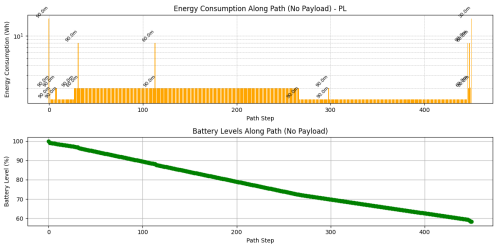

(d) Path D - Power consumption using no payload (PL)

Figure 5.11: Power consumption of the FlyCart30 drone along path D

Using a more appropriate drone for long-distance transport tasks, the results for the *DJI FLyCart 30* are displayed in figures 5.11, representing *path D*. Differently with respect to the Avata case, in here the results refer to a longer traveled distance, comparing the case in which the drone is carrying the maximum possible payload with the case without it.
For the *FlyCart 30* drone, the energy consumption is expected to be significantly higher than the *DJI Avata* due to its larger size, higher weight, and greater power requirements. The energy consumption plot reveals:

- A baseline consumption that remains steady during level flight, with occasional **peaks** corresponding to changes in altitude, acceleration, or sharp maneuvers. For example:
  - Peaks around the initial path steps are likely due to takeoff or an increase in vertical speed.
  - Additional peaks occur during descent or ascent phases, which align with the presence of "ups" (only 1 for PL case) and "downs" (2 for PD case and 3 for PL case) in the path.

- When payload is added (30 kg for *DJI FlyCart 30*), the range of energy consumption increases across the path steps, reflecting the greater energy demands required to sustain flight under higher weight.
- The overall energy consumption ranges from about 0.01 Wh in steady flight to above 10 Wh during peaks, consistent with the drone's power requirements.

Given the *FlyCart 30*'s battery specifications:

$$\text{Battery Energy Capacity} = \frac{38000\,\text{mAh} \times 52.22\,\text{V}}{1000} = 1984.36\,\text{Wh}.$$

The battery level plots further illustrate the energy demands, decreasing linearly with minor deviations. **With Maximum Payload** the battery drain is more pronounced due to the additional load. Additionally, the energy consumption during ascent and descent maneuvers with payload (as evidenced by the peaks) further contributes to this accelerated battery depletion bor both cases.
The total power consumption percentages for the analyzed paths are as follows:

- **No Payload:** 41.62% (PD) and 42.53% (PL).
- **Max Payload:** 64.91% (PD) and 66.57% (PL).

While for battery level the final results for *path D* are:

- **No Payload:** 58.38% (PD) and 57.47% (PL).
- **Max Payload:** 35.08% (PD) and 33.43% (PL).

For what concern the last type of UAV, the DJI Inspire 3, similar conclusions can be made by looking figures 5.12, whose battery specifications include a total battery capacity of:

$$\text{Battery Energy Capacity} = \frac{4280\,\text{mAh} \times 23.1\,\text{V}}{1000} = 1984.36\,\text{Wh}.$$

Again the trends are coherent with what was mentioned previously, presenting peaks at take-off and landing heights, as well as at ups and downs movements along z-axis. The energy consumption plots, ranging between 0.2 Wh to 1 Wh, presents:

- **PD case:** 2 downs and 0 ups movements.
- **PL case:** 3 downs and 1 up movements.

In summary, the power consumption as well as the final battery levels are:

- **No Payload PD:** 79.80% and final battery level 20.20%.
- **No Payload PL:** 81.08% and final battery level 18.91% (PL).
- **Max Payload PD:** 85.85% and final battery level 14.14%.

- **Max Payload PL:** 87.27% and final battery level 12.72% (PL).

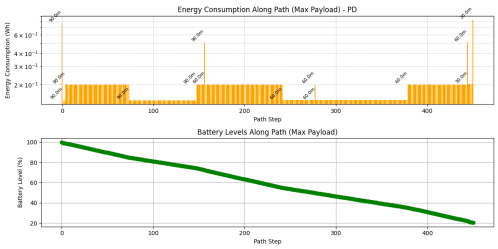

(a) Path D - Power Consumption and battery level with max payload (PD)

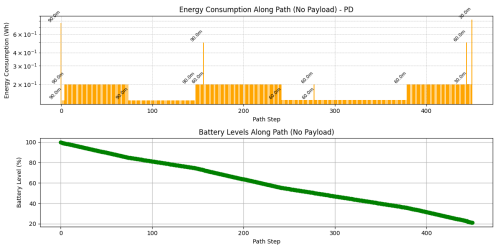

(b) Path D - Power Consumption and battery level with no payload (PD)

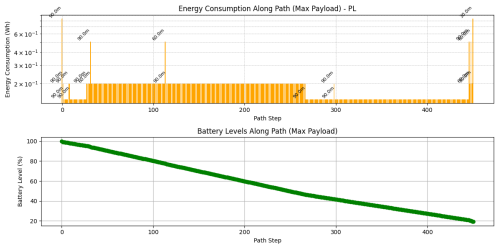

(c) Path D - Power Consumption and battery level with max payload (PL)

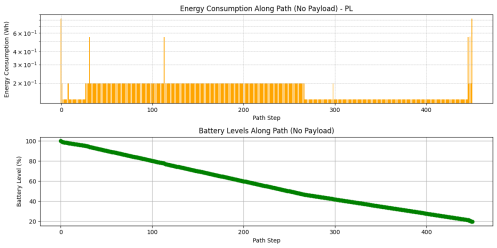

(d) Path D - Power Consumption and battery level with no payload (PL)

Figure 5.12: Power consumption of the Inspire 3 drone along path D

5.2.2 Analysis of supported technologies - default scenario

During the drone's flight, the primary technologies used for connectivity varied depending on the weighting approach. Again the focus will be for path A and B, which presented a series of handovers during flight, thus it will be more interesting looking at the different types of antennas which were exploited.

The presence of 4G technologies displayed in figures 5.13 for PL-based paths, particularly at lower frequencies, suggests that their broader coverage areas made them favorable for maintaining connectivity over longer distances, despite the availability of 5G.
For PD-based weights instead the dominance shifts significantly to 5G tech. This indicates that when prioritizing the shortest path, the network favored 5G, that still being at lower frequencies guarantee the coverage but poorer performance.
As already mentioned in chapter four, another scenario is tested to see the impact of removing the 4G 700MHz and 800MHz antennas, in favor to those who were not considered due to higher Path Losses. For both path A and B, and for both PD and PL types of weight the results are identical, as shows figure 5.14 that reports only 2 of the 4 results since are all identical.

The results demonstrate that 5G at 800MHz is capable of sustaining connectivity across the trajectory in the absence of alternative lower-frequency 4G bands.

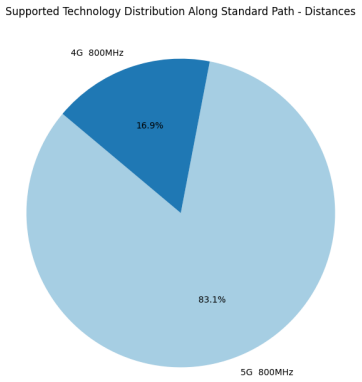

(a) Path A - Supported tech exploited for PD-based weights

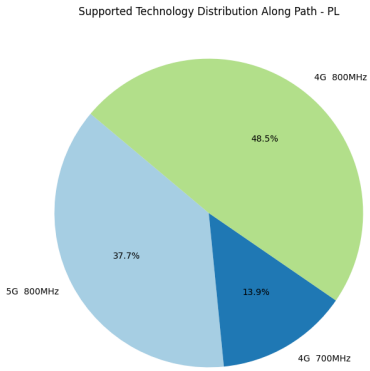

(b) Path A - supported tech exploited for PL-based weights

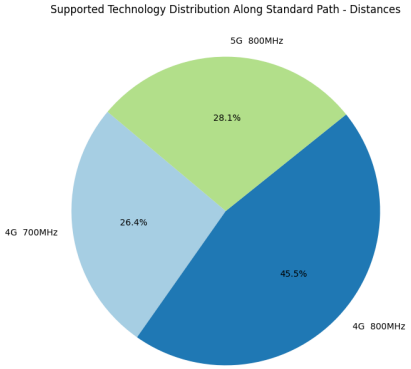

(c) Path B - supported tech exploited for PD-based weights

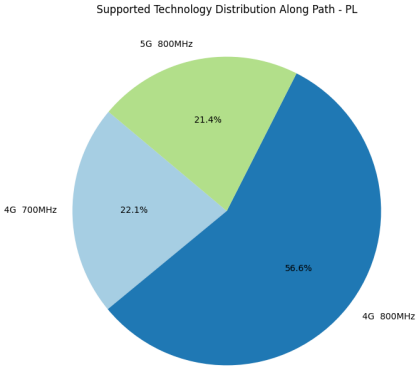

(d) Path B - supported tech exploited for PL-based weights

Figure 5.13: Pie charts - Supported Technologies

However, it also suggests that without 4G support, this setting could support the trajectory but with slightly higher path loss variability, being equal to, for example in path A to:

- 97.14 dB versus 96.17 dB for PL-based in path A.
- 97.02 dB versus 96.61 dB for PD-based in path A.

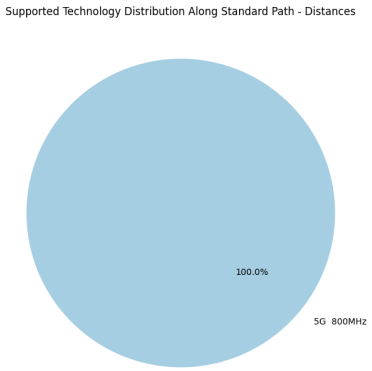

(a) Path A - Supported tech with no 4G antennas (PD)

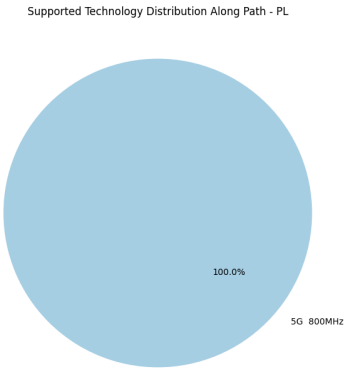

(b) Path B - Supported tech with no 4G antennas (PL)

Figure 5.14: Supported techs with no 4G 700/800 MHz antennas

5.3 Performance Analysis of second scenario - 4-layered graph

In this second scenario, the constructed graph includes an additional layer along the z-axis, making it more discrete and allowing for the formation of a greater number of traversable arcs, as shown in Table 3.1. The added z-layer represents a 10-meter band above the ground, meaning that flying at this height may be more challenging due to an increased probability of encountering obstacles.
The paths analyzed in this scenario differ from the standard case in the z-plane. This choice was made to broaden the variety of results and assess how different altitudes influence the findings.
The 2D plots of the main paths can be seen in figures 5.15, 5.16, 5.17 and 5.18.

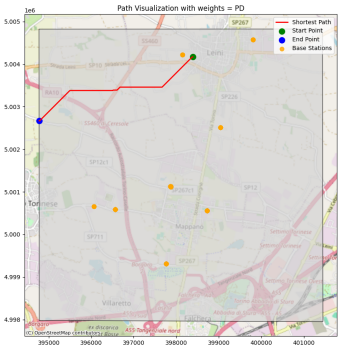

(a) Path A with PD weights selection

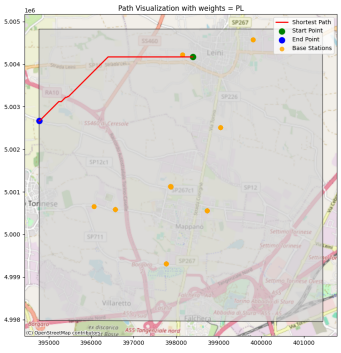

(b) Path A with PL weights selection

Figure 5.15: Path A for the 4-layered graph - PD & PL weight-based comparison.

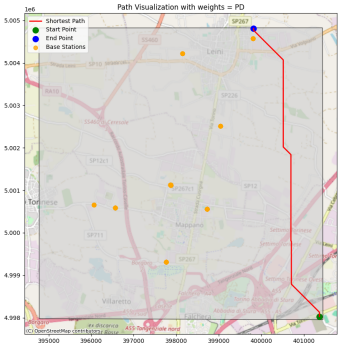

(a) Path B with PD weights selection

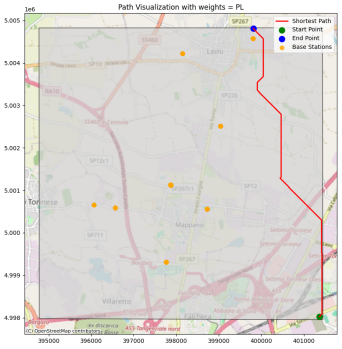

(b) Path B with PL weights selection

Figure 5.16: Path B for the 4-layered graph - PD & PL weight-based comparison.

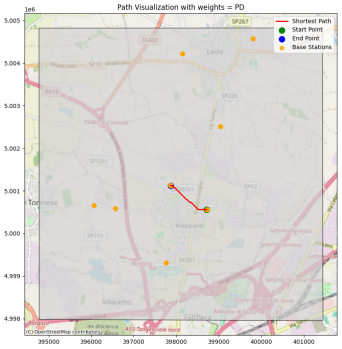

(a) Path C with PD weights selection

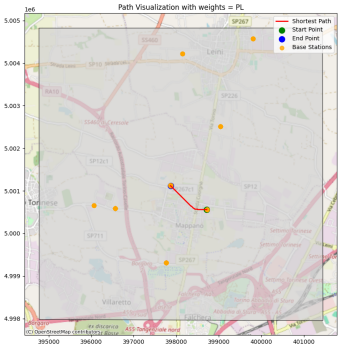

(b) Path C with PL weights selection

Figure 5.17: Path C for the 4-layered graph - PD & PL weight-based comparison.

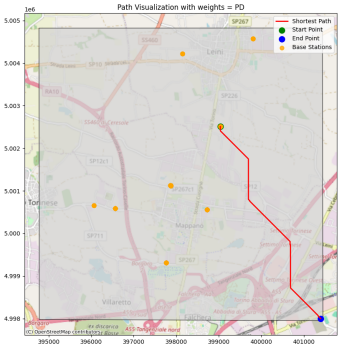

(a) Path D with PD weights selection

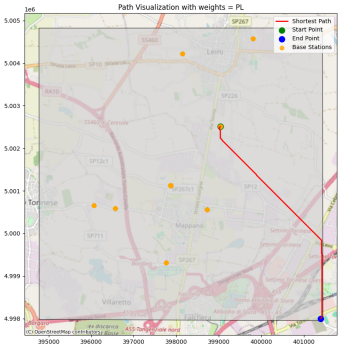

(b) Path D with PL weights selection

Figure 5.18: Path D for the 4-layered graph - PD & PL weight-based comparison.

On the 2D plane, the results appear very similar to those in Figure 5.1, with only slight differences. These variations are mainly caused by differences in the altitude of the start and/or destination points, as well as the presence of an additional layer on which the drone can navigate. The key distinction between the PD and PL cases remains evident, highlighted by the deviations observed in the PL case compared to the PD case.

For a clearer understanding, Figures 5.19 and 5.20 present the 3D trajectories of *Path A* and *Path C*. The elevation models for *Path A* can be compared with those in Figure 5.6, where the PL case exhibits more frequent altitude variations before reaching the destination. This behavior is particularly noticeable when approaching a base station along the route. Such deviations are also reflected in the handovers occurring at the same nodes, justifying the 'change of course' as an optimization strategy to enhance signal reception from the BS.
Despite these changes, the shortest physical path remains identical to the one obtained using the default graph. Since no modifications were made along the x- and y-axes, the shortest route in terms of horizontal distance remains unchanged.

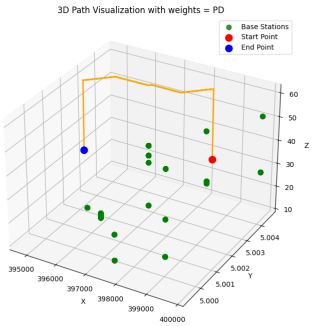

(a) Path A - 3D plot using PD

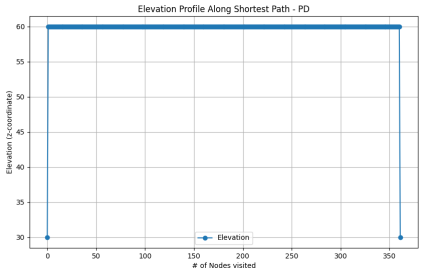

(b) Path A - elevation profile using PD

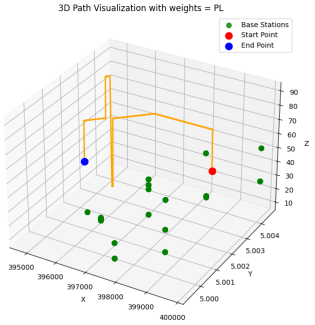

(c) Path A - 3D plot using PL

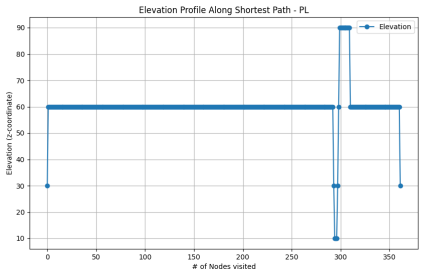

(d) Path A - elevation profile using PL

Figure 5.19: Path A - focus on displacements along the z-axis

Another example is illustrated in Figure 5.20, which represents the shortest route observed so far. Given the relatively short total distance, no major influencing

factors—such as intermediate base stations or obstacles—are present. Consequently, the final results exhibit similar behavior across cases.

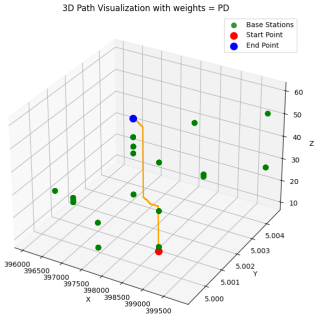

(a) Path C - 3D plot using PD

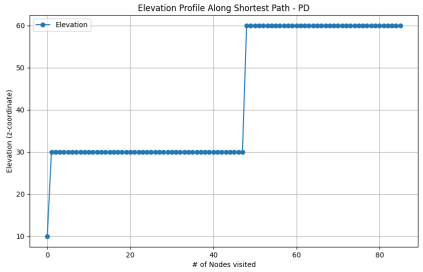

(b) Path C - elevation profile using PD

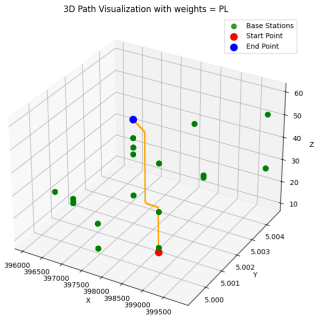

(c) Path C - 3D plot using PL

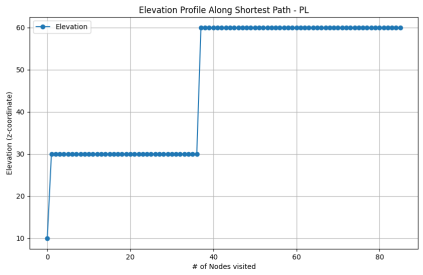

(d) Path C - elevation profile using PL

Figure 5.20: Path C - focus on displacements along the z-axis

As done previously, Tables 5.4 and 5.5 summarize the key metrics obtained for Paths A and C. The observations for Path A remain consistent, with an equal number of handovers and a lower average PL.

Table 5.4: Comparison of Path Loss Optimized vs. PD path using DJI Inspire 3 for Path A

Metric	**PL Optimized**	**STD Shortest Path**
Travelled Distance (m)	4385.77	4274.56
Number of Ups	4	1
Number of Downs	4	1
Handover Count	2	2
Total Time (No Payload) (s)	200.24	180.2
Total PC (No Payload) (%)	63.92	61.98
Final Battery Level (No Payload) (%)	36.07	38.02
Total Time (Max Payload) (s)	200.24	180.24
Total PC (Max Payload) (%)	68.87	66.71
Final Battery Level (Max Payload) (%)	32.13	33.29
Mean Path Loss (dB)	96.09	96.61
Maximum PL (dB)	99.39	99.50
Minimum PL (dB)	91.00	92.20
95th Percentile PL (dB)	99.33	99.36
99th Percentile PL (dB)	99.38	99.47
Variance of Path Loss	6.83	4.93
LoS Percentage (%)	99.72	99.70
NLoS Percentage (%)	0.28	0.30

Regarding Path C, physical metrics such as drone power consumption, total flight time, distance traveled, and battery level show no significant variations. However, a stronger focus should be placed on communication KPIs. Since this route is entirely within a populated area, starting under one base station and reaching a second, noticeable differences emerge in the number of handovers and the percentage of NLoS occurrences.
In the PL-based case, performance is optimized by minimizing unnecessary handovers along the trajectory. Additionally, since this path traverses an urbanized area, a small fraction of it occurs in NLoS conditions. This is primarily due to the starting point being located behind a warehouse, which obstructs the signal from the neighboring base station.

To validate the observations above, Figure 5.21 illustrates the PL values experienced at each node along the trajectory.

Table 5.5: Comparison of Path Loss Optimized vs. PD path using DJI Inspire 3 for Path C

Metric	**PL Optimized**	**STD Shortest Path**
Traveled Distance (m)	1115.94	1115.94
Number of Ups	2	2
Number of Downs	0	0
Handover Count	3	5
Total Time (No Payload) (s)	57.86	57.86
Total PC (No Payload) (%)	17.24	17.26
Final Battery Level (No Payload) (%)	82.75	82.74
Total Time (Max Payload) (s)	57.86	57.86
Total PC (Max Payload) (%)	18.64	18.66
Final Battery Level (Max Payload) (%)	81.35	81.34
Mean Path Loss (dB)	91.66	91.66
Maximum PL (dB)	93.51	93.51
Minimum PL (dB)	88.97	88.98
95th Percentile PL (dB)	93.31	93.31
99th Percentile PL (dB)	93.48	93.48
Variance of Path Loss	1.10	1.12
LoS Percentage (%)	98.85	98.85
NLoS Percentage (%)	1.15	1.15

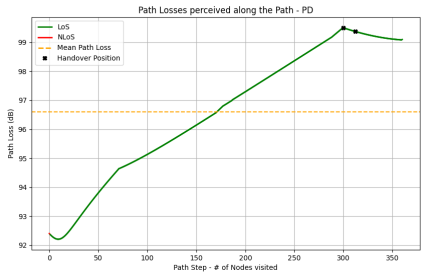

(a) Path A - Path Loss suffered for PD-based weights

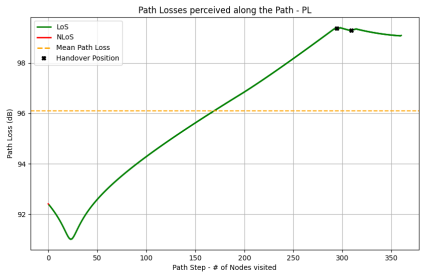

(b) Path A - Path Loss suffered for PL-based weights

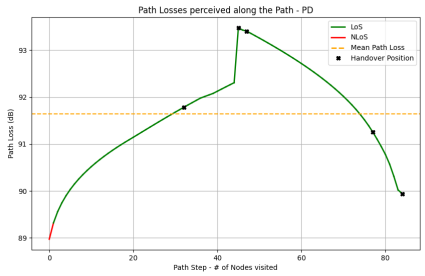

(c) Path C - Path Loss suffered for PD-based weights

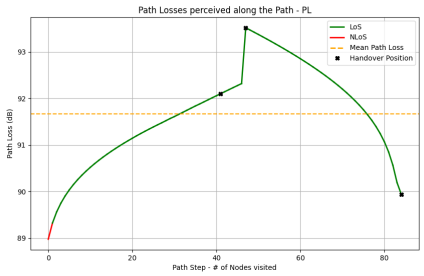

(d) Path C - Path Loss suffered for PL-based weights

Figure 5.21: Representation of path Losses suffered on paths A and C

Focusing on plots 5.21d and 5.21c, it is important to note the red line at the beginning of the graph, which represents the initial NLoS steps.

5.3.1 Performance Analysis of different drones - 4-layers scenario

This section presents the results obtained for *Path A*, as Path C does not exhibit any significant deviations from the default scenario. As previously mentioned, the plots 5.22, 5.23, 5.24 illustrate the trends in battery level and power consumption at each step.

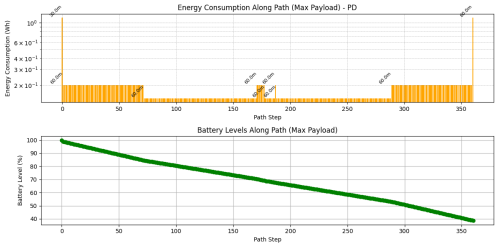

(a) Path A - Power Consumption & battery level with max payload (PD)

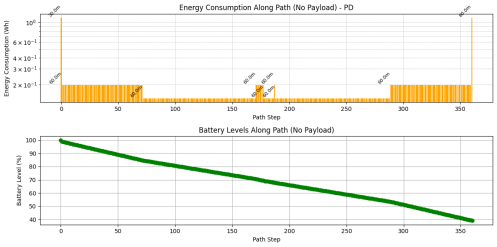

(b) Path A - Power Consumption & battery level with no payload (PD)

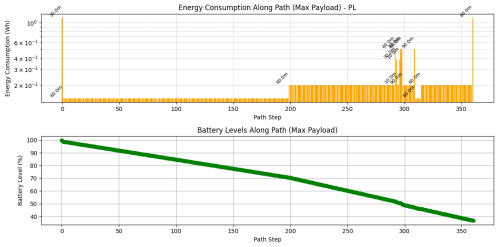

(c) Path A - Power Consumption & battery level with max payload (PL)

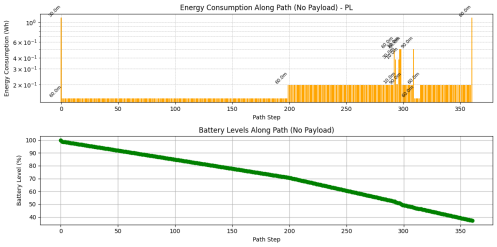

(d) Path A - Power Consumption & battery level with no payload (PL)

Figure 5.22: Power Consumption and battery level trends using Inspire 3 along path A

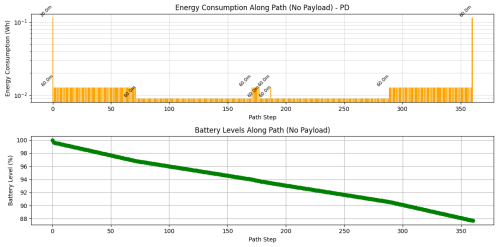

(a) Path A - Power Consumption & battery level (PD)

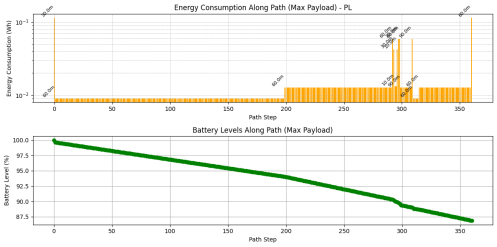

(b) Path A - Power Consumption & battery level (PL)

Figure 5.23: Power Consumption and battery level trends using Avata 2 along path A

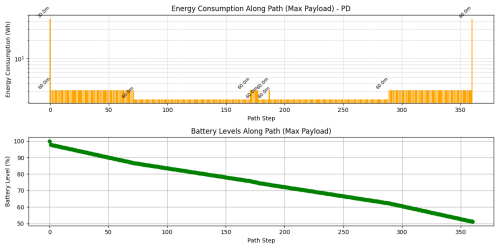

(a) Path A - Power Consumption & battery level with max payload (PD)

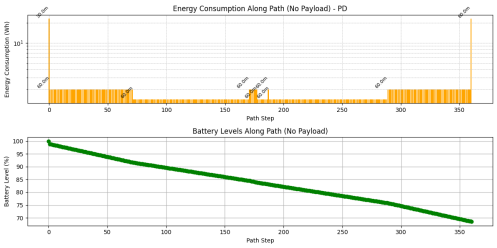

(b) Path A - Power Consumption & battery level with no payload (PD)

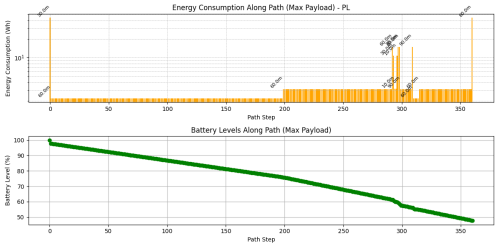

(c) Path A - Power Consumption & battery level with max payload (PL)

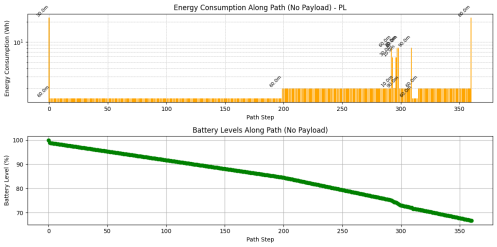

(d) Path A - Power Consumption & battery level with no payload (PL)

Figure 5.24: Power Consumption and battery level trends using FlyCart 30 along path A

Consistent with the previous findings, the altitude variations along the z-axis in the PL case have led to significant spikes in energy consumption for both the *DJI Inspire 3*, *DJI Avata 2* and *DJI FlyCart 30* drones, significantly impacting the final results, as shown in Table 5.6. The results shown for the case with maximum payload refer for the *DJI FlyCart 30* to 30 kg maximum, and for the *DJI Inspire 3* to 0.043 kg.

Metrics Name	**PL case**	**PD case**
Traveled distance	Inspire: 4385.77 FlyCart: 4385.77 Avata: 4385.77	Inspire: 4274.56 FlyCart: 4274.56 Avata: 4274.56
Total PC (No P)	Inspire: 63.92% FlyCart: 34.40% Avata: 13.49%	Inspire: 61.98% FlyCart: 32.61% AVata: 12.66%
Final Battery (No P)	Inspire: 36.08% FLyCart: 65.6% Avata: 86.50%	Inspire: 38.02% FlyCart: 67.38% Avata: 87.34%
Total PC (Max P)	Inspire: 64.45% FlyCart: 54.48% Avata: 13.49%	Inspire: 62.49% FlyCart: 51.06% Avata: 12.66%
Final Battery (Max P)	Inspire: 35.55% FlyCart: 45.52% Avata: 86.50%	Inspire: 37.51% FlyCart: 48.93% Avata: 87.34%

Table 5.6: Metrics Comparison for PL and PD Cases

As expected, the FlyCart 30 performs better over longer distances due to its more powerful battery, despite its total weight of 52.5 kg, further burdened by the payload of 30 kg in the corresponding cases.
In contrast, the Inspire 3 is designed for aerial filming, prioritizing higher velocities at the expense of increased energy consumption, nearly double that of the FlyCart 30.
Among the tested drones, the DJI Avata 2 exhibited the best performance, maintaining the highest remaining battery levels across all scenarios. This advantage is primarily due to its lack of additional payload, significantly reducing energy consumption. Furthermore, its sustained speed allows it to reach its destination efficiently without excessive battery depletion, making it particularly well suited for missions requiring extended flight endurance.

5.3.2 Analysis of supported technologies - 4-layers scenario

Also, for the 4-layer scenario, the most commonly supported technologies are lower-frequency 4G LTE bands, specifically 700 MHz and 800 MHz, along with occasional support for 5G at 800 MHz. The results do not differ significantly from the default case, yielding identical plots for *path A*. However, for the remaining three paths, the results are presented in the figures below (see 5.25, 5.26 and 5.27). A particular focus should be placed on *path C*, as it exhibits a greater variety of technologies. During this flight, the drone traverses an urban area, starting near one base station and concluding near another. Given that the total distance is slightly over one kilometer, configuring the algorithm to use PL-based weights effectively prevents unnecessary handovers. In contrast, when using PD-based weights, the system still performs multiple unnecessary handovers throughout the flight, as also highlighted in Table 5.5.

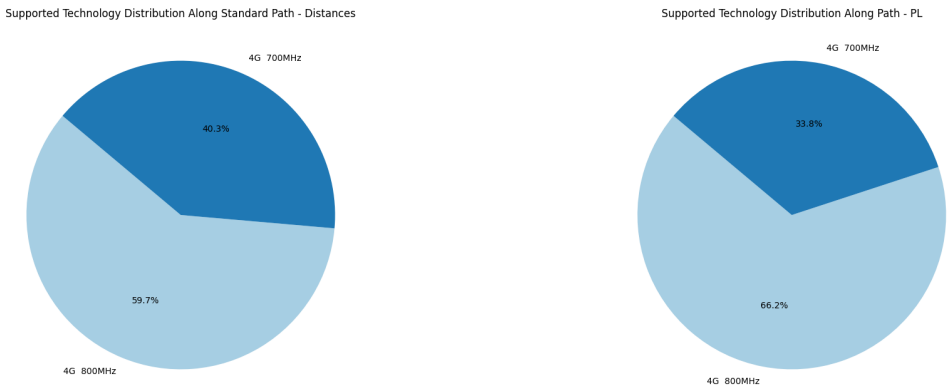

(a) Path B - Supported tech exploited for PD-based weights

(b) Path B - supported tech exploited for PL-based weights

Figure 5.25: Pie charts B- Supported Technologies for 4 layer graph

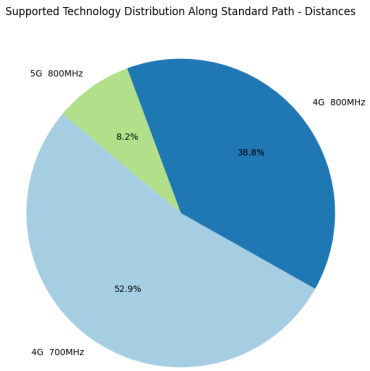

(a) Path C - supported tech exploited for PD-based weights

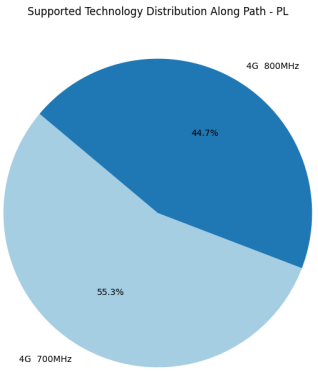

(b) Path C - supported tech exploited for PL-based weights

Figure 5.26: Pie charts C- Supported Technologies for 4 layer graph

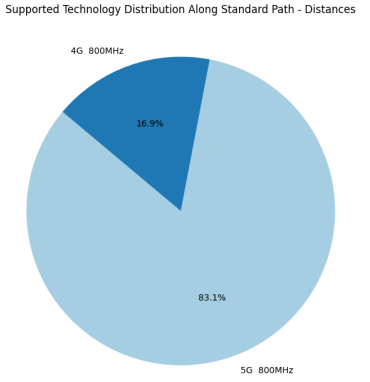

(a) Path D - supported tech exploited for PD-based weights

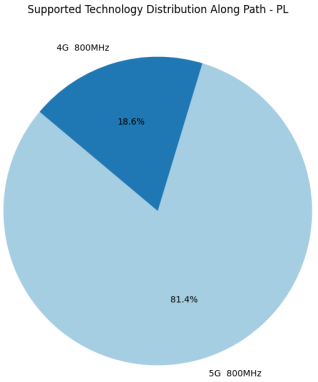

(b) Path D - supported tech exploited for PL-based weights

Figure 5.27: Pie charts D- Supported Technologies for 4 layer graph

To further analyze the impact of lower-frequency 4G technologies, an additional test is conducted in which all 4G 700/800 MHz and 5G 800 MHz bands are removed. The results indicate that, across all paths, the drone consistently utilizes the next available technology, which is 4G at 1800 MHz, as illustrated in Figure 5.28. The pie charts remain unchanged across different paths, reflecting this fallback mechanism.

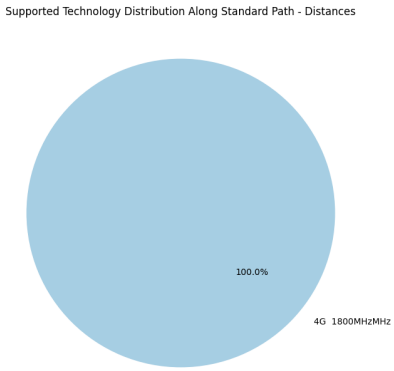

(a) Path B -supported tech exploited for PD-based weights no 700-800 MHz techs

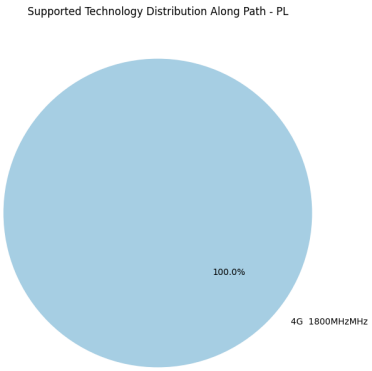

(b) Path B - supported tech exploited for PL-based weights no 700-800 MHz techs

Figure 5.28: Pie charts - Supported Technologies for 4 layer graph with no 700-800 MHz techs

These findings suggest that removing lower-frequency base stations should have influenced the original path selection. Indeed, the absence of these base stations negatively impacted overall performance. Differently with respect to the default case, where only 4G 700/800 MHz bands are removed, the scenario is further deteriorated by the removal of even the 5G 800 MHz band, causing a significant deterioration in performance.

The results presented in Table 5.7 demonstrate this degradation.

Paths	**PL-based weights**		**PD-based weights**	
	STD	**NO 700-800 MHz**	**STD**	**NO 700-800 MHz**
Path A	96.09 #H=2	103.02 #H=1	96.6 #H=2	102.90 #H=4
Path B	96.86 #H=3	102.56 #H=4	96.56 #H=4	104.57 #H=4
Path C	91.66 #H=3	99.35 #H=3	91.66 #H=5	99.35 #H=3
Path D	96.07 #H=2	103.12 #H=2	96.15 #H=2	102.95 #H=4

Table 5.7: PL-based and PD-based weights for different paths.

Analyzing the results in the Table 5.7, it is evident that removing the 700-800 MHz bands leads to a clear degradation in performance when compared to the standard case. This degradation is even more pronounced than in the default scenario, where at least the 5G 800 MHz bands are still available.

The number of handovers remains relatively stable within the same weight type (PL-based or PD-based), with only a slight increase in the NO 700-800 MHz case. The major gap in total handovers is observed when comparing different weight types within the same scenario (either standard or NO 700-800 MHz). This suggests that

the choice of weight type has a more substantial influence on handover frequency than the mere removal of lower-frequency bands.
Regarding the comparison between PL-based and PD-based weights within the same scenario, it is observed that some cases exhibit higher mean path loss when using PL-based weights compared to their PD-based counterparts. However, this increase in path loss is balanced by a significantly lower number of handovers along the path, reinforcing the advantage of PL-based optimization in reducing unnecessary handovers while maintaining an acceptable communication quality.

5.4 Performance Analysis of third scenario - small graph

In this third scenario, the graph model is extended to include a higher level of discretization along the z-axis, incorporating a total of nine altitude layers. This increased granularity provides a more detailed representation of UAV mobility, allowing for finer altitude adjustments that can significantly influence path selection. The additional layers facilitate a greater number of traversable arcs, potentially offering improved connectivity but also increasing computational complexity.
The purpose of this scenario is to analyze how a higher-resolution altitude model impacts trajectory planning, communication performance, and energy consumption. The UAVs now have the flexibility to adjust their altitude more frequently.

As with the previous cases, the analysis compares paths computed using PL-based and PD-based weight assignments. Given the higher number of available altitude levels, it is expected that PL-based paths will take greater advantage of vertical displacements to optimize connectivity. Conversely, PD-based paths may attempt to minimize the number of altitude changes to reduce energy consumption.
The selected paths for this analysis, displayed in figures 5.29, 5.30, 5.31 and 5.32, include a diverse range of start and end locations to assess how different terrain conditions and base station distributions influence UAV flight. The upcoming sections will discuss in detail the impact of this increased discretization on UAV trajectory selection, power efficiency, and network handover events.

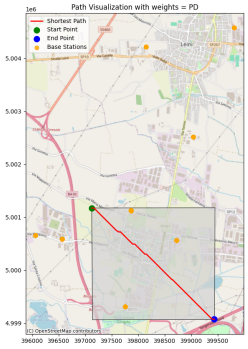

(a) Path A with PD weights selection

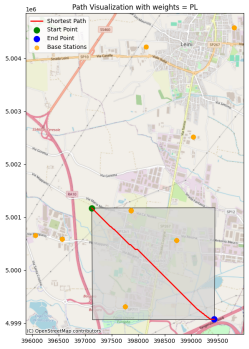

(b) Path A with PL weights selection

Figure 5.29: Path A for small graph - PD & PL weight-based comparison.

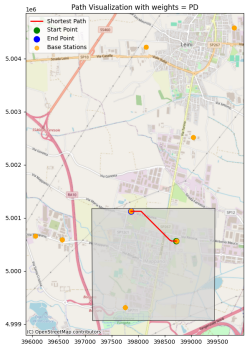

(a) Path B with PD weights selection

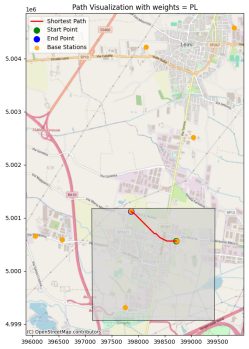

(b) Path B with PL weights selection

Figure 5.30: Path B for small graph - PD & PL weight-based comparison.

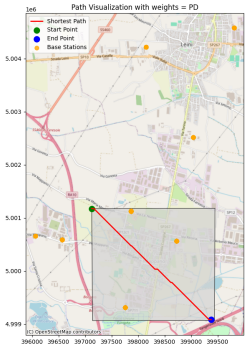

(a) Path C with PD weights selection

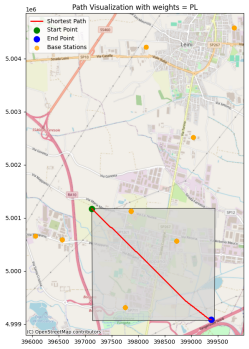

(b) Path C with PL weights selection

Figure 5.31: Path C for small graph - PD & PL weight-based comparison.

(a) Path D with PD weights selection (b) Path D with PL weights selection

Figure 5.32: Path D for small graph - PD & PL weight-based comparison.

To further investigate connectivity performance, two representative paths are selected: a shorter path (Path B) and a longer path (Path C). Both paths traverse the town center, with takeoff or landing near one of the base stations in the area. For comparison, Path A and Path C represent longer routes spanning the diagonal of the available area, covering both urban and rural environments, including open fields. These longer paths introduce additional variability in signal propagation due to diverse terrain conditions. They may differ only for the z starting and ending points.
Path B and Path D instead are shorter paths which begin (or end) in a flat area, arriving (or departing) from a more densely populated area, possibly near a BS.

The following figures 5.33 and 5.34 present the 3D plots and elevation profiles of the selected paths, providing information on the influence of terrain on communication performance.
Each elevation profile depicts variations in terrain height along the communication path, highlighting also for this scenario the major deviations, compared to the shortest route, of the optimized route for PLs.

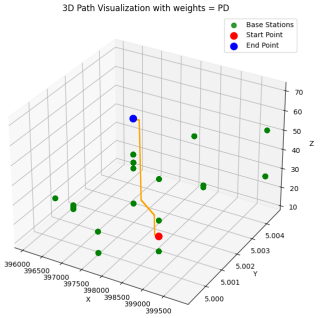

(a) Path B - 3D plot using PD

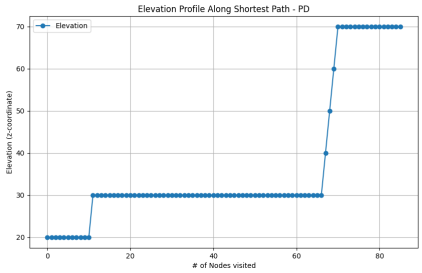

(b) Path B - elevation profile using PD

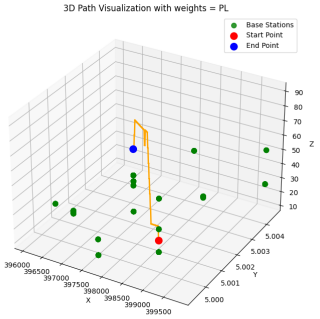

(c) Path B - 3D plot using PL

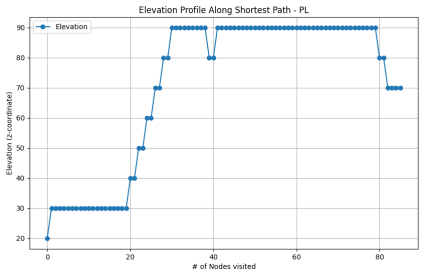

(d) Path B - elevation profile using PL

Figure 5.33: Path B - focus on displacements along the z-axis

Despite some fluctuations in the paths generated by the PL-based weights, and despite the shorter distances compared to previous scenarios, the increased height levels and more discretized space significantly reduced the total distance traveled. This optimization of PLs consequently led to lower energy consumption for the drone, as will be demonstrated in the following sections. Similar elevation trends can also be observed for paths A and D.

A general overview of the main KPIs for both *path B* and *path C* are reported in tables 5.8 and 5.9.
Even when using a more discretized graph over a smaller area, the results remain consistent with initial expectations, further supporting the observations made for both the default and 4-layered graphs in terms of communication metrics.

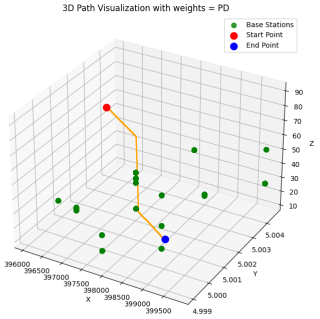

(a) Path C - 3D plot using PD

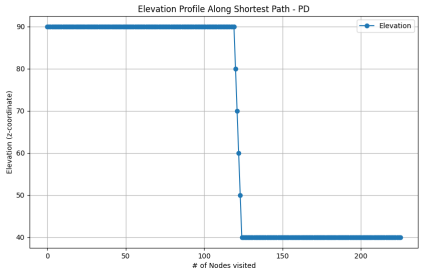

(b) Path C - elevation profile using PD

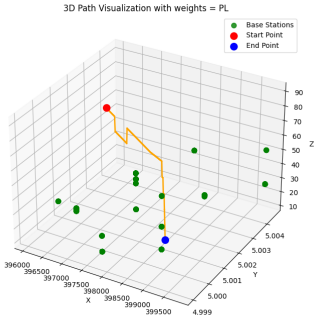

(c) Path C - 3D plot using PL

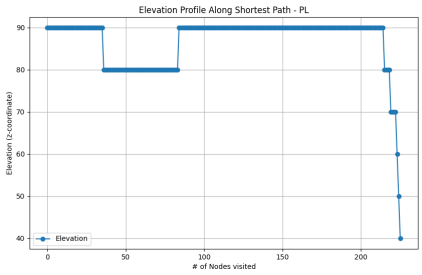

(d) Path C - elevation profile using PL

Figure 5.34: Path C - focus on displacements along the z-axis

Table 5.8: Comparison of PL vs. PD based paths using DJI Inspire 3 for Path B

Metric	**PL Optimized**	**STD Shortest Path**
Traveled Distance (m)	1127.52	1102.67
Number of Ups	8	5
Number of Downs	3	0
Handover Count	3	6
Total Time (No Payload) (s)	65.36	57.86
Total PC (No Payload) (%)	28.34	27.19
Final Battery Level (No Payload) (%)	71.66	72.81
Total Time (Max Payload) (s)	65.36	57.86
Total PC (Max Payload) (%)	30.69	29.40
Final Battery Level (Max Payload) (%)	69.30	70.60
Mean Path Loss (dB)	91.63	91.71
Maximum PL (dB)	93.47	93.47
Minimum PL (dB)	88.63	88.63
95th Percentile PL (dB)	93.27	93.37
99th Percentile PL (dB)	93.43	93.46
Variance of Path Loss	1.14	1.29
LoS Percentage (%)	100	100
NLoS Percentage (%)	0	0

Table 5.9: Comparison of PL vs. PD based paths using DJI Inspire 3 for Path C

Metric	**PL Optimized**	**STD Shortest Path**
Traveled Distance (m)	3144.7	3136.41
Number of Ups	1	0
Number of Downs	6	5
Handover Count	5	7
Total Time (No Payload) (s)	138.58	136.08
Total PC (No Payload) (%)	72.39	72.16
Final Battery Level (No Payload) (%)	27.60	27.84
Total Time (Max Payload) (s)	138.58	136.08
Total PC (Max Payload) (%)	77.99	77.72
Final Battery Level (Max Payload) (%)	22.01	22.28
Mean Path Loss (dB)	93.54	93.46
Maximum PL (dB)	95.32	96.43
Minimum PL (dB)	92.27	92.17
95th Percentile PL (dB)	95.07	95.05
99th Percentile PL (dB)	95.30	96.11
Variance of Path Loss	0.62	0.70
LoS Percentage (%)	100	100
NLoS Percentage (%)	0	0

To validate these findings, Figure 5.35 illustrates the PL values experienced at each node along the trajectory. As previously stated in Tables 5.8 and 5.9, the number of handovers in PD-based paths is significantly higher than in their corresponding PL-based counterparts, increasing the likelihood of communication issues, such as disconnections, during the flight.

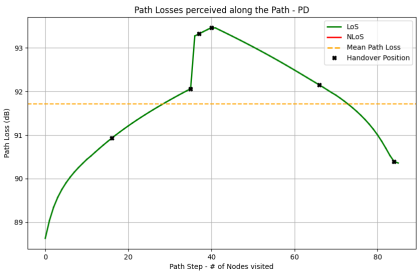

(a) Path B - Path Loss suffered for PD-based weights

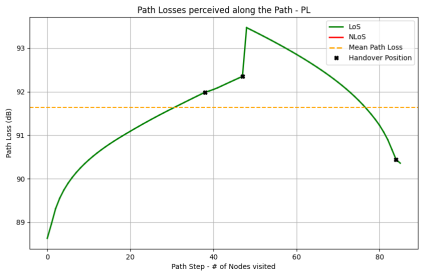

(b) Path B - Path Loss suffered for PL-based weights

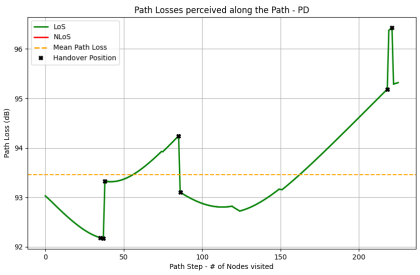

(c) Path C - Path Loss suffered for PD-based weights

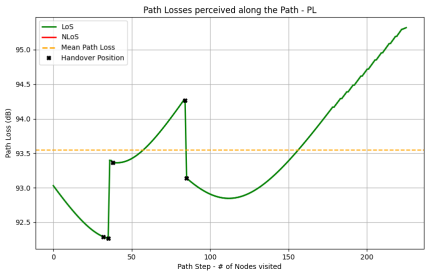

(d) Path C - Path Loss suffered for PL-based weights

Figure 5.35: Representation of path Losses suffered along paths B and C in small graph

Focusing on the trend of perceived PLs along path B, we observe an initial increase followed by a subsequent decrease. As shown in figures 5.30a and 5.30b, the trajectory begins just below a BS and ends near another. This pattern explains the PL trend: approximately midway through the route, the drone is equidistant from both BSs, leading to higher PL values.
For path C, the drone starts in a relatively flat but isolated area, as seen in figures 5.31a and 5.31b, apart from the initial (but far) BS in LoS. Upon entering the built-up area, a series of handovers occur, resulting in the observed peaks in the initial steps. As the drone moves from the urban area towards the far northwest of the region, the PL exhibits a slight upward trend.

5.4.1 Performance Analysis of different drones - small graph scenario

In this scenario, the performance of the three different drone models—*DJI Avata 2, Inspire 2, and FlyCart 30*—can be directly compared. This comparison is feasible because the covered area is smaller, and the selected path for evaluation, *path D*, is more manageable for all three drone types. *Path B* exhibits performance trends similar to *path D*, as well as *path A* with *Path C*.
Table 5.10 presents the main communication KPIs for *path D*, which remain consistent across all three drone types. Concerning the second analyzed case, *Path C*, the main KPIs can be found in table 5.9.

KPIs	PL Optimized	STD Shortest Path
Traveled Distance (m)	1252.37	1177.81
Number of Ups	9	3
Number of Downs	6	0
Handover Count	2	3
Mean Path Loss (dB)	92.77	92.75
Maximum PL (dB)	94.29	94.31
Minimum PL (dB)	90.98	90.81
95th Percentile PL (dB)	94.11	94.12
99th Percentile PL (dB)	94.26	94.27
LoS Percentage (%)	100.0	100.0
NLoS Percentage (%)	0.0	0.0

Table 5.10: Communication KPIs for path D in small graph

As observed in previous analyses, the PL-optimized path exhibits more frequent altitude changes (ups and downs) compared to the standard shortest path for both the visualized cases C and D. This results in a longer traveled distance and higher power consumption. However, communication performance remains superior, as the handover count is lower in the PL-optimized path. Despite the mean PL being slightly higher than that of the standard shortest path, the overall reliability of the connection is improved, reducing the likelihood of communication disruptions. The PL-based path for all the drones, as expected, has more peaks in power consumptions due to the frequent ups and downs, compared to the PD-based path.

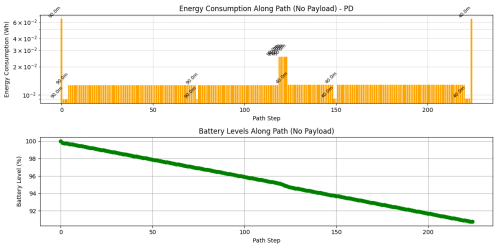

(a) Path C - Power Consumption & battery level with no payload (PD)

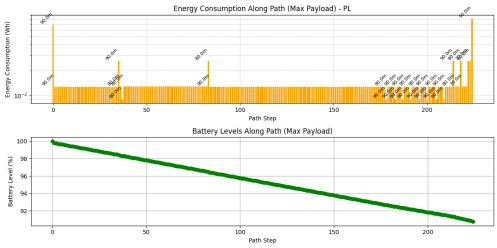

(b) Path C - Power Consumption & battery level with no payload (PL)

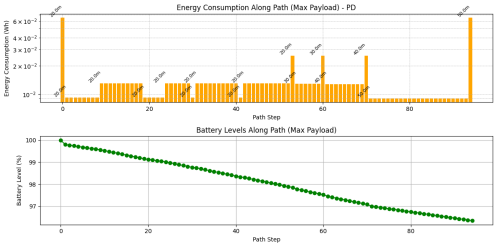

(c) Path D - Power Consumption & battery level with no payload (PD)

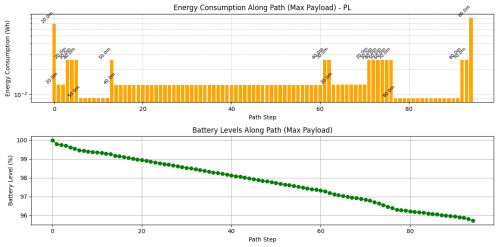

(d) Path D - Power Consumption & battery level with no payload (PL)

Figure 5.36: Power Consumption and battery level trends using Avata 2 along path C & D in small graph.

As mentioned in previous section, displayed in Figure 5.36, the energy consumption and battery level results for the *DJI Avata* drone account only for its own operational payload (being equal to 0.377), as it is not designed for transporting objects or materials. Instead, it is primarily intended for video recording over short distances. In the final results, *DJI Avata* ranged from a minimum of 0.01 to a maximum of 0.06 Wh in energy consumption, achieving:

- Path C
  - Final Battery Level:
    - PL-based: 90.51%
    - PD-based: 90.56%
  - Power Consumption:
    - PL-based: 9.49%
    - PD-based: 9.44%
- Path D
  - Final Battery Level:
    - PL-based: 95.69%
    - PD-based: 96.19%
  - Power Consumption:
    - PL-based: 4.31%
    - PD-based: 3.81%

As for *DJI Inspire 3*, figures 5.38 and 5.37 present the energy consumption results for both scenarios in *path C and D*: with no payload and with the maximum payload the drone can carry.
Since this drone operates at its maximum horizontal speed (see Table 5.1 for reference), which is higher than that of the other two models, this inevitably leads to increased power consumption.

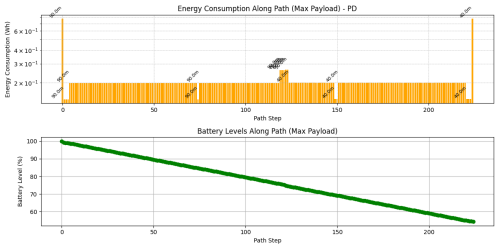

(a) Path C - Power Consumption & battery level with max payload (PD)

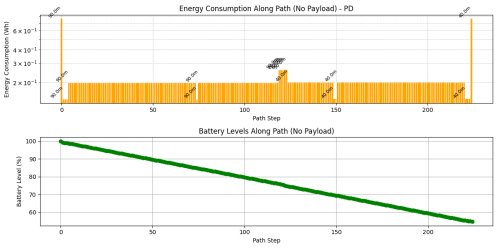

(b) Path C - Power Consumption & battery level with no payload (PD)

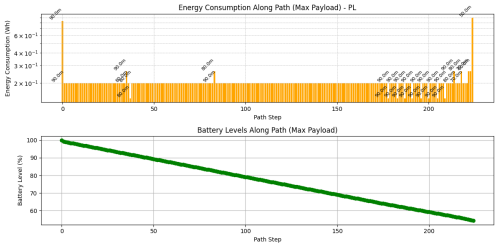

(c) Path C - Power Consumption & battery level with max payload (PL)

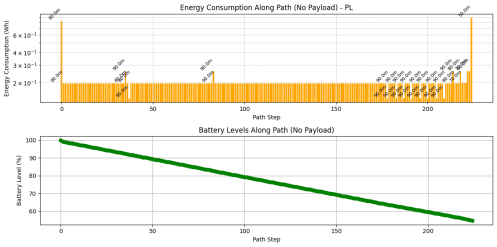

(d) Path C - Power Consumption & battery level with no payload (PL)

Figure 5.37: Power Consumption and battery level trends using Inspire 3 along path C in small graph

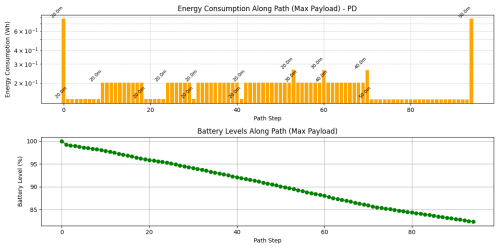

(a) Path D - Power Consumption & battery level with max payload (PD)

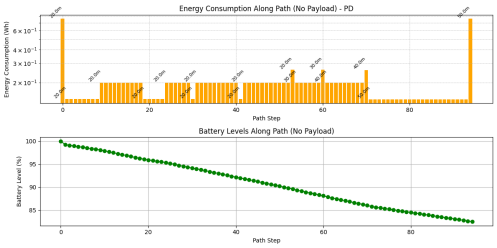

(b) Path D - Power Consumption & battery level with no payload (PD)

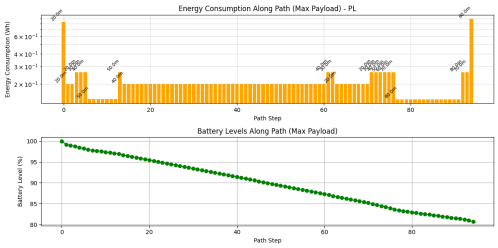

(c) Path D - Power Consumption & battery level with max payload (PL)

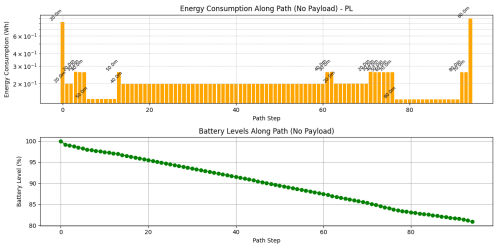

(d) Path D - Power Consumption & battery level with no payload (PL)

Figure 5.38: Power Consumption and battery level trends using Inspire 3 along path D in small graph

In the final results, the *DJI Inspire 3* exhibited energy consumption ranging from a minimum of 0.2 Wh to a maximum of 0.6 Wh for the PD-based path and from 0.2 Wh to 1 Wh for the PL-based path, achieving:

- Path C:
  - Final Battery Level:
    - Max Payload PL-based: 53.48%
    - No payload PL-based: 53.87%
    - Max Payload PD-based: 53.60%
    - No payload PD-based: 53.98%
  - Power Consumption:
    - Max Payload PL-based: 46.52%
    - No payload PL-based: 46.13%
    - Max Payload PD-based: 46.40%
    - No payload PD-based: 46.02%
- Path D:
  - Final Battery Level:
    - Max Payload PL-based: 65.64%
    - No payload PL-based: 68.27%
    - Max Payload PD-based: 69.05%
    - No payload PD-based: 71.35%
  - Power Consumption:
    - Max Payload PL-based: 34.36%
    - No payload PL-based: 31.73%
    - Max Payload PD-based: 30.95%
    - No payload PD-based: 28.65%

Finally, concerning instead the results obtained for both *Path C* and *Path D* for *DJI FlyCart 30*, these are displayed in figures 5.39 and 5.40.

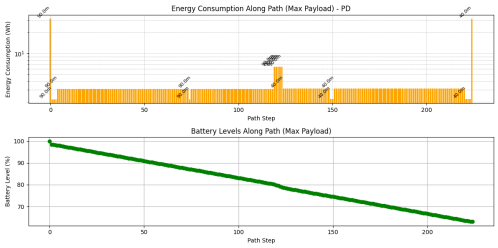

(a) Path C - Power Consumption & battery level with max payload (PD)

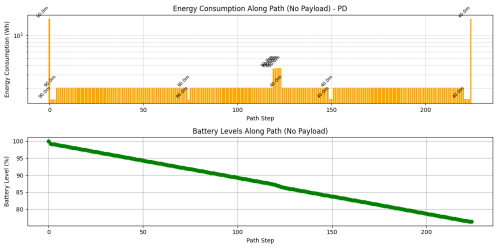

(b) Path C - Power Consumption & battery level with no payload (PD)

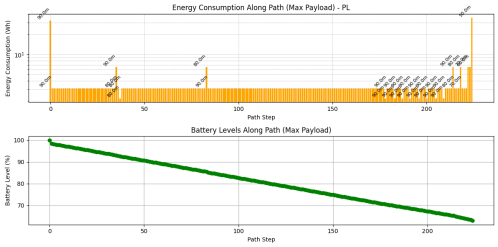

(c) Path C - Power Consumption & battery level with max payload (PL)

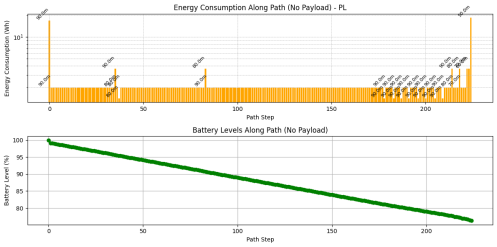

(d) Path C - Power Consumption & battery level with no payload (PL)

Figure 5.39: Power Consumption and battery level trends using FlyCart 30 along path C in small graph

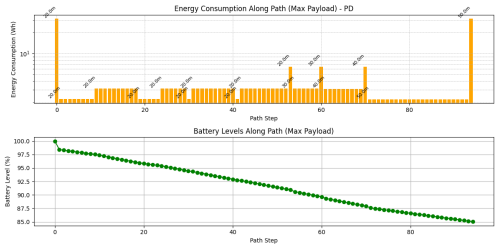

(a) Path D - Power Consumption & battery level with max payload (PD)

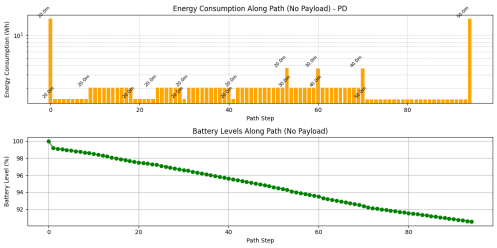

(b) Path D - Power Consumption & battery level with no payload (PD)

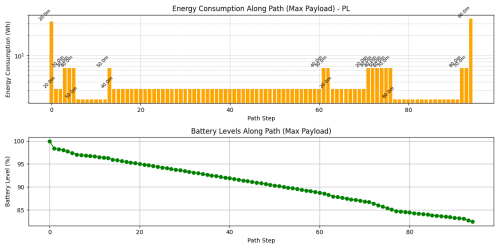

(c) Path D - Power Consumption & battery level with max payload (PL)

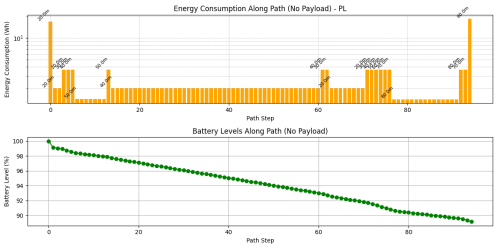

(d) Path D - Power Consumption & battery level with no payload (PL)

Figure 5.40: Power Consumption and battery level trends using FlyCart 30 along path D in small graph

Regarding the *DJI FlyCart 30*, as in previous cases, the initial and final peaks in power consumption are significantly higher than those observed for the other drones. This is due to the drone's need to generate sufficient lift for a greater mass

(see specifications 5.1), which becomes even more pronounced when carrying the maximum payload. In these scenarios, power consumption exceeds 10 Wh during these critical phases.
The final results obtained by *DJI FlyCart 30* in path C and D are:

- Path C:
  - Final Battery Level:
    - Max Payload PL-based: 61.16%
    - No payload PL-based: 75.36%
    - Max Payload PD-based: 61.51%
    - No payload PD-based: 75.53%
  - Power Consumption:
    - Max Payload PL-based: 38.84%
    - No payload PL-based: 24.64%
    - Max Payload PD-based: 38.49%
    - No payload PD-based: 24.47%
- Path D:
  - Final Battery Level:
    - Max Payload PL-based: 79.81%
    - No payload PL-based: 87.80%
    - Max Payload PD-based: 83.28%
    - No payload PD-based: 89.65%
  - Power Consumption:
    - Max Payload PL-based: 20.19%
    - No payload PL-based: 12.20%
    - Max Payload PD-based: 16.72%
    - No payload PD-based: 10.35%

5.4.2 Analysis of supported technologies - small graph scenario

The analysis of the main supported technologies confirms previous observations. The most commonly used technologies are those operating at lower frequencies within the 4G and 5G bands. The distribution of these technologies is illustrated in Figures 5.41 for shorter paths and 5.42 for longer ones.
One notable difference compared to the other scenarios is the increased frequency of handovers. This can be attributed to the lower flight altitude over the urban area, where BS in LoS frequently transition to NLoS due to obstacles. This phenomenon is particularly evident in paths weighted primarily by PD-based weights, as the drone is forced to switch connections more frequently.

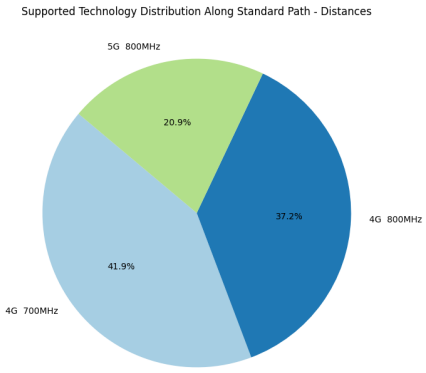

(a) Path B - supported tech exploited for PD-based weights

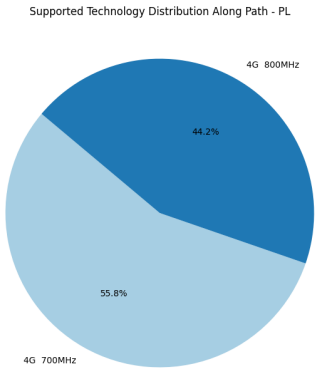

(b) Path B - supported tech exploited for PL-based weights

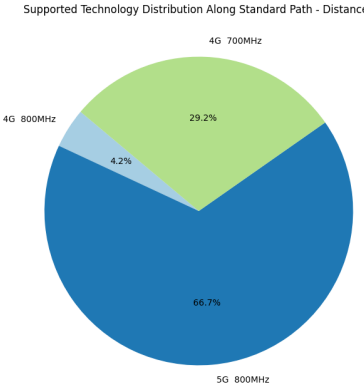

(c) Path D - supported tech exploited for PD-based weights

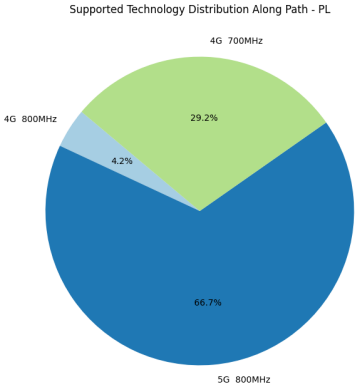

(d) Path D - supported tech exploited for PL-based weights

Figure 5.41: Pie charts - Supported Technologies for small graph

To further evaluate the impact of lower frequency bands, an additional test is conducted by removing all 4G 700/800 MHz bands. The results remain consistent with previous findings, confirming that 5G 800 MHz remains the dominant technology along the entire route, as shown in Figure 5.48.

The results, shown in 5.11, indicate that removing the 4G 700-800 MHz bands negatively impacts the average PL in both cases; however, the effect on handovers (#H) differs between the large and small graphs. In the larger graph, the removal of these bands led to an increase in both PL and #H, while in the smaller graph, only PL worsened, and #H remained the same or even decreased. This difference can be attributed to the greater discretization in the smaller graph, which allows for more route options, potentially reducing the need for frequent handovers. Additionally, in the larger graph, the 5G 800 MHz band was also removed, reducing the available

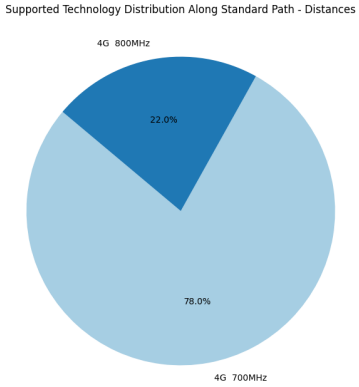

(a) Path A - Supported tech exploited for PD-based weights

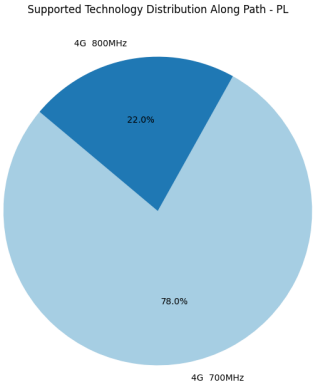

(b) Path A - supported tech exploited for PL-based weights

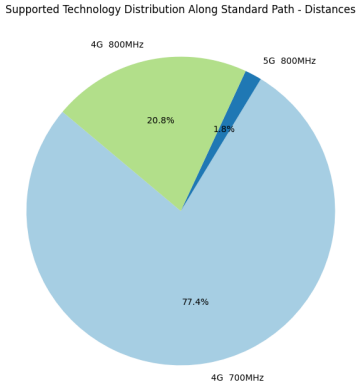

(c) Path C - supported tech exploited for PD-based weights

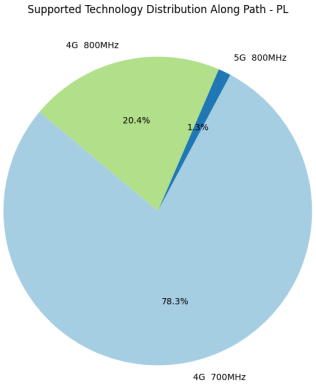

(d) Path C - supported tech exploited for PL-based weights

Figure 5.42: Pie charts - Supported Technologies for small graph

frequency bands significantly. In contrast, in the smaller graph, the 5G 800 MHz band remained, allowing it to compensate for the removed 4G bands, thus mitigating the impact on handovers.

Paths	**PL-based weights**		**PD-based weights**	
	STD	**NO 700-800 MHz**	**STD**	**NO 700-800 MHz**
Path A	93.54 #H=3	94.33 #H=3	93.39 #H=4	94.54 #H=6
Path B	91.63 #H=3	92.24 #H=1	91.71 #H=6	92.23 #H=3
Path C	93.54 #H=5	94.39 #H=3	93.46 #H=7	94.42 #H=6
Path D	92.77 #H=2	93.06 #H=2	92.75 #H=3	93.02 #H=2

Table 5.11: PL-based and PD-based weights for different paths.

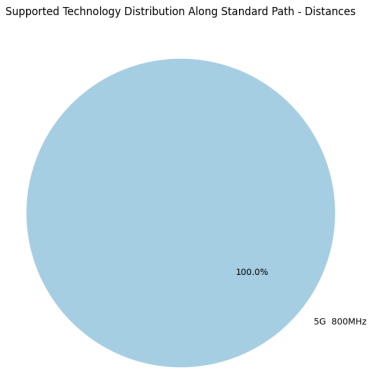

(a) Supported tech exploited for PD-based weights - no 4G 700/800 MHz

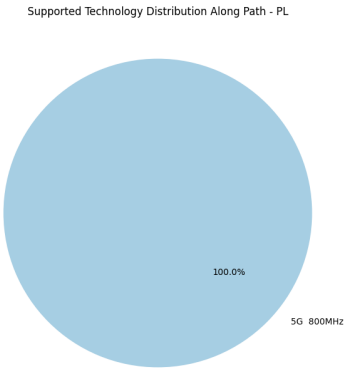

(b) Supported tech exploited for PL-based weights - no 4G 700/800 MHz

Figure 5.43: Pie charts - Supported Technologies for small graph with no 4G 700/800 MHz bands

5.5 Performance Analysis of the Trade off scenario

In this section, we analyze the performance of the proposed approach when optimizing the trade-off between communication quality and energy efficiency. The evaluation is conducted using the previous three graph representations, where the edge weights are derived from a combination of physical distance and path loss values. Unlike the previous cases, the objective here is to balance both spatial efficiency and communication reliability by assigning weighted contributions to each factor, as summarized in table 4.2.
To achieve this, a combined weight model is employed, as previously introduced, where the total weight of an edge is computed as a linear combination of path loss and physical distance. By adjusting the weighting coefficients, W_{PL} and W_{PD}, different trade-off scenarios are tested to assess their impact on routing decisions. The goal is to find an optimal balance that minimizes the physical path length without significantly degrading communication quality. For simplicity, we refer to this combination of the two weight types as the *Hybrid Weight* (HW).
It is important to note that, since physical distances generally have greater numerical values compared to path loss values (which are the normalized and scaled ratio of metrics expressed in dB), they tend to have a stronger influence on the final weights. As a result, the routing decisions will often be more similar to those obtained using a purely PD-based approach. This effect occurs because, even when PL is included in the weighting scheme, its relative contribution remains lower than that of PD unless explicitly amplified through the weighting coefficients.

The results presented below correspond to a single selected path from those analyzed previously, allowing for comparisons across the three different graph types. These results are evaluated under the three threshold configurations outlined in Table 4.2.

The same type of drone, *DJI Inspire 3*, is used in all the following results.

5.5.1 Analysis on default graph - trade off

For the default scenario using the 3-layered graph, *Path B* is selected. The original PL-based and PD-based 2D plots were previously presented in Figures 5.2a and 5.2b, respectively. The results obtained using the HW-based path are shown in Figure 5.44.
Since the differences between the various threshold configurations within each HW scenario are minimal, only the case of '50% PD vs. 50% PL' is displayed in the plots.

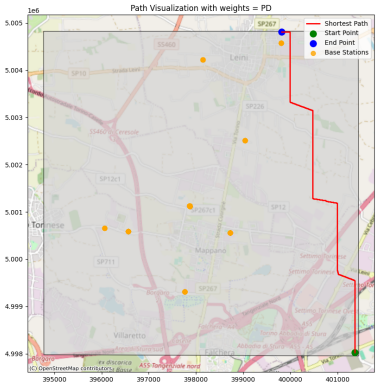

(a) 2D plot for the configuration 50% PD and 50%.

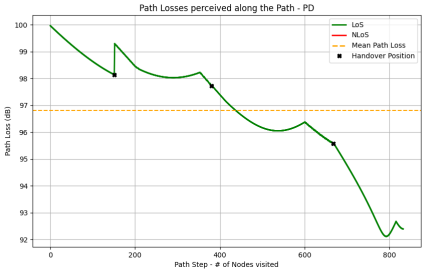

(b) Path losses perceived along path B in 50:50 trade off configuration

Figure 5.44: Results for path B in trade off scenario

Given that the *DJI Inspire 3* is chosen for this scenario, it is important to assess whether the computed trajectories fall within the operational limits of the drone's battery capacity. Based on manufacturer specifications, the Inspire 3 can cover in this case a maximum distance of approximately 6969.98 m with no payload and around 6483.35 m when carrying the maximum payload.

However, as observed in the computed results, the total power consumption in this scenario exceeds what the standard battery can support. This implies that the drone would be unable to complete the flight before the battery is fully depleted. As a result, the battery percentage will appear negative, and the total power consumption surpasses 100%, as illustrated in Figure 5.45.
However, despite this limitation, a meaningful comparison can still be made between the final power consumption in the standard cases and in the hybrid weight-based trade-off scenario.

The results presented in Table 5.12 indicate that the differences among the various HW-based outputs are small. This is likely due to the limited number of available paths, constrained by the number of cells and edges, which restricts the impact of

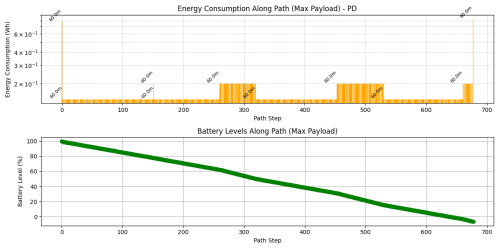

(a) Power consumptions for configuration 20:80 for max payload.

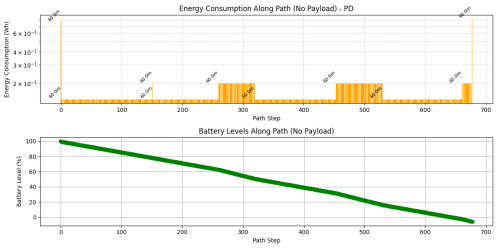

(b) Power consumptions for configuration 20:80 no payload

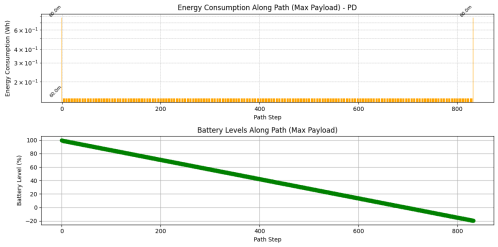

(c) Power consumptions for configuration 50:50 for max payload.

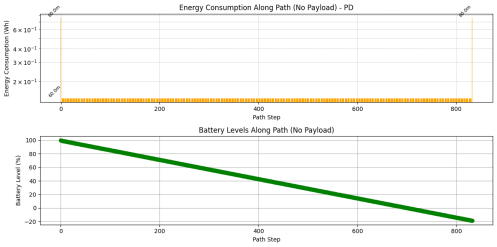

(d) Power consumptions for configuration 50:50 with no payload

Figure 5.45: Results for Power Consumptions and Battery Levels in path B in trade off default scenario

combining path loss and physical distance weights. However, a notable transition in communication performance occurs between the 80:20 HW and the 50:50 HW configurations, while the traveled distance and corresponding power consumption remain stable across all HW cases. This shift can be attributed to the selection of a specific edge over another (along x-y plane rather than z, which remains constant), enabling the drone to maintain connectivity with the same base station while minimizing the number of handovers.

On the other hand, the performance gap between the 20:80 and 50:50 HW cases is not as pronounced. Notably, the 50:50 HW configuration appears to offer the best trade-off for this path, achieving a slight reduction in total power consumption and traveled distance compared to the PL-based standard case, while maintaining the number of handovers at three. This suggests that a balanced weighting between path loss and physical distance can provide an effective routing solution, ensuring both energy efficiency and communication reliability.

Metrics	PL-based Std	PD-based Std	Trade off - PD:PL [%]		
			20:80	50:50	80:20
#H	3	4	3	3	4
Avg PL	96.80	96.51	97.02	97.024	96.51
Distance	7777.27	7422.03	7422.12	7422.03	7422.03
Tot PC Max Payload	120.64%	114.48%	114.48%	114.48%	114.48%
Tot PC No Payload	112.09%	106.48%	106.48%	106.48%	106.48%

Table 5.12: Comparisons on path B with all the trade off configurations - standard graph

5.5.2 Analysis on 4-layered graph - trade off

Since *path B* yields identical results for both the default and 4-layered graphs—having the same start and end points—*path A* is selected for this analysis. The main results are presented in Figure 5.46, while the power consumption trends for the 20:80 trade-off configuration are shown in Figure 5.47.

The 2D path and path loss plots for the three different configurations exhibit only minimal variations, making the differences nearly imperceptible. For this reason, only a single representative case is displayed.

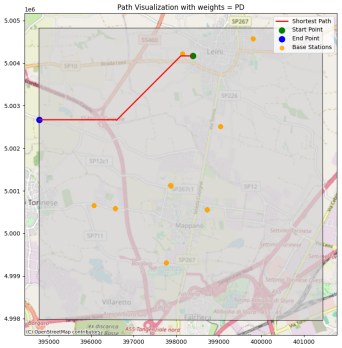

(a) 2D plot for the configuration 20% PD and 80%.

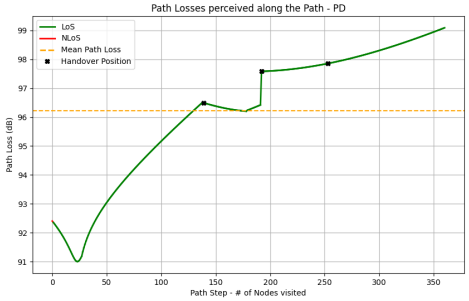

(b) Path losses perceived along path A in trade off scenario

Figure 5.46: Results for path A in trade off 4-layered scenario

The results in Table 5.13 indicate that the trade-off configurations produce only minor variations compared to the standard (STD) cases. While all hybrid configurations maintain a similar number of handovers, they show a slight reduction in average path loss compared to the PD-based case, though still higher than the PL-based scenario.

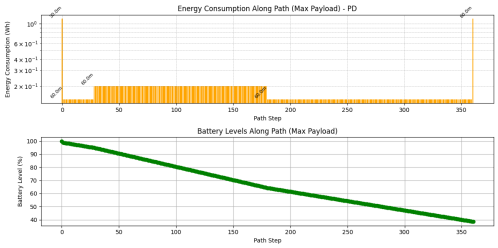

(a) Power consumption for the configuration 20% PD and 80% with max payload.

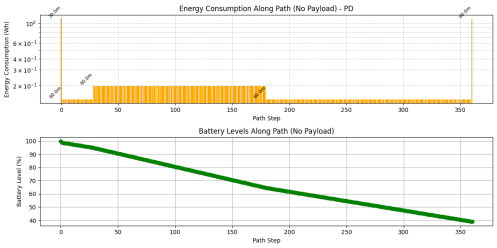

(b) Power consumption for the configuration 20% PD and 80% with no payload.

Figure 5.47: Results for path A in trade off 4-layered scenario

Regarding power consumption, the trade-off configurations exhibit a noticeable improvement over the PL-based case, aligning more closely with the PD-based results. Among them, the 50:50 and 80:20 configurations offer the most balanced outcome, achieving a reasonable compromise between signal quality and energy efficiency without significantly deviating from the shortest physical path.

Metrics	**PL-based STD**	**PD-based STD**	**Trade off - PD:PL [%]**		
			20:80	**50:50**	**80:20**
#H	2	2	3	3	3
Distance	4385.77	4274.56	4282.85	4274.57	4282.94
Avg PL	96.09	96.61	96.218	96.229	96.226
Tot PC Max Payload	68.87%	66.71%	62.60%	62.49%	62.49%
Tot PC No Payload	63.92%	61.98%	62.10%	61.98%	61.98%

Table 5.13: Comparisons on path A with all the trade off configurations - 4-layered graph

5.5.3 Analysis on small graph - trade off

The path selected for the small graph scenario is *path B*, whose results were previously discussed in the dedicated sections and summarized in Table 5.8 for the *DJI Inspire 3* drone.

The following figures present the 2D trajectory and the corresponding path loss variations experienced along *path B*. As observed in previous scenarios, the differences among the trade-off configurations are relatively minor. For this reason, Figures 5.48 illustrate only one representative trade-off case, specifically the 20:80 configuration.

Since the selected path is shorter than the previous ones, the *DJI Inspire 3* completes the flight without any issues. Figure 5.49 presents the results for the 20:80 trade-off configuration, as the other configurations yield results nearly identical to

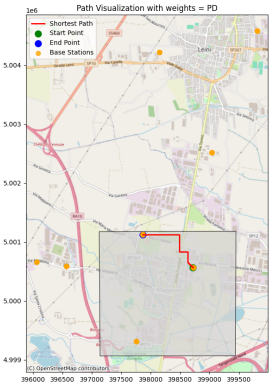

(a) 2D plot of path B using the 20:80 trade off configuration

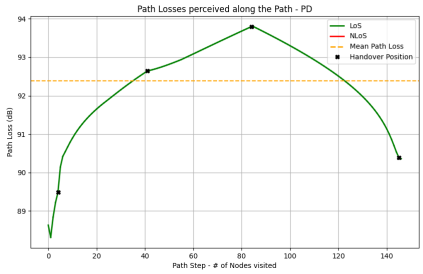

(b) Path Loss suffered along path B for configuration 20:80

Figure 5.48: Results for path B in trade off scenario - small graph

the PD-based case.

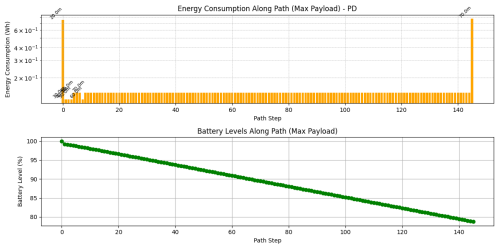

(a) Power consumptions for configuration 20:80 for max payload.

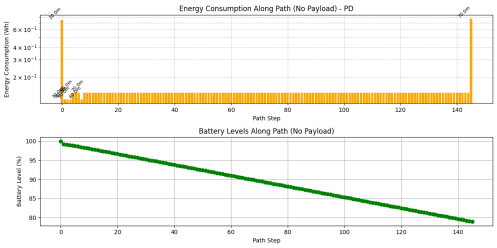

(b) Power consumptions for configuration 20:80 for no payload.

Figure 5.49: Results for path B in trade off scenario - small graph

Since the differences among the trade-off configurations are minimal and not easily distinguishable in the visual plots, Table 5.14 provides a summarized comparison of the obtained results.

The analysis conducted on the small graph reveals that all hybrid configurations (50:50, 80:20, and 20:80 HW) produce nearly identical outcomes in terms of average path loss, traveled distance, and power consumption, with no significant impact on communication performance. This similarity can be attributed to the relatively short traveled distance (1460 m), which limits the number of possible paths and variations in power consumption or path loss. Consequently, none of the hybrid configurations demonstrate a meaningful advantage over the others. In this particular case, when flying across an urban area, choosing an HW configuration is not the most effective solution, as the proximity to numerous antennas eliminates the need to optimize communication, while it comes at the cost of a significantly longer route.

Metrics	**PL-based Std**	**PD-based Std**	**Trade off - PD:PL [%]**		
			20:80	**50:50**	**80:20**
#H	3	6	4	4	4
Avg PL	91.63	91.71	92.39	92.39	92.39
Distance	1127.52	1102.67	1460.0	1460.0	1460.0
Tot PC Max Payload	30.69%	29.40%	22.02%	22.02%	22.02%
Tot PC No Payload	28.34%	27.19%	21.83%	21.83%	21.83%

Table 5.14: Comparisons on path B with all the trade off configurations - small graph

Chapter 6

Conclusions

This study explored an extended 3D graph-based model for BVLoS drone operations, incorporating additional altitude layers to enhance path diversity and improve communication performance. The results demonstrated how the introduction of additional z-axis layers influences drone trajectories, handover events, and power consumption, providing valuable insights for optimal communication quality and energy efficiency. By integrating path loss as a weighting parameter, we highlighted how signal reliability influences the choice of routes, especially in scenarios where NLoS conditions are prevalent. Additionally, the comparison between different drones revealed significant differences in energy consumption, further emphasizing the need for drone-specific optimizations in mission planning.

Another key finding of this study is that the hybrid weight configurations yield results that, while distinct from the standard PD- and PL-based cases, remain closely aligned with one another. The trade-off configurations consistently exhibit an intermediate behavior, balancing distance minimization and communication performance. In some cases, power consumption is even lower than in the standard PD-based scenario, while path loss values tend to be slightly worse. These results suggest that hybrid weight strategies can provide a viable middle ground between optimizing energy efficiency and maintaining acceptable signal quality.
Moreover, we observed that when traveling away from urban centers, the path loss experienced along the trajectory tends to be higher compared to paths that pass near urbanized areas (e.g., 5 up to 10 dB gap in a comparable traveled distance). As a result, the algorithm adapts by deviating from the shortest path to maintain connectivity, bringing the trajectory closer to the nearest base station. This behavior suggests that a hybrid approach would be most effective, dynamically adjusting the path selection based on the drone's proximity to urban areas and base stations. Such an approach would help mitigate signal loss while also limiting excessive deviations, thereby balancing communication reliability and power consumption. Conversely, in fully urban environments, where base station density is higher, the shortest path approach may be preferable, with the primary concern shifting to obstacle avoidance if buildings are too tall. Future refinements to this framework could incorporate adaptive weight adjustments based on environmental characteristics, further improving the robustness of drone trajectory planning in BVLoS operations.

6.1 Future Work

While the proposed model has demonstrated its effectiveness in improving BVLoS drone trajectory planning by incorporating additional altitude layers and communication-aware path selection, there are several directions for further development that could enhance its applicability and accuracy.
A natural extension of this work would involve adapting the channel model to urban environments by integrating the UMA propagation model. This would allow a more precise representation of signal propagation in densely built-up areas, where obstacles such as buildings significantly impact the received power and connectivity. By extending the model beyond the suburban scenario considered in this study, it would be possible to better assess the viability of BVLoS drone operations in real-world urban deployments.

Another important enhancement concerns the integration of dynamic constraints, such as the presence of no-fly zones. By incorporating regulatory and operational constraints into the path-planning process, the model could ensure that drones comply with airspace regulations while optimizing their trajectories for both communication performance and flight efficiency. This extension could involve real-time updates on restricted areas, allowing the drone to dynamically adapt its route when faced with new restrictions.
The communication model itself can also be further refined by considering additional environmental and network factors. Elements such as weather conditions, multipath effects, and base station congestion due to high ground traffic could be incorporated to achieve a more realistic assessment of connectivity along the planned routes. The impact of such factors on path loss and handover frequency would provide valuable insights into the robustness of communication links under various operational scenarios. Furthermore, an additional refinement could involve incorporating the uplink case, where the drone must transmit data back to the network. Since transmission power consumption depends on the drone's position relative to the base station it is associated with, considering uplink energy requirements would provide a more comprehensive optimization framework. This would allow for a more realistic approach, balancing both downlink and uplink efficiency, which is particularly crucial for missions involving, for example, real-time video streaming or sensor data collection.

Finally, improvements can be made in the power consumption modeling by incorporating additional parameters that affect drone energy efficiency. The inclusion of factors such as wind resistance, varying speed profiles, payload variations, and different atmospheric conditions would allow for a more comprehensive evaluation of energy consumption throughout the flight. Such refinements could lead to more accurate predictions of battery performance, ultimately contributing to more efficient mission planning.
By addressing these aspects, the model could be further extended to support more complex and dynamic operational scenarios, ensuring improved reliability and efficiency for BVLoS drone communications and navigation.

Bibliography

[1] https://www.statista.com/chart/5729/the-industries-where/-drones-could-really-take-off/

[2] https://www.forbes.com/sites/niallmccarthy/2016/09/02/the-industries-where-drones-could-really-take-off-infographic/#5477ff3027ad

[3] "Clarity from above PwC global report on the commercial applications of drone technology", report done by Drone Powered Solutions (DPS)

[4] https://www.precedenceresearch.com/commercial-drone-market

[5] Ilić, Damir, Ilic-Kosanovic, Tatjana, "New perspectives regarding the combat use of commercial drones in the context of the Russian-Ukrainian conflict", 2023/01/01 Serbian Journal of Engineering Management

[6] Chen, Siyuan, Laefer, Debra, Mangina, Eleni, "State of Technology Review of Civilian UAVs", 2016/07/12 Recent Patents on Engineering

[7] "Maximum coverage capacitated facility location problem with range constrained drones" by Darshan Chauhan, Avinash Unnikrishnan, Miguel Figliozzi

[8] https://www.thedroneu.com/blog/bvlos/

[9] https://www.safedroneflying.aero/en/drone-guide/drone-regulations

[10] E. Politi, I. Varlamis, K. Tserpes, M. Larsen and G. Dimitrakopoulos, "The future of safe BVLOS drone operations with respect to system and service engineering," 2022 IEEE International Conference on Service-Oriented System Engineering (SOSE), Newark, CA, USA, 2022, pp. 133-140, doi: 10.1109/SOSE55356.2022.00022. keywords: Visualization;Service-oriented systems engineering;Object detection;Sensor fusion;Turning;Search problems;Sensors;UAVs;market analysis;cloud-edge computing;BVLOS drones,

[11] F. B. Sorbelli, P. Chatterjee, P. Das and C. M. Pinotti, "Risk Assessment in BVLoS Operations for UAVs: Challenges and Solutions," 2024 20th International Conference on Distributed Computing in Smart Systems and the Internet of Things (DCOSS-IoT), Abu Dhabi, United Arab Emirates, 2024, pp. 300-307, doi: 10.1109/DCOSS-IoT61029.2024.00053. keywords: Surveys;Adaptation

models;Visualization;Heuristic algorithms;Scalability;Autonomous aerial vehicles;Path planning;UAV;UAS;UTM;BVLoS;risk assessment,

[12] `https://droneii.com/bvlos-operations-expanding-the-frontier`

[13] F. Betti Sorbelli, P. Chatterjee, F. Corò, S. Ghobadi, L. Palazzetti and C. M. Pinotti, "A Novel Graph-Based Multi-Layer Framework for Managing Drone BVLoS Operations," in IEEE Transactions on Network and Service Management, vol. 21, no. 5, pp. 5091-5105, Oct. 2024, doi: 10.1109/TNSM.2024.3401175. keywords: Drones;Path planning;Planning;Risk management;Autonomous aerial vehicles;Visualization;Vegetation;Drones;BVLoS;connectivity;ground risk,

[14] `https://www.droneleye.eu/piloti-di-droni/la-radio/#:~:text=L'uso%20delle%20radiofrequenze%20%C3%A8,25mW%20per%20i%205.8GHz.`

[15] M. Meo, D. Renga and F. Scarpa, "Integrating Aerial Base Stations for sustainable urban mobile networks," GLOBECOM 2022 - 2022 IEEE Global Communications Conference, Rio de Janeiro, Brazil, 2022, pp. 1727-1733, doi: 10.1109/GLOBECOM48099.2022.10001387. keywords: 6G mobile communication;Base stations;Costs;5G mobile communication;Urban areas;Quality of service;Resource management;Non-Terrestrial Networks;HAPS;5G/6G Networks;Energy Efficiency;Renewable Energy,

[16] L. Gupta, R. Jain and G. Vaszkun, "Survey of Important Issues in UAV Communication Networks," in IEEE Communications Surveys & Tutorials, vol. 18, no. 2, pp. 1123-1152, Secondquarter 2016, doi: 10.1109/COMST.2015.2495297. keywords: Mobile computing;Topology;Network topology;Mesh networks;Routing protocols;Routing;Unmanned Aerial Vehicle;UAV;Multi-UAV Networks;ad hoc networks;communication networks;wireless mesh networks;software defined network;routing;seamless handover;energy efficiency;,

[17] Y. Zeng and R. Zhang, "Energy-Efficient UAV Communication With Trajectory Optimization," in IEEE Transactions on Wireless Communications, vol. 16, no. 6, pp. 3747-3760, June 2017, doi: 10.1109/TWC.2017.2688328. keywords: Energy consumption;Wireless communication;Unmanned aerial vehicles;Propulsion;Trajectory optimization;Acceleration;UAV communication;energy efficiency;trajectory optimization;sequential convex optimization,

[18] B. Li, Z. Fei, Y. Zhang and M. Guizani, "Secure UAV Communication Networks over 5G," in IEEE Wireless Communications, vol. 26, no. 5, pp. 114-120, October 2019, doi: 10.1109/MWC.2019.1800458. keywords: Network security;Communication system security;Interference;Unmanned aerial vehicles;Jamming;Ad hoc networks,

[19] Tengkuo Zhu, Stephen D. Boyles, Avinash Unnikrishnan, "Two-stage robust facility location problem with drones, Transportation Research Part C: Emerging Technologies", Volume 137, 2022, 103563, ISSN 0968-090X, https://doi.org/10.1016/j.trc.2022.103563.

[20] H. V. Abeywickrama, B. A. Jayawickrama, Y. He and E. Dutkiewicz, "Empirical Power Consumption Model for UAVs," 2018 IEEE 88th Vehicular Technology Conference (VTC-Fall), Chicago, IL, USA, 2018, pp. 1-5, doi: 10.1109/VTCFall.2018.8690666. keywords: Power demand;Unmanned aerial vehicles;Batteries;Wireless fidelity;Energy consumption;Meters;Global Positioning System;UAV;power consumption;energy consumption;power consumption model,

[21] V. V. Díaz and D. Marcano Aviles, "A Path Loss Simulator for the 3GPP 5G Channel Models," 2018 IEEE XXV International Conference on Electronics, Electrical Engineering and Computing (INTERCON), Lima, Peru, 2018, pp. 1-4, doi: 10.1109/INTERCON.2018.8526374. keywords: 3GPP;Channel models;5G mobile communication;Macrocell networks;Fading channels;Device-to-device communication;5G;path loss;simulator;3GPP,

[22] W. Khawaja, I. Guvenc, D. W. Matolak, U. -C. Fiebig and N. Schneckenburger, "A Survey of Air-to-Ground Propagation Channel Modeling for Unmanned Aerial Vehicles," in IEEE Communications Surveys & Tutorials, vol. 21, no. 3, pp. 2361-2391, thirdquarter 2019, doi: 10.1109/COMST.2019.2915069. keywords: Atmospheric modeling;Channel models;Loss measurement;Unmanned aerial vehicles;Fading channels;Frequency measurement;L-band;Air-to-ground (AG);channel measurement;channel modeling;drone;large and small scale fading;sounding;unmanned aerial vehicle (UAV),

[23] TR 138 901 - V16.1.0 - 5G; Study on channel model for frequencies from 0.5 to 100 GHz (3GPP TR 38.901 version 16.1.0 Release 16)

[24] K. Wang et al., "Path Loss Measurement and Modeling for Low-Altitude UAV Access Channels," 2017 IEEE 86th Vehicular Technology Conference (VTC-Fall), Toronto, ON, Canada, 2017, pp. 1-5, doi: 10.1109/VTCFall.2017.8288385. keywords: Meters;Antenna measurements;3GPP;Channel models;Loss measurement;Current measurement;Frequency measurement,

[25] S. K. Jha, R. Rokaya, A. Bhagat, A. R. Khan and L. Aryal, "LTE Network: Coverage and Capacity Planning — 4G Cellular Network Planning around Banepa," 2017 International Conference on Networking and Network Applications (NaNA), Kathmandu, Nepal, 2017, pp. 180-185, doi: 10.1109/NaNA.2017.23. keywords: Planning;Long Term Evolution;Propagation losses;Capacity planning;Downlink;Receivers;Uplink;Long Term Evolution(LTE);Network capacity;Network Planning;Atoll,

[26] F. B. Sorbelli, P. Chatterjee, F. Coro, L. Palazzetti and C. M. Pinotti, "A Novel Multi-Layer Framework for BVLoS Drone Operation: A Preliminary Study," IEEE INFOCOM 2023 - IEEE Conference on Computer Communications Workshops (INFOCOM WKSHPS), Hoboken, NJ, USA, 2023, pp. 1-6, doi: 10.1109/INFOCOMWKSHPS57453.2023.10225806. keywords: Cellular networks;Visualization;Conferences;Emergency services;Product delivery;Agriculture;Planning;Drones;BVLoS;Connectivity;Ground risk,

[27] Yangsheng Xia, Chao Chen, Yao Liu, Jianmai Shi, Zhong Liu, "Two-layer path planning for multi-area coverage by a cooperative ground vehicle and drone system", The Laboratory of Big Data and Decision, College of Systems Engineering, National University of Defense Technology, Changsha 410073, China

[28] Shubhani Aggarwal, Neeraj Kumar, "Path planning techniques for unmanned aerial vehicles: A review, solutions, and challenges", Computer Science and Engineering Department, Thapar Institute of Engineering and Technology, Patiala, Punjab, India

[29] GERMAN CASTELLANOS, ACHIEL COLPAERT, MARGOT DERUYCK (Member, IEEE), EMMERIC TANGHE ,EVGENII VINOGRADOV, LUC MARTENS (Member, IEEE), SOFIE POLLIN, AND WOUT JOSEPH, (Senior Member, IEEE); "Evaluation of Beamsteering Performance in MultiuserMIMO Unmanned Aerial Base Stations Networks"

[30] `https://lteitaly.it/it/internal/map.php#6`

[31] `https://www.regione.piemonte.it/web/sites/default/files/media/documenti/2018-11/ai06_maira_0.pdf`

[32] "Fundamentals of Wireless Communication" by David Tse and Pramod Viswanath, published by Cambridge University Press.

[33] `https://support.zyxel.eu/hc/en-us/articles/360005188999-Signal-quality-LTE-5G-LTE-and-5G-signal-quality-parameters`

[34] `https://halberdbastion.com/technology/cellular/4g-lte/lte-frequency-bands/b7-2600-mhz`

[35] `"https://www.researchgate.net/figure/A-algorithm-flow-chart_fig2_361199586"`

[36] `https://wiki.teltonika-networks.com/view/Mobile_Signal_Strength_Recommendations`

[37] Thibbotuwawa, A., Nielsen, P., Zbigniew, B., Bocewicz, G. (2019). Energy Consumption in Unmanned Aerial Vehicles: A Review of Energy Consumption Models and Their Relation to the UAV Routing. In: Świątek, J., Borzemski, L., Wilimowska, Z. (eds) Information Systems Architecture and Technology: Proceedings of 39th International Conference on Information Systems Architecture and Technology – ISAT 2018. ISAT 2018.

[38] `https://www.dji.com/it/camera-drones?site=brandsite&from=nav`

[39] F. B. Sorbelli, F. Corò, S. K. Das and C. M. Pinotti, "Energy-Constrained Delivery of Goods With Drones Under Varying Wind Conditions," in IEEE Transactions on Intelligent Transportation Systems, vol. 22, no. 9, pp. 6048-6060, Sept. 2021, doi: 10.1109/TITS.2020.3044420. keywords: Drones;Heuristic algo-

rithms;Payloads;Energy consumption;Vehicle dynamics;Batteries;Shortest path problem;Drone delivery algorithms;energy model;wind model;time-dependent cost graphs;mission feasibility problem,

[40] Thibbotuwawa, A., Nielsen, P., Zbigniew, B., Bocewicz, G. (2019). Energy Consumption in Unmanned Aerial Vehicles: A Review of Energy Consumption Models and Their Relation to the UAV Routing. In: Świątek, J., Borzemski, L., Wilimowska, Z. (eds) Information Systems Architecture and Technology: Proceedings of 39th International Conference on Information Systems Architecture and Technology – ISAT 2018. ISAT 2018. Advances in Intelligent Systems and Computing, vol 853. Springer, Cham.

[41] `https://www.dji.com/it/avata-2/specs`

[42] `https://www.dji.com/it/flycart-30/specs`

[43] `https://www.dji.com/it/inspire-3/specs`

[44] `https://networkx.org/documentation/stable/index.html`

[45] `https://en.wikipedia.org/wiki/Dijkstra%27s_algorithm`

[46] `https://networkx.org/documentation/stable/reference/algorithms/shortest_paths.html`